Since 1955

Strojniški vestnik
Journal of Mechanical Engineering

no. 1-2
year 2021
volume 67

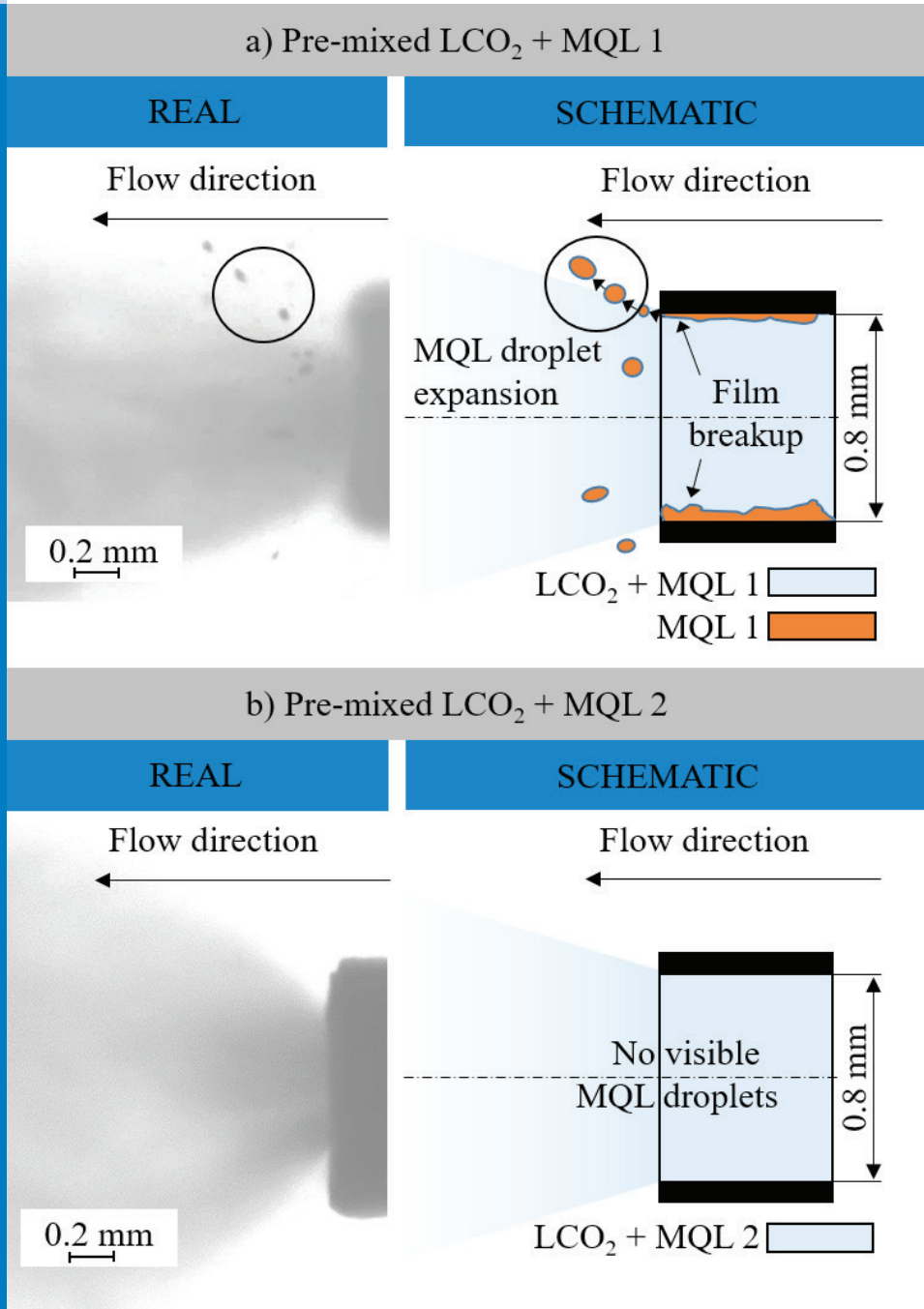

Strojniški vestnik – Journal of Mechanical Engineering (SV-JME)

Aim and Scope
The international journal publishes original and (mini)review articles covering the concepts of materials science, mechanics, kinematics, thermodynamics, energy and environment, mechatronics and robotics, fluid mechanics, tribology, cybernetics, industrial engineering and structural analysis.
The journal follows new trends and progress proven practice in the mechanical engineering and also in the closely related sciences as are electrical, civil and process engineering, medicine, microbiology, ecology, agriculture, transport systems, aviation, and others, thus creating a unique forum for interdisciplinary or multidisciplinary dialogue.
The international conferences selected papers are welcome for publishing as a special issue of SV-JME with invited co-editor(s).

Print: Demat d.o.o., printed in 250 copies

Founders and Publishers
University of Ljubljana, Faculty of Mechanical Engineering, Slovenia
University of Maribor, Faculty of Mechanical Engineering, Slovenia
Association of Mechanical Engineers of Slovenia
Chamber of Commerce and Industry of Slovenia, Metal Processing Industry Association

Cover:
Single-channel supply of pre-mixed media of LCO_2 + MQL represents a state-of-the-art LCO_2 assisted machining. However, to fully understand and optimize cooling and lubrication, a fundamental media flow analysis was essential. Therefore, media flow velocity and oil droplet size were analysed in supplying line and at the nozzle outlet utilizing different media flow rates and MQL oil polarities.

Image courtesy:
Laboratory for Machining, University of Ljubljana, Faculty of Mechanical Engineering, Ljubljana, Slovenia

ISSN 0039-2480, ISSN 2536-2948 (online)

General information
Strojniški vestnik – Journal of Mechanical Engineering is published in 11 issues per year (July and August is a double issue).

Institutional prices include print & online access: institutional subscription price and foreign subscription €100,00 (the price of a single issue is €10,00); general public subscription and student subscription €50,00 (the price of a single issue is €5,00). Prices are exclusive of tax. Delivery is included in the price. The recipient is responsible for paying any import duties or taxes. Legal title passes to the customer on dispatch by our distributor. Single issues from current and recent volumes are available at the current single-issue price. To order the journal, please complete the form on our website. For submissions, subscriptions and all other information please visit: *http://www.sv-jme.eu.*

You can advertise on the inner and outer side of the back cover of the journal. The authors of the published papers are invited to send photos or pictures with short explanation for cover content.

We would like to thank the reviewers who have taken part in the peer-review process.

The journal is subsidized by Slovenian Research Agency.

Strojniški vestnik - Journal of Mechanical Engineering is available on *https://www.sv-jme.eu.*

Contents

Strojniški vestnik - Journal of Mechanical Engineering
volume 67, (2021), number 1-2
Ljubljana, January-February 2021
ISSN 0039-2480

Published monthly

Papers

Strojniški vestnik - Journal of Mechanical Engineering 67(2021)1-2, 3-10

DOI:10.5545/sv-jme.2020.7076 Original Scientific Paper
Received for review: 2020-12-22
Received revised form: 2021-02-14
Accepted for publication: 2021-02-16

Media Flow Analysis of Single-Channel Pre-Mixed Liquid CO_2 and MQL in Sustainable Machining

Damir Grguraš[1] – Luka Sterle[1] – Aleš Malneršič[1] – Luka Kastelic[1] – Cedric Courbon[2] – Franci Pušavec[1,*]

[1] University of Ljubljana, Faculty of Mechanical Engineering, Slovenia
[2] University of Lyon, École nationale d'ingénieurs de Saint-Étienne (ÉNISE), France

Single-channel supply of pre-mixed liquid carbon dioxide (LCO_2) and minimum quantity lubrication (MQL) represents a state-of-the-art LCO_2 assisted machining. However, to fully understand and optimize cooling and lubrication provided by the LCO_2 + MQL, a fundamental media flow analysis is essential, yet not researched enough. Therefore, in this paper, media flow velocity and oil droplet size were analysed in supplying line and at the nozzle outlet using high-speed camera and proprietary single-channel system. Results indicate that pre-mixed media flow velocity is mainly influenced by the LCO_2 expansion rate upon the nozzle outlet, wherein oil droplet size is largely dependent on the solubility between oil and LCO_2. Media flow velocity increases significantly from an average of 40 m/s in the supplying line to the excess of 90 m/s at the nozzle outlet due to the pressure drop and LCO_2 expansion. Furthermore, this volume expansion causes the oil droplet to increase to the point of critical, unstable droplet size. Afterward, the unstable oil droplet breaks up into smaller oil droplets. It was found, that nonpolar oil, with greater solubility in LCO_2, compared to the polar oil, provides droplets as small as 2 µm in diameter. Smaller oil droplets positively reflect on tool wear and tool life in LCO_2 assisted machining, as the longest tool life was achieved by using the nonpolar oil for pre-mixed LCO_2 + MQL.
Keywords: flow analysis, flow velocity, droplet size, single-channel supply, liquid carbon dioxide – LCO_2, minimum quantity lubrication – MQL, LCO_2 assisted machining

Highlights
- *LCO_2 assisted machining with single-channel supply of pre-mixed liquid CO_2 and MQL was introduced as the sustainable replacement to conventional machining with flood lubrication.*
- *Analysis of pre-mixed LCO_2 and MQL media flow was carried out.*
- *Media flow analysis was performed using high-speed camera, determining media flow velocity and media droplet size.*
- *Results of the media flow analysis were coupled with tool life experiments in LCO_2 assisted machining of Ti-6Al-4V (β).*

0 INTRODUCTION

During machining, especially of difficult-to-cut materials, excessive heat generation in the cutting zone demands adequate cooling and lubrication. Normally, conventional machining with flood lubrication and low cutting speed is applied, reflecting in lower machining productivity. In addition, conventional oil-based emulsions are found non-sustainable due to adverse impact on environment and worker's health. Studies are showing that minimum quantity lubrication (MQL) can be an alternative to flood lubrication [1]. To further emphasize the potential of MQL lubrication, innovative MQL approaches have been proposed, namely electrostatic MQL (EMQL), hybrid nano-particles immersed EMQL and electrostatic lubrication [2]. Nevertheless, the absence of MQL cooling ability demands other sustainable alternatives to allocate both – cooling and lubrication. Studies showed that combination of liquid nitrogen and MQL (N_2 + MQL) in cryogenic machining yields lower tool wear and surface roughness [3]. The use of liquid carbon dioxide (LCO_2) in combination with MQL is another approach to improve machining performance [4]. In such LCO_2 assisted machining, pre-mixed LCO_2 + MQL represents state-of-the-art, whereas LCO_2 provides cooling and MQL lubrication effects [5].

Extensive research on cooling was carried out by Pušavec et al. [6], providing a better understanding of cooling capability of LCO_2 in comparison with flood lubrication. It has been shown that even though the tool temperatures are lower when using flood lubrication, LCO_2 in combination with MQL yields longer tool life. On the other hand, however, lubrication capability of pre-mixed LCO_2 + MQL lacks in scientific research. Only a few studies can be found discussing MQL oil droplets; all of them are related to the conventional MQL or MQCL (minimum quantity cooling lubrication), where pressurized air is used as a carrier media. MQL study by Cabanettes et al. [7] discovered that oil droplets adhere to the wall of the supplying line by creating a film along the wall. At the nozzle outlet, this is followed by the film disintegration and the formation of oil droplets. In addition, the oil viscosity, as discovered by Muaz and Choudhury [8], conditions the lubrication ability of MQL. Lower viscosity oils are preferable for

*Corr. Author's Address: University of Ljubljana, Faculty of Mechanical Engineering, Aškerčeva 6, 1000 Ljubljana, Slovenia, franci.pusavec@fs.uni-lj.si

MQL, since smaller oil droplets and thus deeper penetration into the cutting zone can be achieved. Similar was reported for MQCL [9]. In addition, increase in the airflow provides higher quantity of oil droplets [10] and [11], wherein increase in the nozzle-workpiece distance provides decrease in oil droplet size. According to Maruda et al. [11], MQCL droplets of the diameter less than 5 μm can quickly evaporate from the heated surface and have the least negative effect on human health.

Presented studies show that deeper understanding of media flow leads to a better understanding of MQL / MQCL machining. Accordingly, one must be aware that state-of-the-art LCO_2 + MQL flow is not entirely understandable. In this paper, therefore, an attempt is made to advance the understanding of the pre-mixed LCO_2 + MQL media flow characteristics. The knowledge of pre-mixed LCO_2 + MQL flow characteristics can be used for deeper understanding about the cooling and lubrication abilities of this novel technology. With regard to that, media flow velocity and oil droplet size were analysed using a high-speed camera at three key locations: (i) in the supplying line; (ii) directly after the nozzle outlet; (iii) near the nozzle outlet. In addition, results obtained from this fundamental study were coupled with authors' previous tool life experiments in LCO_2 assisted milling of Ti-6Al-4V (β) [5]. Moreover, suggestions for future work and practical workshop conclusions have been drawn.

1 EXPERIMENTAL PROCEDURE

For the media flow analysis, a unique experimental setup was developed as shown in Fig. 1. The LCO_2 + MQL media flow was analysed using a high-speed camera at three positions:

- Position A: for analysing the flow in the supplying line, where the average media flow velocity was determined,
- Position B: for analysing the flow at the nozzle outlet, in the immediate vicinity of the nozzle (close to the nozzle), where the average flow velocity and average oil droplet diameter were determined,
- Position C: for analysing the expanding media flow at the nozzle outlet, at a distance from the nozzle (far from the nozzle, i.e. 3 mm from the nozzle), where the average flow velocity and average oil droplet diameter were determined.

At position A, the high-speed camera was mounted perpendicular to the supplying line, with a distance of

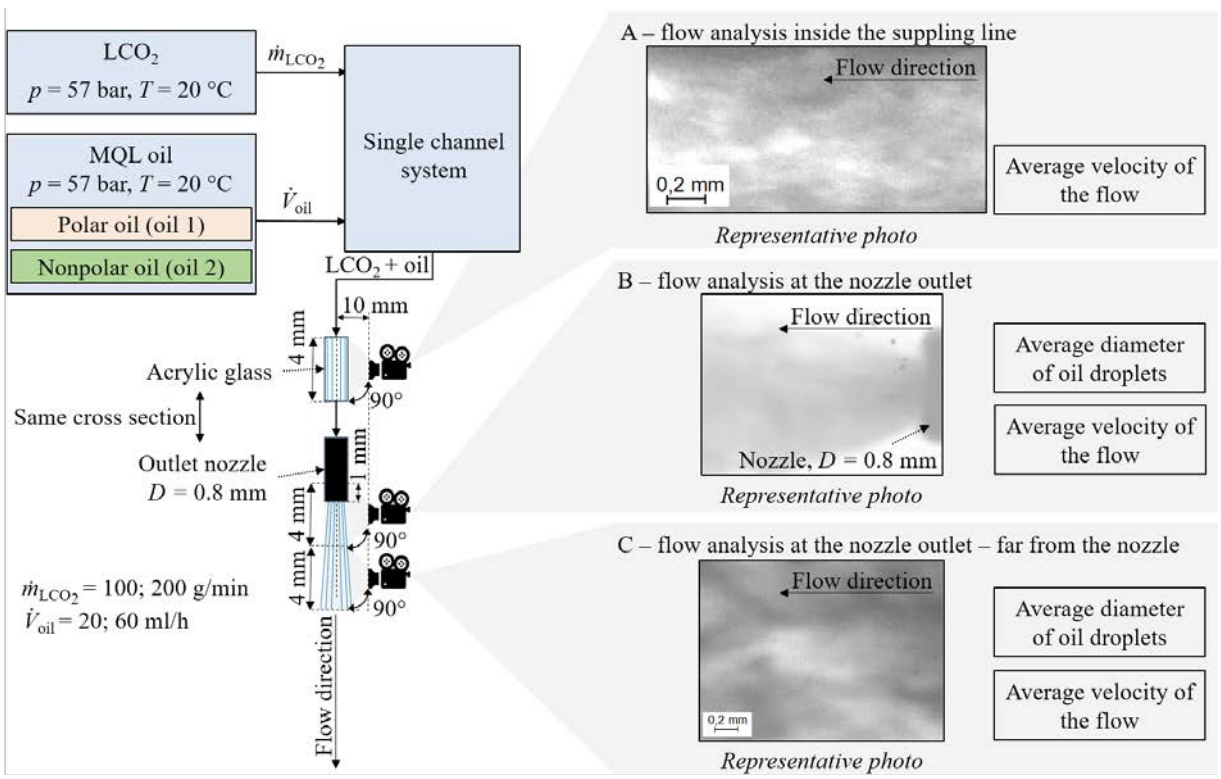

Fig. 1. *Illustration of the experimental setup*

10 mm from it. Media flow analysis at the position A was carried out using specially designed acrylic chamber with a square cross section, as shown in Fig. 2. The square cross section provided the possibility of recording of the media flow without any reflection issues. The chamber consists of two acrylic parts, which are secured together using eight screws. Two positioning holes provide the positioning accuracy of both sides. It should be noted that the cross section of the nozzle and the cross section of the supplying line chamber were identical. The identical cross-sections provide a smooth flow of the LCO_2 + MQL media, without any pressure drop due to the cross-sectional change inside the pipeline / supplying line. At position B, the high-speed camera was mounted perpendicular to the nozzle outlet, with a distance of 10 mm from the nozzle in such a manner that recording the flow of LCO_2 + MQL directly at the nozzle outlet has been performed. The high-speed camera was positioned to cover a measurement window of 4 mm × 4 mm. At position C, the high-speed camera was mounted perpendicular to the nozzle outlet, with a distance of 10 mm from the nozzle. At this position, the LCO_2 + MQL expanding flow was analysed 3 mm away from the nozzle outlet, as shown in Fig. 1.

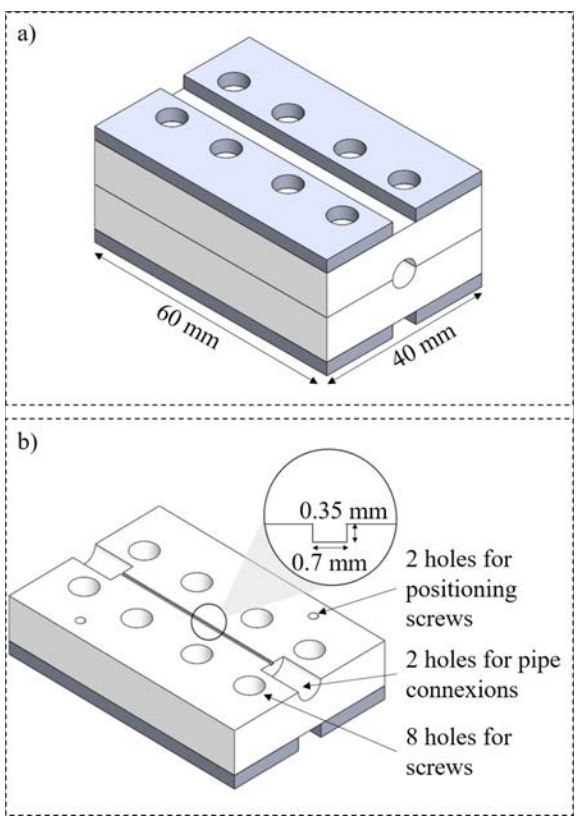

Fig. 2. *Acrylic glass chamber, a) 3D view, and b) sectional view*

Experiments have been performed separately with high-speed camera that has been moved to the desired camera positions A, B or C, with the following settings: (i) frame resolution of 512 × 384 pixels and (ii) frame rate of 67500 frames per seconds [fps]. Afterwards, Photron Fastcam Analysis software was used to extract the data from recorded videos and to analyse the media velocity and oil droplet size. Media velocity was determined by following the characteristic part of the media stream, i.e. dark areas or oil droplets in the stream. Using the analysis software, media velocity was then calculated from the change of flow path in a time period. For the sake of repeatability, every experiment was repeated five times.

A proprietary single-channel supply system ArcLub One, detailed in **[12]**, was used to supply the pre-mixed LCO_2 + MQL media under the temperature of T = 20 °C and the pressure of p = 57 bar. In this study, LCO_2 mass flow rates of $\dot{m}_{LCO2}$ = 100 g/min and 200 g/min and oil (MQL) volume flow rates of $\dot{V}_{oil}$ = 20 ml/h and 60 ml/h were used. The flow rates were selected based on the state-of-the-art studies: (i) LCO_2 flow rates from **[5]** and **[13]** and (ii) oil flow rates from **[10]** and **[14]**.

As concluded in **[5]** and **[12]**, oil polarity affects its solubility in LCO_2, which further influences the tool life. Therefore, in this study, MQL oils with different polarities were used: (i) polar MQL oil (oil 1) and (ii) nonpolar MQL oil (oil 2). Other physical and chemical properties of oils are given in Table 1.

Table 1. *Physical and chemical properties of oils (according to the oil manufacturer's specifications)*

	Oil 1	Oil 2
Physical state at 20 °C	Liquid	Liquid
Colour	Amber	Clear yellow
Odour	Weak, characteristic	Characteristic
Chemical characterization	Mixture of esters and additives	Base oil with additives
Density at 20 °C [g/cm³]	0.90 (DIN 51757)	0.87 (DIN 51757)
Kinematic viscosity at 20 °C [mm²/s]	N/A (22 at 40 °C) (ISO 3104)	3.5 (DIN 51562)
Polarity	Polar	Nonpolar

2 RESULTS AND DISCUSSION

2.1 High-Speed Camera Position A – Media Flow Analysis Inside the Supplying Line

Fig. 3 shows the media stream of LCO_2 + MQL inside the supplying line. As found in [5] and [12], polar oils have limited ability of mixing with LCO_2. Using the high-speed camera, this can be seen as a two-phase flow inside the supplying line. With other words, mixture of LCO_2 + MQL (oil 1), as well as unmixed portion of the oil 1 can be seen (Fig. 3a; dark spots). On the other hand, as oil 2 is nonpolar and dissolves to a greater extent in LCO_2, it is not possible to find any residual oil, which is not mixed with LCO_2. Only the flow of the mixture of LCO_2 + MQL (oil 2) can be noticed, as shown in Fig. 3b.

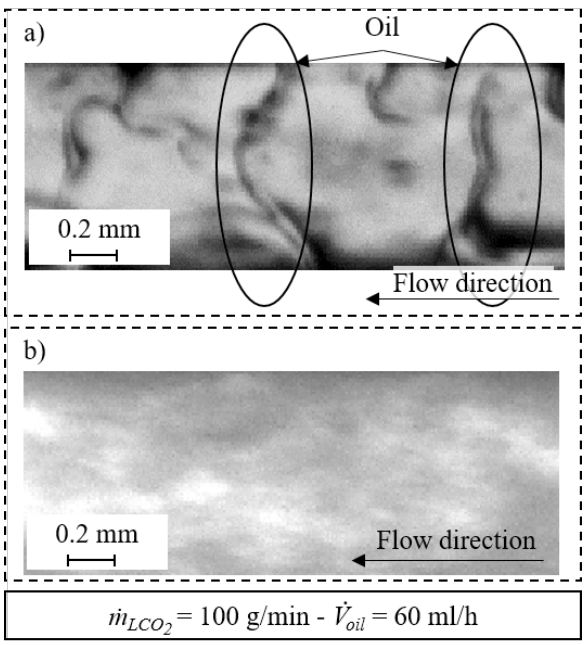

Fig. 3. *Media flow analysis inside the supplying line; a) LCO_2 + oil 1, and b) LCO_2 + oil 2*

The influence of the LCO_2 and MQL flow rates on the media flow velocity is shown in Fig. 4. Regardless of the media flow rate, it can be observed that the media flow velocity of LCO_2 + MQL (oil 2) is slightly greater than the media flow velocity of LCO_2 + MQL (oil 1). The reason can be the level of dissolution between oil and LCO_2. Namely, the oil 2 is completely soluble in LCO_2, resulting in a mixture of LCO_2 + MQL (oil 2) that has higher average flow velocity than the two-phase flow of LCO_2 and oil 1. Oil 1, which is partially mixed with LCO_2, can slow down the entire stream of the two-phase mixture. In addition, oil that is not mixed with LCO_2 (i.e. oil 1), can adhere to the walls of the nozzle and thus possibly slow down the stream of the entire media. This can be illustrated schematically with Fig. 7 in section 2.2. Considering the error bars, however, it is not possible to notice significant difference between the velocity of the mixture of LCO_2 + MQL for different LCO_2 and oil flow rates. Nevertheless, by the increase in media mass flow rate through a nozzle of the same diameter, a higher flow velocity is expected, which describes marginal average velocity increasement with the higher LCO_2 mass flow rate. For example, flow velocity increases from 44 m/s to 49 m/s when the LCO_2 flow rate is increased from 100 g/min to 200 g/min with unchanged MQL flow rate of 60 ml/h.

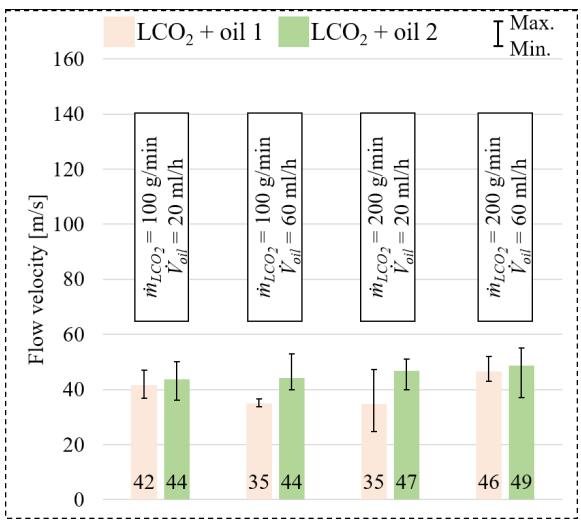

Fig. 4. *Average velocity of the media flow inside the supplying line*

2.2 High-Speed Camera Position B – Media Flow Analysis at the Nozzle Outlet

Fig. 5 shows stream of the media at the nozzle outlet. In addition, evolution of the droplet size during expansion of the mixture is visible in Fig. 6. For the mixture of LCO_2 + MQL (oil 1), oil droplets that are not part of the mixture can be observed, as they freely fly from the nozzle. Schematically, Fig. 7 illustrate this behavior of unmixed oil. It is clear that the portion of the oil, which does not mix with LCO_2, forms an oil film of variable thickness on the nozzle wall. At the nozzle outlet, the disintegration of this film occurs, resulting in a formation of oil droplets, which were captured by a high-speed camera. Similar

trend was observed for conventional MQL, where oil and pressurized air are not mixed and researchers [7] observed the formation of an oil film on the nozzle wall. As illustrated in Fig. 5, the diameter of the oil droplets increases with distance from the nozzle outlet. The reason lies in the nature of the carrier media LCO_2, which evaporates and expands (expansion rate of 535:1 [15]) due to the pressure drop from 57 bar in the supplying line to 1 bar at the nozzle outlet. Therefore, its volume and thus the size increases. On the other hand, oil droplets of oil 2 in the flow of LCO_2 are not visible due to the greater solubility between the oil and LCO_2. In addition, Fig. 8, shows that the LCO_2 flow with oil 2 is slightly faster than the flow with oil 1 as a consequence of the film-formation phenomena described in previous sections. However, significant increase in media flow velocity can be observed once the LCO_2 + MQL media leaves the supplying line (Figs. 4 and 8). The increase from an average of 40 m/s in the supplying line to the excess of 90 m/s at the nozzle outlet, regardless of the LCO_2 and MQL flow rates, can be observed due to the LCO_2 expansion and phase change from liquid to gas. This results in acceleration of the flow and thus higher flow velocity at the nozzle outlet compared to the flow velocity in the supplying line.

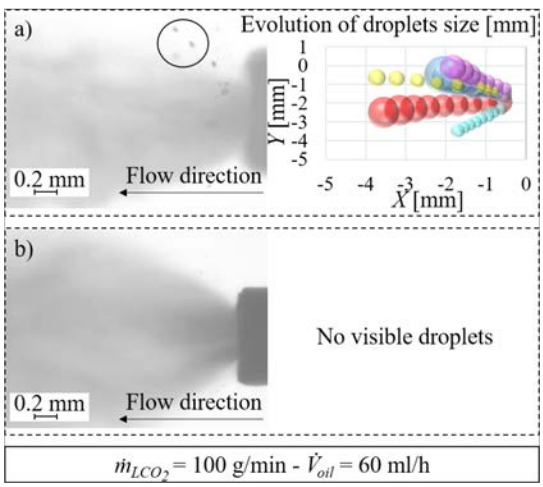

Fig. 5. *Media flow analysis at the nozzle outlet; a) LCO_2 + oil 1, and b) LCO_2 + oil 2*

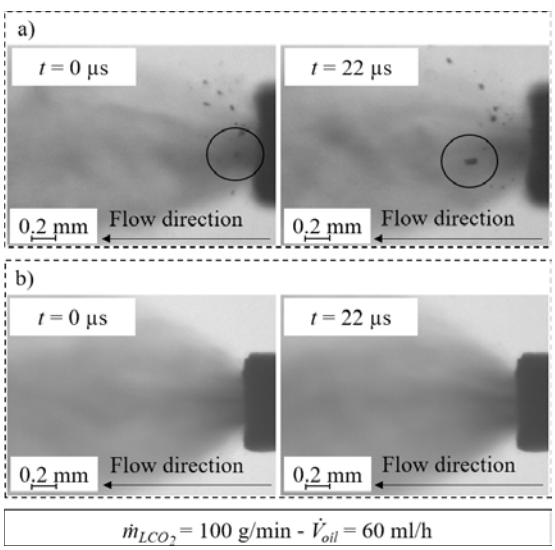

Fig. 6. *Evolution of the droplets size during mixture expansion at the nozzle outlet; a) LCO_2 + oil 1, and b) LCO_2 + oil 2*

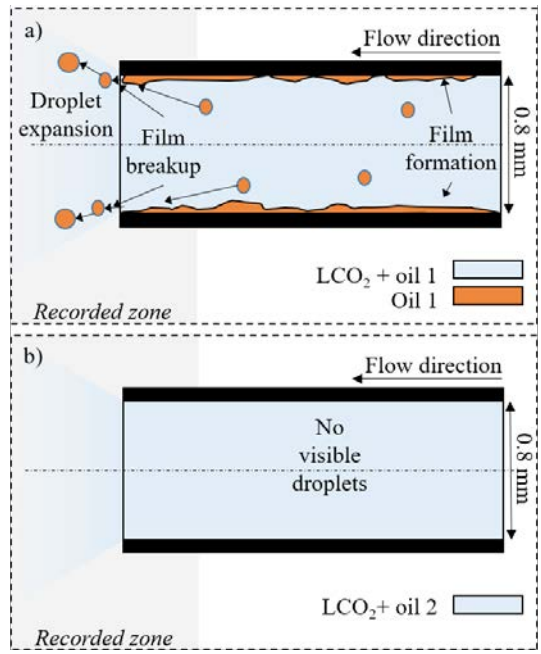

Fig. 7. *Oil behavior in the media flow at the nozzle outlet; a) LCO_2 + oil 1, and b) LCO_2 + oil 2*

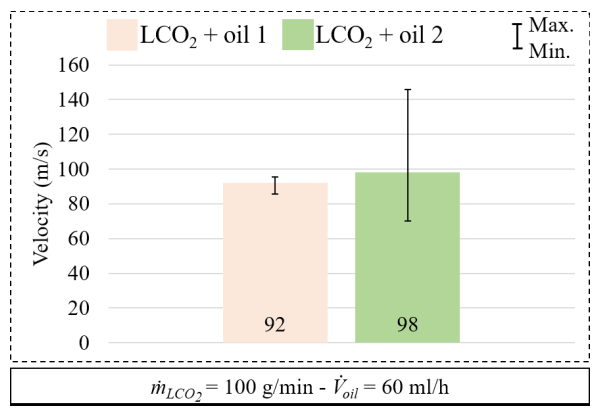

Fig. 8. *Average speed of the media flow at the nozzle outlet*

2.3 High-Speed Camera Position C – Media Flow Analysis at the Nozzle Outlet; Far from the Nozzle

Fig. 9 shows the media flow further from the nozzle outlet. The stream was recorded with a high-speed camera that was mounted at a distance of 3 mm from the outlet nozzle, as illustrated in Fig. 1. Following the observations from the high-speed camera positions A and B, the oil 2 droplets are not visible in the LCO_2 stream. Moreover, due to the spatial expansion of LCO_2, a smaller number of droplets of oil 1 can be observed in the stream. Oil droplets are smaller by comparing their size with the droplets right at the nozzle outlet (high-speed camera position B).

Illustration of the oil behavior in the LCO_2 stream is schematically shown in Fig. 10. As explained in section 2.2., the oil droplet size, after leaving the nozzle, increases due to the expansion of LCO_2. In addition, the average diameter of the droplet increases to a critical, unstable droplet size. Afterward, the decomposition of the droplet occurs, which means that the droplet breaks up into smaller droplets. It can be concluded that oil droplets entering the cutting zone are smaller than the droplets leaving the nozzle. On the other hand, no visible oil droplets in the LCO_2 flow can be seen when the oil 2 was used. This confirms that even though the oil flow rates are same, in case of oil 2, the average droplet size is significantly smaller and thus non-visible with selected camera settings. Nevertheless, our previous study [12] shows that mixture of LCO_2 and nonpolar oil (i.e. oil 2) provides oil droplets as small as 2 µm in diameter, compared to the larger oil droplets with excess of 5 µm in diameter for the mixture of LCO_2 and oil 1. In addition, due to the greater solubility of oil 2 in LCO_2, higher amount of oil enters the cutting zone. On the contrary, unmixed portion of the oil 1 is not part of the stream of LCO_2 + MQL and can freely fly from the nozzle, as observed at high-speed camera position B. This affects the amount of the oil, which has the ability to lubricate the cutting zone.

According to written, longer tool life is expected if the nonpolar oil (oil 2) is used in a mixture of LCO_2 + MQL. This observation is confirmed by tool life experiments [5], where tool life travel path of L_f = 36.6 m was achieved using single-channel supply of LCO_2 and nonpolar oil in cryogenic milling of titanium alloy Ti-6Al-4V (β). On the other hand, tool life travel path was shorter (L_f = 28.0 m) when the mixture of LCO_2 and polar oil was used. Furthermore, transition from conventional flood lubrication to LCO_2 assisted machining, if the nonpolar oil (oil 2) is used in pre-mixed LCO_2 + MQL, reflects in 44.7 % lower running costs, as the tool life is significantly prolonged (conventional flood lubrication; L_f = 13.6 m and LCO_2 assisted machining; L_f = 36.6 m) [16].

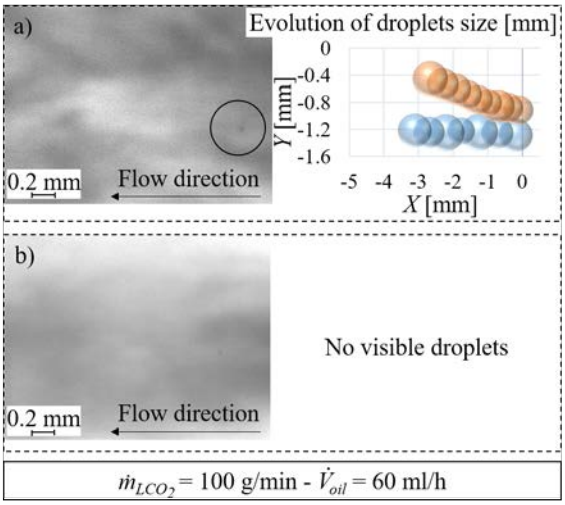

Fig. 9. *Media flow analysis at the nozzle outlet – far from the nozzle; a) LCO_2 + oil 1, and b) LCO_2 + oil 2*

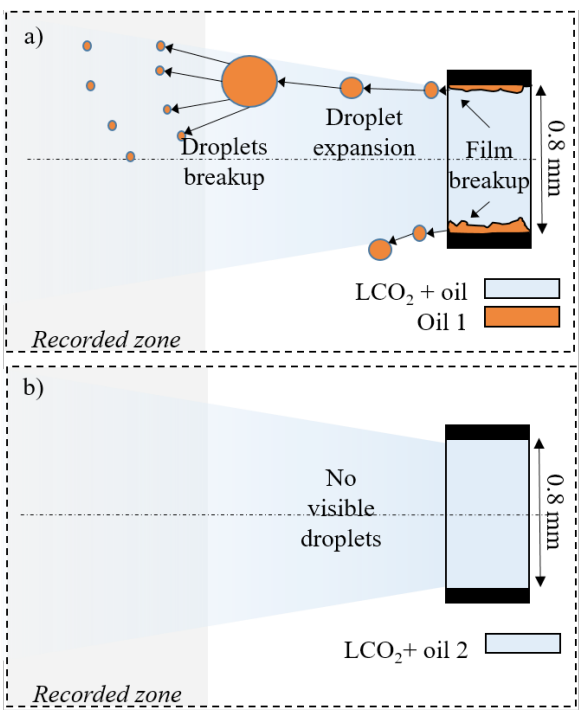

Fig. 10. *Oil behavior in the media flow at the nozzle outlet – far from the nozzle; a) LCO_2 + oil 1, and b) LCO_2 + oil 2*

3 CONCLUSIONS

In this paper, media flow analysis of pre-mixed LCO_2 and MQL (oil) was carried out. Media flow velocity

and oil droplet size were analysed using high-speed camera, wherein pre-mixed media flow was analysed inside the supplying line and at the nozzle outlet. For this research, two different oils were used in a mixture of LCO_2 + oil, i.e polar MQL oil (oil 1) and nonpolar MQL oil (oil 2). Key findings can be summarized, as follows.

Flow velocity of pre-mixed LCO_2 and oil is influenced by the LCO_2 flow rate. Thus, increase in LCO_2 mass flow rate increases the flow velocity, e.g. flow velocity increases from 44 m/s to 49 m/s when the LCO_2 flow rate is increased from 100 g/min to 200 g/min with unchanged MQL flow rate of 60 ml/h. However, the flow velocity of a mixture of LCO_2 and oil is largely influenced by the pressure drop and LCO_2 expansion upon the nozzle outlet. Media flow velocity increases significantly from an average of 40 m/s in the supplying line to the excess of 90 m/s at the nozzle outlet.

LCO_2 expansion upon the nozzle outlet has an impact on oil droplet size as well. Due to the LCO_2 expansion, the size of the oil droplet increases to the point of critical, unstable droplet size. Afterward, the unstable oil droplet breaks up into smaller oil droplets. Besides, oil droplet size in the pre-mixed media is largely dependent on the solubility between oil and LCO_2. Solubility of nonpolar oil (oil 2) is greater compared to the polar oil (oil 1). Thus, mixture of LCO_2 and oil 2 provides oil droplets as small as 2 μm in diameter. On the contrary, mixture of LCO_2 and oil 1 provides oil droplets with excess of 5 μm in diameter. In addition, limited oil solubility yields towards unmixed portion of the oil 1 (oil which is not part of the LCO_2 + MQL stream), which can freely fly from the nozzle, with lower possibilities for entering the cutting zone. In combination with larger oil droplets this affects the lubrication capability in LCO_2 assisted machining, as described further in conclusions.

The contribution of this study is reflected in an enhanced understanding of LCO_2 and oil behavior for practical use of LCO_2 assisted machining. To realize the longest tool life, therefore, a nonpolar oil (i.e. oil 2) should be used in the mixture of LCO_2 + MQL. In our study, tool life travel path of L_f = 36.6 m was achieved using single-channel supply of LCO_2 and nonpolar oil in milling of titanium alloy Ti-6Al-4V (β). On the other hand, tool life travel path was shorter (L_f = 28.0 m) when the mixture of LCO_2 and polar oil was used.

Future work requires deeper investigations into LCO_2 assisted machining, wherein nonpolar oil (oil 2) should be used in the pre-mixed LCO_2 + MQL. LCO_2 and MQL flow rates should be varied and tool life experiments for other difficult-to-cut materials, such as Inconel 718, stainless steel 316 L, etc. should be investigated. In addition, surface topography and cutting forces should be analysed.

4 ACKNOWLEDGEMENTS

Acknowledgements to the Slovenian Research Agency (*ARRS*) for founding research project *L2-8184* and research program *P2-0266*. Acknowledgements also to the Laboratory for water and turbine machines (*LVTS*) at the Faculty of Mechanical Engineering, Ljubljana for supporting the experimental work. Authors would like to acknowledge also the companies *Rhenus Lub* and *Kemol* for supporting this work.

5 REFERENCES

[1] Khawaja, A.H., Jahanzaib, M., Cheema, T.A. (2020). High-speed machining parametric optimization of 15CDV6 HSLA steel under minimum quantity and flood lubrication. *Advances in Production Engineering & Management*, vol. 15, no. 4, p. 403-415, **DOI:10.14743/apem2020.4.374**.

[2] Shah, P., Khanna, N., Zadafiya, K., Bhalodiya, M., Maruda, R.W., Krolczyk, G.M. (2020). In-house development of eco-friendly lubrication techniques (EMQL, Nanoparticles+EMQL and EL) for improving machining performance of 15–5 PHSS. *Tribology International*, vol. 151, p. 106476, **DOI:10.1016/j.triboint.2020.106476**.

[3] Gupta, M.K., Song, Q., Liu, Z., Sarikaya, M., Jamil, M., Mia, M., Khanna, N., Krolczyk, G.M. (2021). Experimental characterisation of the performance of hybrid cryo-lubrication assisted turning of Ti–6Al–4V alloy. *Tribology International*, vol. 153, p. 106582, **DOI:10.1016/j.triboint.2020.106582**.

[4] Jawahir, S., Attia, H., Biermann, D., Duflou, J., Klocke, F., Meyer, D., Newman, S.T., Pušavec, F., Putz, M., Rech, J., Schulze, V., Umbrello, D. (2016). Cryogenic manufacturing processes. *CIRP Annals – Manufacturing Technologies*, vol. 65, no. 2, p. 713-736, **DOI:10.1016/j.cirp.2016.06.007**.

[5] Bergs, T., Pušavec, F., Koch, M., Grguraš, D., Döbbeler, B., Klocke, F. (2019). Investigation of the solubility of liquid CO2 and liquid oil to realize an internal single channel supply in milling of Ti6Al4V. *Procedia Manufacturing*, vol. 33, p. 200-207, **DOI:10.1016/j.promfg.2019.04.024**.

[6] Pušavec, F., Grguraš, D., Koch, M., Krajnik, P. (2019). Cooling capability of liquid nitrogen and carbon dioxide in cryogenic milling. *CIRP Annals – Manufacturing Technology*, vol. 68, no. 1, p. 73-76, **DOI:10.1016/j.cirp.2019.03.016**.

[7] Cabanettes, F., Faverjo, P., Sova, A., Dumont, F., Rech, J. (2017). MQL machining: from mist generation to tribological behavior of different oils. *International Journal of Advanced Manufacturing Technology*, vol. 90, p. 1119-1130, **DOI:10.1007/s00170-016-9436-0**.

[8] Muaz, M., Choudhury, S.K. (2019). Experimental investigations and multi-objective optimization of MQL-assisted milling

process for finishing of AISI 4340 steel. *Measurement*, vol. 138, p. 557-569, **DOI:10.1016/j.measurement.2019.02.048**.

[9] Maruda, R.W., Krolczyk, G.M., Feldshtein, E., Pušavec, F., Szydlowski, M., Legutko, S., Sobczak-Kupiec, A. (2016). A study on droplets sizes, their distribution and heat exchange for minimum quantity cooling lubrication (MQCL). *International Journal of Machine Tools and Manufacture*, vol. 100, p. 81-92, **DOI:10.1016/j.ijmachtools.2015.10.008**.

[10] Park, K.H., Olortegui-Yume, J., Yoon, M.C., Kwon, P. (2010). A study on droplets and their distribution for minimum quantity lubrication (MQL). *International Journal of Machine Tools and Manufacture*, vol. 50, no. 9, p. 824-833, **DOI:10.1016/j.ijmachtools.2010.05.001**.

[11] Maruda, R.W., Feldshtein, E., Legutko, S., Krolczyk, G.M. (2015). Research on emulsion mist generation in the conditions of minimum quantity cooling lubrication (MQCL). *Tehnički vjesnik – Technical Gazette*, vol. 22, no. 5, p. 1213-1218, **DOI:10.17559/TV-20140423221850**.

[12] Grguraš, D., Sterle, L., Krajnik, P., Pušavec, F. (2019). A novel cryogenic machining concept based on a lubricated liquid carbon dioxide. *International Journal of Machine Tools and Manufacture*, vol. 145, art. ID. 103456, **DOI:10.1016/j.ijmachtools.2019.103456**.

[13] Cordes, S., Hübner, F., Schaarschmidt, T. (2014). Next generation high performance cutting by use of carbon dioxide as cryogenics. *Procedia CIRP*, vol. 14, p. 401-405, **DOI:10.1016/j.procir.2014.03.091**.

[14] Samatham, M., Sheavan, A., Vidyanand, P., Reddy, G.S. (2016). A critical review on minimum quantity lubrication (MQL) coolant system for machining operations. *International Journal of Current Engineering and Technology*, vol. 6, no. 5, p. 1745-1751.

[15] Busch, K., Hochmuth, C., Pause, B., Stoll, A., Wertheim, R. (2016). Investigation of cooling and lubrication strategies for machining high-temperature alloys. *Procedia CIRP*, vol. 41, p. 835-840, **DOI:10.1016/j.procir.2015.10.005**.

[16] Sterle, L., Grguraš, D., Kern, M., Pušavec, F. (2019). Sustainability Assesment of Advanced Machining Technologies. *Strojniški vestnik – Journal of Mechanical Engineering*, vol. 65, no. 11-12, p. 671-679, **DOI:10.5545/sv-jme.2019.6351**.

Strojniški vestnik - Journal of Mechanical Engineering 67(2021)1-2, 11-26

DOI:10.5545/sv-jme.2020.6946 Original Scientific Paper
Received for review: 2020-09-23
Received revised form: 2020-11-20
Accepted for publication: 2020-12-09

Relationship between Tire Ground Characteristics and Vibration Noise

Haichao Zhou[1,*] – Huiyun Li[1] – Chen Liang[1] – Lingxin Zhang[2] – Guolin Wang[1]
[1] Jiangsu University, School of Automotive and Traffic Engineering, China
[2] AEOLUS Tyre Co. Ltd, China

To study the relationship between tire ground characteristic parameters and vibration noise, a radial truck tire (295/80R22.5) is selected as the research object, and a finite element model is established. The test results of the tire stiffness, vibration modal, and surface velocity response are used to verify the model. In order to find the influence of the inherent vibration characteristics of a tire on radiated noise, the contour design and belt design are selected as design schemes, and a modal analysis and vibration noise numerical simulation analysis are carried out for different tire structures. The footprints of the tire-ground are refined and divided. All the grounding parameters of each subarea are extracted, and the relationships between the geometric and mechanical parameters of the tire ground characteristics and vibration noise are investigated. Then, the effects of the skewness and stiffness of tread deformation, as well as the spectral density of tire–road excitation force power on vibration noise, are analysed. The results showed that a positive correlation exists between the vibration noise and the skewness of the tread radial deformation; however, a negative correlation is observed between the vibration noise and radial deformation stiffness. The peak values and numbers of the tire excitation force power spectral density using the minimum noise structure design are significantly smaller than those of the original tire. This study can serve as a theoretical guideline for the structural design of low-noise tires.
Keywords: tire noise, ground characteristic parameters, numerical simulation, modal analysis, tread stiffness, power spectral density

Highlights
- *Tire dynamic model is established and validated, and tire vibration noise model is introduced.*
- *The effects of tire contour profiles and belt structures on vibration noise are compared and analysed, and the geometric and mechanical parameters of tire ground characteristics are introduced.*
- *Relationships between tire ground characteristics and tire vibration noise are established.*
- *The mechanisms of the reduction of tire vibration noise are analysed based on the tread radial deformations and excitation force power spectral density.*

0 INTRODUCTION

Noise pollution produced by vehicles is a prominent issue in modern society, especially for the inhabitants of urban areas. Studies have shown that road traffic noise is a remarkably complex phenomenon, with different sources such as the power unit, aerodynamics, and tire–road interaction [1] and [2]. According to statistics, when heavy trucks travel at speeds of more than 70 km/h, tire noise becomes the main source of noise of a vehicle [3]. A combination of vibrodynamic and aerodynamic phenomena occurs during the generation of tire noise, when the tire and road come into contact. The vibration noise originating from vibrodynamic phenomena has a frequency lower than 1 kHz and is due to tire vibrations arising from the contact of the tires with irregularities in the road surface [4]. To reduce tire noise, the European Union, the United States, Japan, and China have passed laws and regulations, with clear requirements and implementation periods for improvements to noise performance. Therefore, the development of low-noise tires is of practical significance and has value as an engineering guideline.

The main source of noise in truck and bus radial (TBR) tires is structural vibration [5] and [6]. The vibration of a tire is mainly caused by the external and internal excitation of the tire. Dubois et al. [7] used a flat plate and thin shell model to simplify a tire and obtain the excitation force of it when it rolls on a road surface, and they calculated the vibration noise under this exciting force. Belgacem et al. [6] noted that the vibration noise of a tire can be predicted by using the Helmholtz equation and that reducing the tire excitation force can reduce tire vibration noise. Zhou et al. [8] studied the influence of the belt structure on tire vibration and noise; they found that optimizing the belt helped reduce the acceleration peak of the tread and sidewall and decrease the tire noise. Wang et al. [9] researched the effects of the tread design parameters on tire vibration noise and found that the tread is the main acoustic component that contributes to tire noise.

Tires are the only parts of a vehicle that come into contact with the road surface, and therefore, tire

*Corr. Author's Address: Jiangsu University, School of Automotive and Traffic Engineering, Zhenjiang, China, hczhou@ujs.edu.cn

ground characteristics are the integrative reflections of tire performance, including roll resistance, tire noise, tire wear, and hydroplaning [10] and [11]. Tire ground characteristics have a direct and considerable impact on tire properties, but the extent of the influence of different parameters on tire performances is different. Analysing tire ground characteristics helps to understand the interaction between tire and road, which is beneficial to tire structure design and pavement development [12]. Tire ground characteristics can be divided into the geometric parameters and mechanical parameters, and these parameters greatly influence contact pressure and grip performance [13]. Wang et al. [14] controlled the tread deformation to decrease stress concentration and increase contact pressure uniformity, which resulted in the improvement of tire grip. Liang [15] explored the effects of tire contour shape on tire noise and found that the contour structure reduces tire noise owing to its effect on tire contact pressure distribution. Hubbell [16] proposed that the ground shape factor be chosen to evaluate the tire noise level in the footprint and concluded that tire vibration noise changes with the ground shape factor changes. Cesbron et al. [17] studied the relationship between ground pressure distribution of a radial tire and the outdoor noise test, it is found that the two properties between 500 Hz and 1000 Hz had a strong correlation. Cohn [18] used different inflation pressure to analyse tire ground and roll resistance, demonstrating an obvious correlation between them.

As mentioned above, the previous studies have mainly focused on tire noise analysis or the effects of structural design, and have analysed the relationship between tire noise and tire–road surface. However, in-depth studies on the relationships between the vibration noise and ground characteristic parameters have not been conducted.

Therefore, the aim of this study is to investigate the effects of the structural parameters of a tire on tire noise and ground characteristic parameters and establish a relationship between tire noise and ground characteristics. A series of tire structures schemes, including tire contour profiles and belt plies, are designed using the orthogonal experimental design method. Additionally, the noise characteristics and ground characteristics of tires of different structures are analysed. Finally, the tread deformation skewness and stiffness are compared, and the power spectral density of the tire radial excitation force of the minimum noise design is compared with that of the original design. This research aims to improve efficiency in the design of low-noise tires.

1 TIRE MODEL ESTABLISH AND VIBRATION NOISE ANALYSIS

1.1 Tire Modelling and Verification

A three-dimensional finite element model of the radial truck tire (295/80R22.5) is established under the inflation pressure 900 kPa, with a load of 35,500 N, as shown in Fig. 1. The rubber is an isotropic hyper-elastic material and can be described by the Yeoh model. The steel cord is considered an isotropic material. The cord-rubber composite is modelled with rebar layers, such as belts and carcasses. The rim and road are defined as analytical rigid bodies, and the tire loading process is implemented by moving the road surface to a special position until a given force is attained. To verify the validity of the finite element model, measuring of the tire stiffness in three directions is carried out by using the MTM-2 tire testing machine. The details on the simulation method and testing process are presented in [19]. Fig. 2 shows a comparison of the three different load-deflection characteristics between simulation and test. It can be seen that the simulation results are in good agreement with the test data.

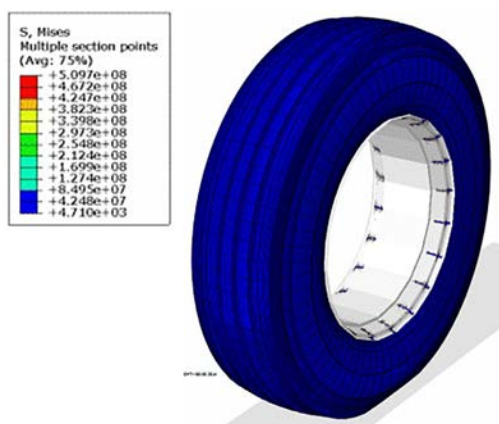

Fig. 1. *Three-dimensional finite element model of tire*

The dynamic characteristics of a tire have a considerable impact on tire vibration noise. Therefore, a dynamic signal analyser is used to measure the vibration modal characteristics of the tire, as shown in Fig. 3. Because that there are 81 vibration response points on the tread, the free model characteristics of the tire are obtained only in the radial direction. In Abaqus software, the Block Lanczos method is used to calculate the natural frequency. Table 1 presents a comparison between the measured and predicted tire modal frequencies; it can be seen that there is a good agreement between the measured and predicted

Table 1. *Comparison of radial modal characteristics between simulated and tested*

Radial order	1	2	3	4	5	6
Test result [Hz]	83.63	94.63	113.18	132.48	153.12	173.97
Simulation result [Hz]	81.78	91.57	109.75	128.9	149.08	169.6
Error [%]	–2.21	–3.	–3.03%	–2.70	–2.64	–2.51

natural frequencies of the former six modals, with a maximum error of 3.2 %.

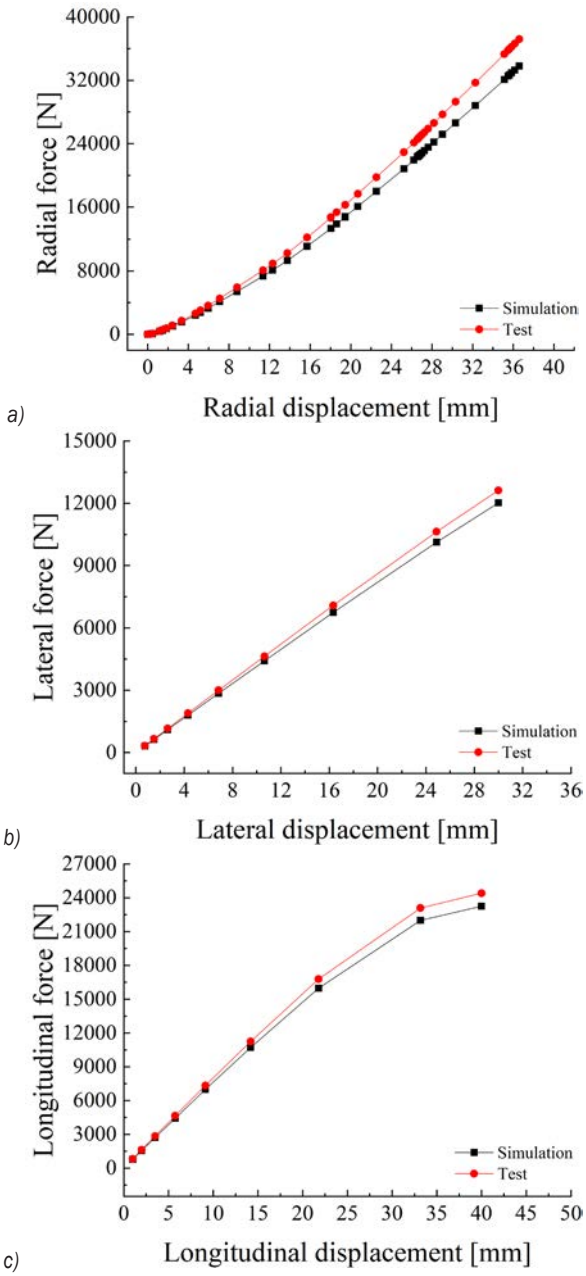

Fig. 2. *Comparison of tire load-deflection characteristics between simulation and measurement; a) radial; b) lateral; and c) longitudinal forces and displacements*

According to boundary element theory, the characteristic of the vibration response of a rolling tire is the main source of tire vibration noise **[20]**. Because of limitations in the dimensions that of the tire drum tester, the surface vibration response of a 215/75R17.5 tire is selected for testing. The simulation and test results are then compared to validate the tire dynamic model established in this study. The tire is loaded on the tire drum test machine, as shown in Fig. 4. During the test, the tire load is 10,000 N, the air pressure is 830 kPa, and the rolling speed is 30 km/h. A Polytec single-point laser Doppler vibrometer is used to measure the vibration of the tire sidewall. The test time and sampling frequency are 1.28 s and 1024 Hz, respectively.

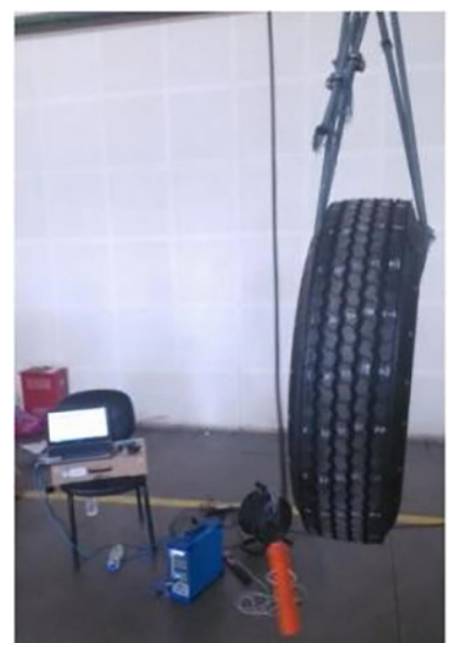

Fig. 3. *Overview of tire modal test*

During the test, the laser Doppler vibrometer is fixed on a tripod and connected to a computer through a data collector, as shown in Fig. 4. The tripod is placed approximately 50 cm from the tire, and a laser beam is focused onto the sidewall measurement point, the focusing knob is turned, and the position of the tripod is adjusted for performing the measurement at different points.

Abaqus/Explicit is used to simulate the rolling of the tire at 30 km/h. Four points on the sidewall of the rolling tire are measured to analyse the vibration characteristics of the sidewall, as shown in Fig. 4. The positive direction of the *z*-axis is the direction towards the ground, and the angle of the measuring point is the angle between the straight line connected by the measuring point and the positive direction

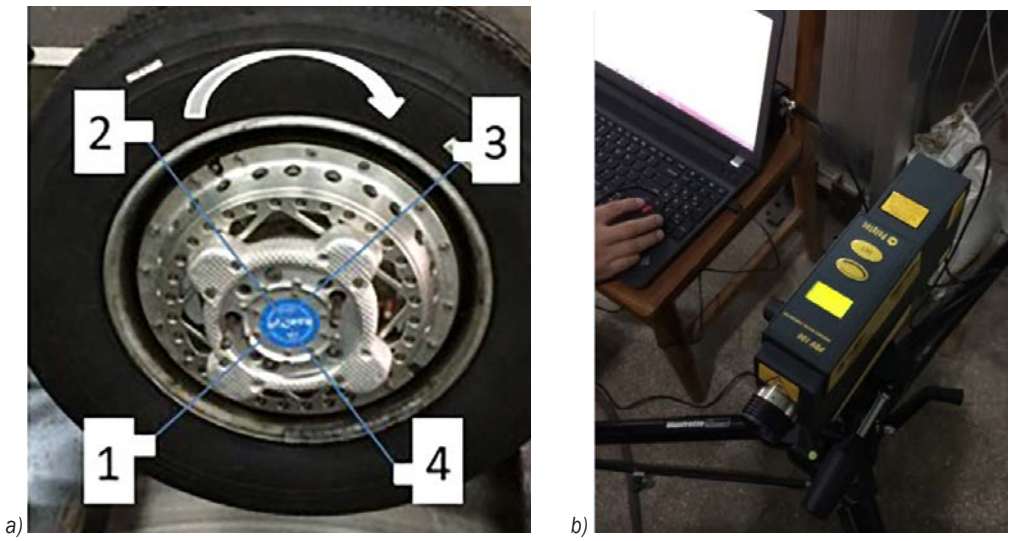

a) b)

Fig. 4. *Experiment to measure vibration response of the rolling tire; a) placement of vibration measurement points for test tire; and b) laser Doppler vibrometer*

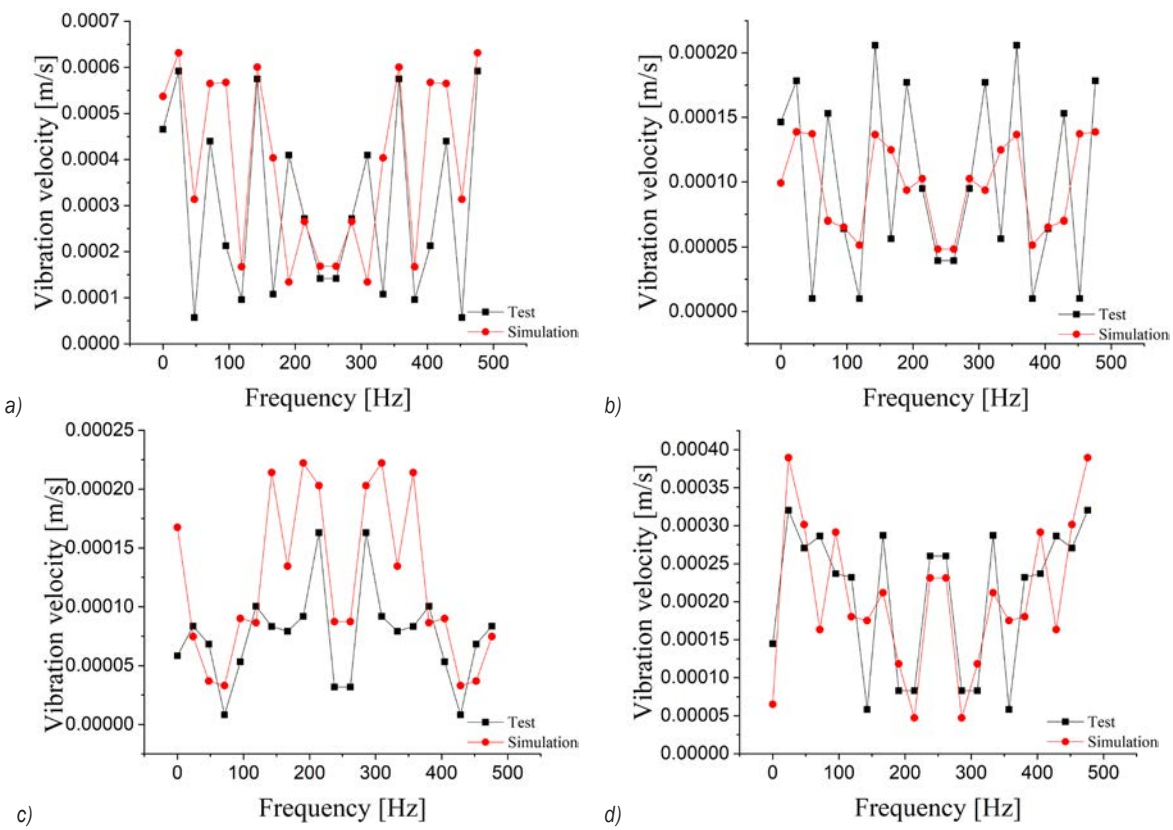

Fig. 5. *Comparison of vibration responses between simulation and measurement in the frequency domain; comparison of test and simulation at measurement a) point 1; b) point 2; c) point 3; and d) point 4*

of the *z*-axis. The angles of the four measurement points were in the *xz* coordinate plane are 45°, 135°, 225°, and 315° in the clockwise direction. The first measurement point is the grounding rear end, and the fourth measurement point is the grounding front end. In order to better compare the test results with the simulation results, the signal in the time domain is subjected to a discrete Fourier transform to obtain the vibration velocity curve in the frequency domain. The results are shown in Fig. 5. It can be seen that the distributions of the vibration velocity obtained in the simulation are in good agreement with those in the test.

1.2 Numerical Analysis of Tire Vibration Noise

A numerical analysis of the tire vibration noise is conducted using the boundary element method. A surface mesh used for noise simulation is extracted from the finite element model of the loaded tire presented Fig. 1. To avoid leakage of acoustic energy, the acoustic boundary element model is sealed by simply meshing the round edges in contact with the rim, as shown in Fig. 6.

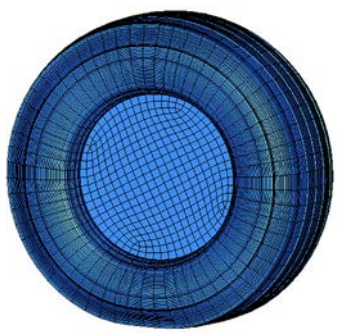

Fig. 6. *Boundary element model of a tire*

According to the GB/T3767-1999 standard, 19 observation points (OP) are distributed on a semi-sphere with a radius of 1 m. The sound pressure level of tire vibration noise is the superposition of A-weighted sound levels from the 19 observation points. The acoustic analysis model and distribution of observation points are shown in Fig. 7. The road surface is treated as a rigid reflection surface.

In this study, the rolling of a tire is simulated using Abaqus/Explicit, and the radial force of the rim centre under steady-state rolling is extracted as the excitation force to carry out noise simulation. The change in the radial excitation force of rim centre over time is shown in Fig. 8.

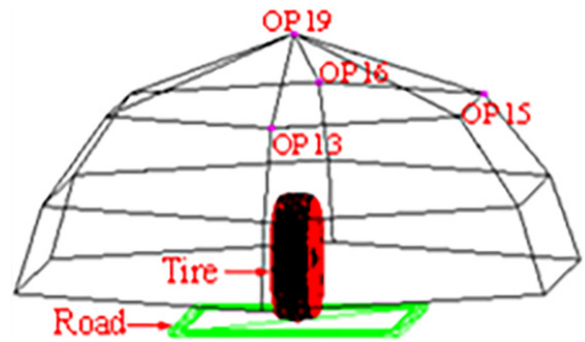

Fig. 7. *Acoustic prediction model and acoustic pressure observation points (OP)*

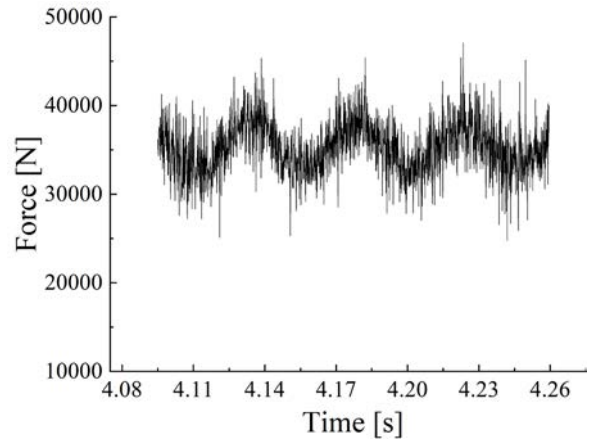

Fig. 8. *Radial excitation force of the rim centre in time domain*

A fast Fourier transform is applied to the radial excitation force in the time domain to derive the excitation force in the frequency domain, which is required to calculate the tire vibration noise, as shown in Fig. 9.

The excitation force of the rim centre in the frequency domain is imposed on the centre point of the tire ground contact patch. The results of the modal simulation are imported for calculating the modal participation factors. The LMS Virtual Lab acoustic software is used to simulate tire noise, the data at the nodes of the tire surface are transferred onto the acoustic mesh via data mapping, and the sound pressure value in the range 20 Hz to 500 Hz is computed using the modal acoustic transfer vector (MATV) method. The MATV method expresses the acoustic transfer function in modal coordinates from a radiating structure to a field point and, therefore, lists the acoustic contribution from each structural modal [21]. With the help of the MATV method, the structural modal matrix is multiplied for the modal coordinates under the LMS Virtual Lab acoustic software to compute noise.

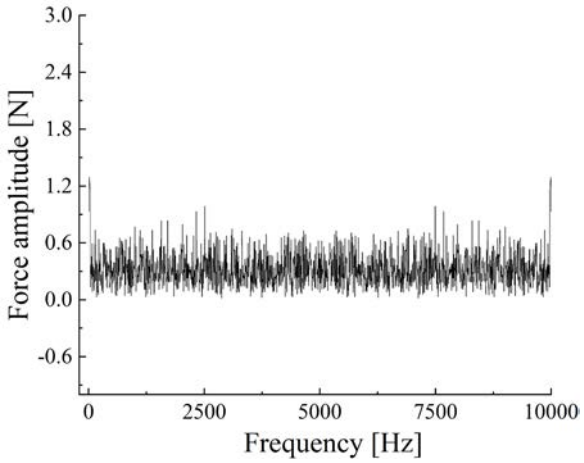

Fig. 9. *Radial excitation force of the rim centre in frequency domain*

After the selection of the observation points corresponding to the front end of the contact patch (OP13), the rear end (OP16), the top end (OP19), and the right sidewall (OP15), the distribution characteristics of vibration noise are shown in Fig. 10.

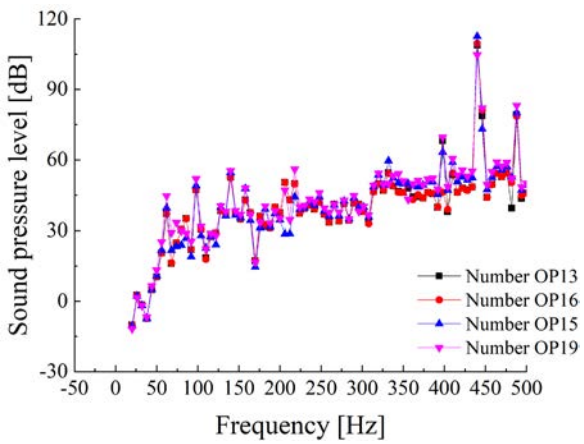

Fig. 10. *Spectral curves of different acoustic observation points*

Fig. 10 shows that the variation trends of the frequency-response function at different OPs are similar, whereas those of the sound pressures differ slightly. The peak noise values are mainly concentrated at 440 Hz and 488 Hz. The sound pressure at the rear end of the contact patch (OP16) is higher than that at the front end of the contact patch (OP13), which is consistent with the results of experiments in **[22]** and **[23]**.

2 EFFECTS OF TIRE STRUCTURE DESIGN ON VIBRATION NOISE

2.1 New Non-Natural Equilibrium Contour Design

The early tire contour design theory only considers the static characteristics of the tire; it does not consider the influence of tire manufacture factors on the tire-building process or the role of the strengthening layer and the belt on the inflation pressure. Therefore, the early tire contour design theory has some limitations in the modern structural design of the tire. More than 50 years after the tire contour design theory was proposed, Sakai proposed a theory for the non-natural equilibrium contour design of tires **[24]**, and inspired Sakai's theory, a new non-natural equilibrium contour (NEC) design theory is proposed in this work, and the structure contour of a tire 295/80R22.5 is drawn using Matlab software, as shown in Fig. 11. The new non-natural equilibrium contour can effectively inhibit shoulder deformation, and increase the ground pressure distribution, and obtain a more reasonable contact shape **[25]**.

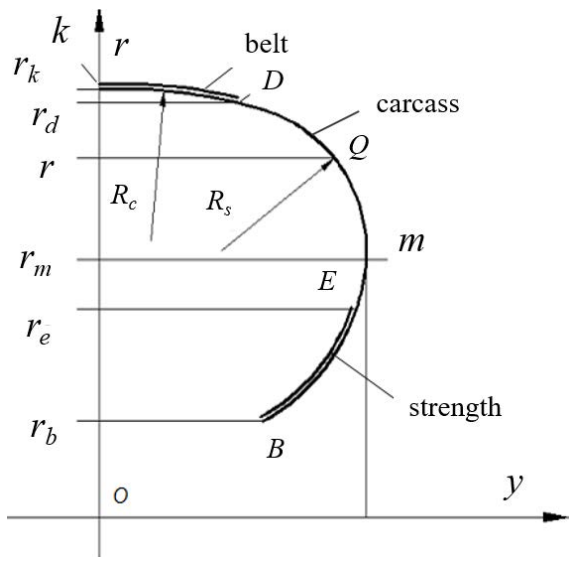

Fig. 11. *Tire contour structure with belt layer and strength layer*

In Fig. 11, R_c is the curvature radius of the belt section, R_s is the curvature radius of the carcass section, r_d refers to the radius of the belt layer with respect to the axis of rotation, r_m refers to the radius of the maximum width point with respect to the axis of rotation in the tire section, τ_0 refers to the belt layer pressure rate, r_k refers to the radius of the tire tread with respect to the axis of rotation, and α refers to the shape coefficient of the belt layer pressure rate.

Variables r_d, τ_0, r_k, and α are chosen as design variables that have a significant effect on the tire contour shape. Here, the orthogonal array (OA) is chosen to generate the design sample points [26]. The three levels of design variable r_d are 483.13 mm, 485.13 mm and 487.13 mm, the three levels of design variable τ_0 are 0.7, 0.8 and 0.9, the three levels of design variable r_k are 491.94 mm, 493.94 mm and 495.94 mm, the three levels of design variable α are 0.1, 0.2 and 0.3. According to the variables and levels, an OA table of $L_9(3^4)$ is generated. With the help of the analysis methods in Chapter 1, the modal frequencies and vibration noise of the different contour design schemes are listed in Table 2.

The range analysis can evaluate the influence of design variables on the sound pressure level (SPL), identify them as primary and secondary, and work out the optimal level combination of the design variables to obtain the most superior performance index from all the sample points. With the help of range analysis, the minimum noise value is obtained by optimizing tire contour design was 81.73 dB.

Table 2. *Former six-order natural frequencies and SPL of different NEC designs*

	Natural frequency [Hz]						Noise
No.	1	2	3	4	5	6	[dB]
1	60.81	82.26	98.46	114.18	129.29	142.75	82.95
2	59.40	80.74	97.13	113.08	128.34	141.79	84.13
3	57.84	78.93	95.42	111.61	127.14	140.72	95.91
4	57.92	79.02	95.43	111.50	126.94	140.59	89.34
5	58.15	79.62	96.23	112.29	127.64	141.25	83.64
6	59.01	80.53	96.97	112.80	127.88	141.19	90.63
7	56.75	78.04	94.67	110.81	126.25	139.94	94.24
8	57.59	78.91	95.37	111.28	126.46	139.87	88.00
9	58.44	79.86	96.21	111.95	126.98	140.41	86.60

2.2 Belt Structure Design

The tire belt structure determines the bearing capacity and stiffness of the tire, and the tire contact pressure, distribution depends on the belt structural design [23]. The tire contact pressure distribution in turn affects the exciting force and consequently affects the vibration noise of the tire. Therefore, the relationship between ground characteristics and vibration noise can be studied by varying the structural design of the tire belt. The structural parameters of the belt include the thickness, width, and length of the belt; the angle of the cord; the density and arrangement; the number of plies; and the type and structure of the cord used. The tire 295/80R22.5 model consists of four belt layers (4-ply tire), but the main parts of the belt are the second and third layers when the tire is rolled. Therefore, taking the second belt layer and the third belt layer as the analysis objects in this work, the influence of the width and angle of the belt layers on the vibration noise are analysed by using the OA table of $L_9(3^4)$. In the orthogonal experiment, the three levels of the width of the second belt layer are 192 mm, 198 mm and 204 mm, the three levels of the angle of the second belt layer are 12°, 15° and 18°; the three levels of the width of the third belt layer are 114 mm, 120 mm and 126 mm, three levels of the angle of the third belt layer are –12°, –15° and –18°. The former six-order modals frequencies and vibration noise of the different belt layer design schemes are listed in Table 3. With the help of the range analysis, the minimum noise value obtained by optimizing belt structure design is 84.22 dB.

Table 3. *Former six-order natural frequencies and SPL of different belt structure*

	Natural frequency [Hz]						Noise
No.	1	2	3	4	5	6	[dB]
1	60.98	82.12	97.64	112.52	126.74	139.26	85.01
2	61.02	82.16	97.71	112.56	126.71	139.21	87.63
3	60.95	82.11	97.69	112.57	126.75	139.27	91.03
4	60.92	82.02	97.53	112.39	126.63	139.35	89.30
5	61.02	82.14	97.63	112.47	126.70	139.43	135.97
6	60.88	82.00	97.55	112.45	126.72	139.42	95.52
7	60.96	82.02	97.47	112.32	126.64	139.57	127.42
8	60.90	81.98	97.45	112.30	126.61	139.49	121.59
9	60.88	81.97	97.46	112.35	126.69	139.62	98.20

3 RESULT ANALYSES AND DISCUSSION

3.1 Relationship between Ground Parameters and Vibration Noise

3.1.1 Definition of Tire Ground Parameters

The distribution characteristics of the tire ground pressure are evaluated using the Tire Footprint Analysis System (TFAS) software, which is a database analysis system that our team developed; the detail ground characteristics are shown in Fig. 12, and the detailed parameters description of the geometric and mechanical parameters of tire ground characteristics is presented in [15] and [27].

In Fig. 12, α_1, α_2, α_3 and α_4 are the four outer angles of the geometry shape of the tire contact with the ground, respectively. The shape coefficient of the tire-ground F_{sr} represents the ratio of the sum of external angles of the footprint geometry to 360° F_{sr}

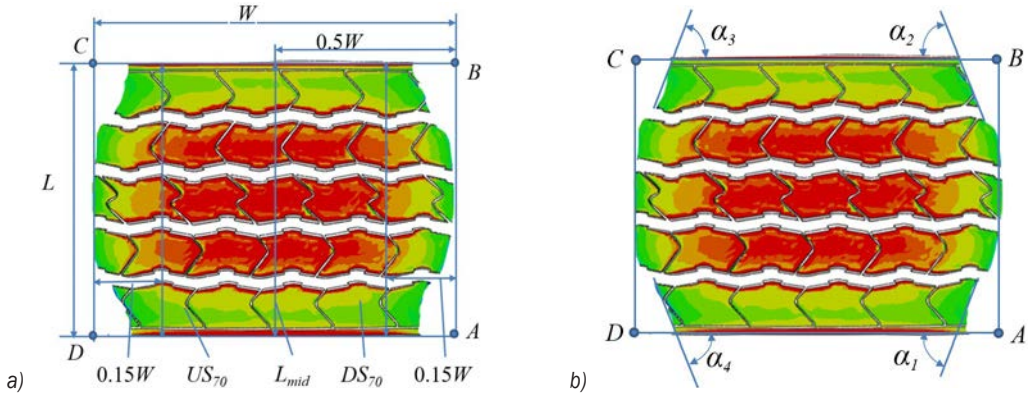

Fig. 12. *Tire ground characteristics parameters; a) tire ground geometric parameters; and b) the four outer angles of the tire contact with the ground*

can be calculated using Eq. (1). If F_{sr} is higher than 1, the footprint shape is concave; if F_{sr} is lower than 1, the footprint shape is convex; and if F_{sr} is equal to 1, the footprint shape is rectangular.

$$F_{sr} = A/360° = \left(\alpha_1 + \alpha_2 + \alpha_3 + \alpha_4\right)/360°. \quad (1)$$

The US_{70} and DS_{70} are the second-longest axis, their locations are 0.15 times the contact width W nearby the edges. L_{mid} is the third-longest axis in the middle of tire contact area. Then, the coefficient of the second-longest axis DOF_{avg} and the coefficient of the third-longest axis LF_{avg} are obtained using Eq. (2). AB and CD are the lengths of the edges of the tire-ground in the lateral direction. L is the maximum length of the tire–ground in the rolling direction, and W is the maximum width of the tire–ground in the lateral direction. $\bar{P}$ is the average contact pressure in the tire-ground zone, which is obtained by dividing the load by the contact area.

$$\begin{cases} DOF_{avg} = 0.5 \times \left(\dfrac{AB}{DS_{70}} + \dfrac{CD}{US_{70}} \right) \\ LF_{avg} = 0.5 \times \left(\dfrac{L_{mid}}{DS_{70}} + \dfrac{L_{mid}}{US_{70}} \right) \end{cases}. \quad (2)$$

When the ratio of the tire height to width is greater than 60 %, the shape factor of the tire–ground proposed by the Goodyear Tire Company can be used to evaluate the noise level [16]. The shape factor characterizes the specific tire footprint configuration by using the relationship between the maximum length of the footprint in the rolling direction and the lengths of the first and second lateral edges at a fixed location in the tire width direction with a fixed location. It can be used to describe the potential noise level generated during the rotation of a tire contacting a road surface. Inspired by the idea proposed by Goodyear, the ground shape factor $FSF_{70\%}$ is selected to describe the potential noise level generated during the rotation of a tire contacting a road surface, as shown in Eq. (3):

$$FSF_{70\%} = \frac{L_{mid}}{US_{70} + DS_{70}}. \quad (3)$$

3.1.2 Analysis of Ground Parameters

Table 4 lists the tire ground parameters in each of the schemes of contour designs and belt structures. In the Table 4, the principle of the rowsis in accordance with the noise values, in other words, the first row corresponds to the lowest noise value, and the last row corresponds to the highest noise value.. The superscript number in Table 4 indicates the corresponding program number listed in Table 2 and Table 3. Taking the NEC[1] as an example, it means the number 1 of NEC design.

The statistical analysis method is used to analyse the relationship between ground parameters and tire noise. Fig. 13 shows a scatter diagram of the relationship between the geometric and mechanical parameters of the tire ground and noise. It can draw a relationship from the figure as the followings:

1. The tire vibration noise will increase sharply under the contact area is larger than 49,000 mm², which means that the contact area should be controlled within a reasonable range. If it exceeds a certain value, the noise will increase considerably.
2. As the third-longest axis and the third-longest axis coefficient LF_{avg} increase, the vibration noise increases first and then decreases, and finally remains constant around 90 dB. Accordingly,

a suitable increase in the third-longest axis and the third-longest axis coefficients can reduce vibration noise. The reason for this may be that an increase in the third-longest axis could cause the shape of tire contact ground to become more rectangular, and this can reduce the contact pressure at the centre of the tread, and improve the uniformity of contact pressure; therefore, it is beneficial to reduce the vibration noise.

3. As the ground length and the coefficient of the second-longest axis DOF_{avg} increase, the tire vibration noise first fluctuates smoothly and then quickly increased, especially the ground length and the second-longest axis coefficients are more than 192 mm and 0.88 mm, respectively. Therefore, the ground length and the DOF_{avg} must be controlled within a reasonable range. Increasing ground length means that the contact pressure in the tread area would shift to the shoulder; if the shoulder stiffness is sufficiently large, the tread deformation will be transferred

Table 4. *Tire ground characteristic parameters in each scheme*

	$C–A$ [mm²]	L_{mid} [mm]	DOF_{avg}	LF_{avg}	F_{sr}	US_{70} [mm]	DS_{70} [mm]	AB [mm]
NEC1	47920	246.35	0.86	1.13	0.81	218	218	188.49
NEC5	48764	248.45	0.83	1.17	0.73	213.14	213.14	176.39
NEC2	48638	246.56	0.84	1.16	0.74	213.42	213.42	178.89
Belt1	48985	242.21	0.88	1.11	0.78	217.89	217.89	192.23
NEC9	48544	244.2	0.85	1.14	0.75	213.65	213.64	181.82
Belt2	48917	241.35	0.88	1.11	0.78	216.97	216.97	191.59
NEC8	48766	246.01	0.83	1.16	0.73	212	212	176.6
Belt4	48979	241.36	0.88	1.11	0.78	216.74	216.74	191.11
NEC4	47721	248.24	0.84	1.16	0.77	214.3	214.3	178.97
NEC6	48989	245.4	0.86	1.14	0.76	215.5	215.49	184.37
Belt3	48530	242.7	0.87	1.13	0.76	214.86	214.85	185.87
NEC7	48776	249.03	0.82	1.18	0.71	211.84	211.83	173.12
Belt6	48678	243.58	0.86	1.13	0.76	215.45	215.45	186.16
NEC3	47004	250.22	0.81	1.19	0.73	210.8	210.8	169.77
Belt9	48629	242.9	0.87	1.13	0.76	251.12	251.12	186.19
Belt8	49271	242.9	0.88	1.11	0.79	218.24	218.24	192.58
Belt7	49333	242.94	0.88	1.11	0.79	217.98	217.98	191.99
Belt5	49249	242.12	0.88	1.11	0.79	217.75	217.75	192.38

	CD [mm]	AD	BC	L [mm]	W [mm]	$\bar{P}$	A	$FSF_{70\%}$
NEC1	188.5	231.2	231.49	188.5	231.35	768.1	372.82	1.13
NEC5	176.39	241.82	241.79	176.39	241.81	714.47	336.3	1.1657
NEC2	178.89	241.9	241.9	178.89	241.9	718.78	322.56	1.1553
Belt1	192.23	244.75	244.75	192.23	244.75	735.23	325.9	1.1116
NEC9	181.82	242.41	242.38	181.82	242.4	722.36	314.17	1.143
Belt2	191.59	244.6	244.52	191.59	244.56	733.39	326.92	1.1124
NEC8	176.61	242.18	242.16	176.61	242.17	715.72	332.22	1.1604
Belt4	191.11	244.45	244.37	191.11	244.41	728.32	328.09	1.1136
NEC4	178.98	231.86	232.14	178.98	232	742.26	348.85	1.1584
NEC6	184.37	242.28	242.25	184.37	242.27	715.64	322.46	1.1388
Belt3	185.87	244.6	244.19	185.87	244.4	727.94	337.36	1.1296
NEC7	173.12	242.19	242.18	173.12	242.19	711.46	351.8	1.1756
Belt6	186.17	244.15	244.08	186.17	242.12	725.65	335.91	1.1306
NEC3	169.77	231.66	231.93	169.77	231.8	754.22	365.54	1.187
Belt9	186.2	243.99	243.91	186.2	243.95	722.71	344.38	0.9673
Belt8	192.59	244.35	244.27	192.59	244.31	728.16	326.73	1.113
Belt7	192	244.32	244.24	192	244.28	723.12	329	1.1145
Belt5	192.39	244.46	244.38	192.39	244.42	721.37	327.76	1.1119

to the lateral side of the sidewall, causing an increase in the sidewall vibration and noise.

4. The width of tire-ground does not have any correlation with the vibration noise.
5. With an increase in the ground shape factor $FSF_{70\%}$, the vibration noise first fluctuates smoothly and then increases to an extremely high value when the ground shape factor is nearly 0.79. When the $FSF_{70\%}$ tends to 1, the vibration noise increases; the smaller the third axis and the DOF_{avg} are, the greater the ground length and the DOF_{avg} are, and the greater the vibration noise is.
6. With the increase in the average pressure and the pressure skewness, the vibration noise first

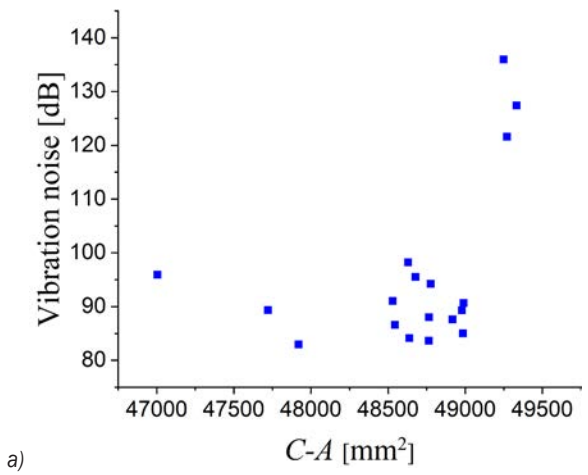

a)

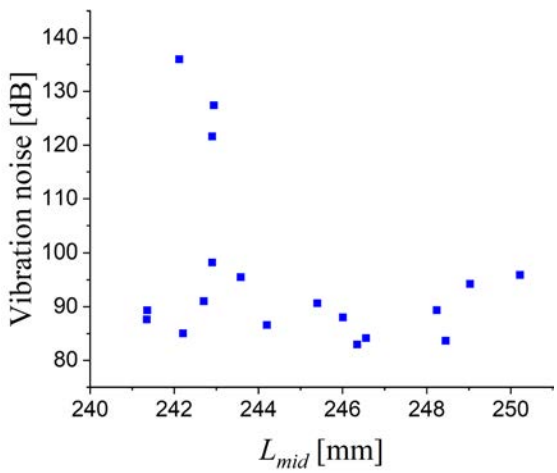

b)

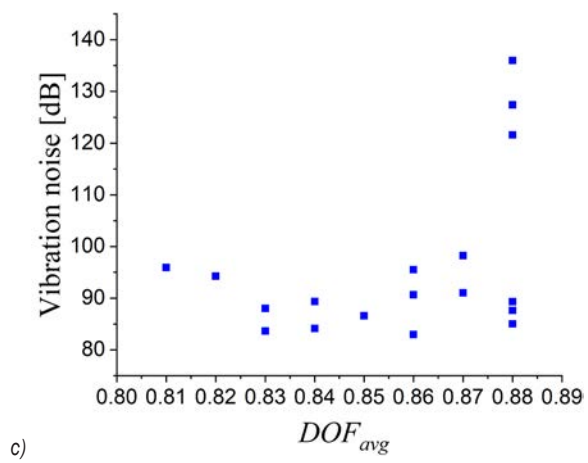

c)

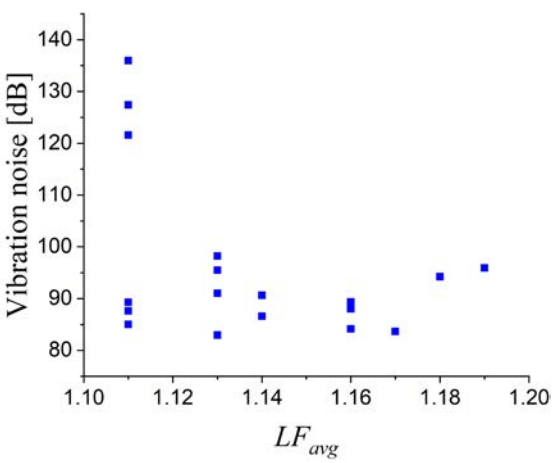

d)

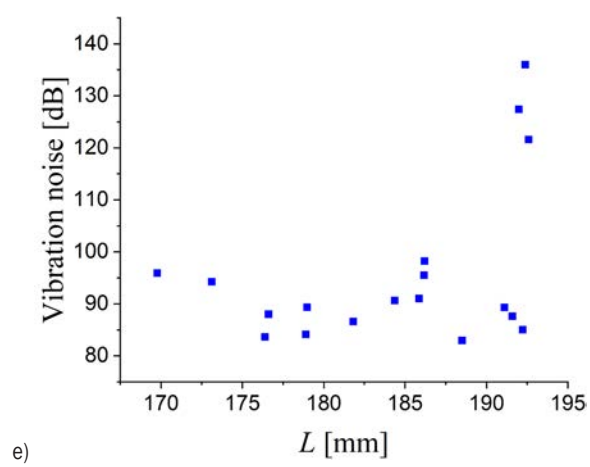

e)

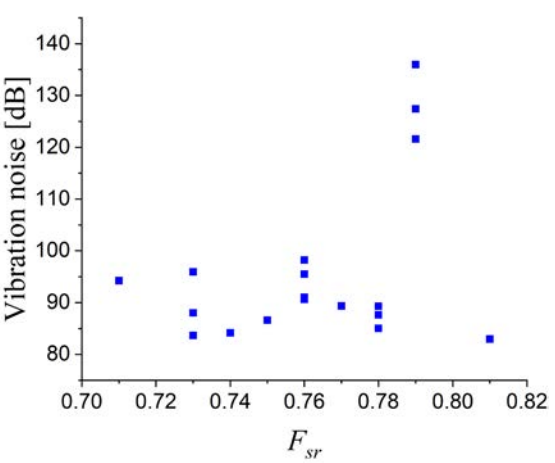

f)

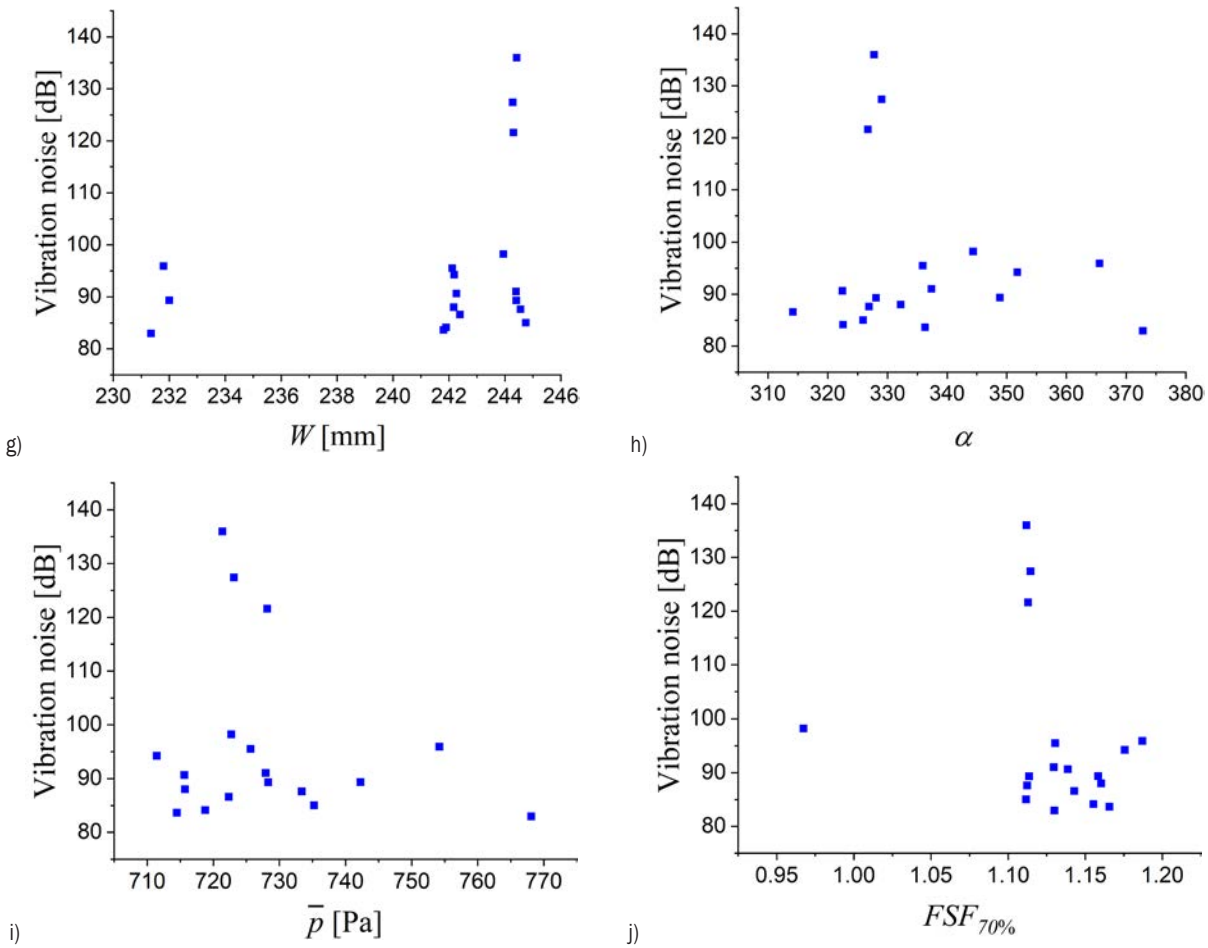

Fig. 13. *Relationship between ground parameters and vibration noise; the relationship between vibration noise and a) C-A, b) L_{mid}, c) DOF_{avg}, d) LF_{avg}, e) L, f) L_{sr}, g) W, h) α, i) $\bar{P}$, and j) $FSF_{70\%}$*

increases, then decreases, and finally tends to smooth fluctuation; this implies that the average pressure and the pressure skewness should be controlled to a certain extent.

7. The vibration noise is greatly related to the ground shape factor, except for the ground shape factor 0.97, which may be a singular point of vibration noise; the vibration noise is mainly distributed around the shape factor with a range of 1.1 to 1.2. In this range, the noise first decreases and then increases.

3.2 Relationship between Tread Deformation and Noise

3.2.1 Definition of Tread Deformation Parameters

When a tire is rolling on a road, the tread radial deformation in the ground area is the main cause of tire vibration. Different tire structure designs will lead to different radial force distribution and different radial deformation in the contact area. In this study, the tread radial deformation skewness and stiffness are selected to study the effect of radial force distribution on vibration noise.

The degree of dispersion of the tread radial deformation profile when a tire is in contact with a road is characterized by the tread radial deformation skewness, which, to a certain extent, can reflect the continuity of the tread radial deformation. The formula for the skewness of the tread radial deformation is given in Eq. (4):

$$S = \sqrt{\frac{1}{n-1}\sum_{i=1}^{n}\left(d_{zi} - \overline{d_z}\right)^2}, \tag{4}$$

where n is the number of nodes in the contact area, d_{zi} is the radial deformation of the i^{th} node, and $\overline{d_z}$ is the average of the radial deformation of all nodes in the contact area.

The radial deformation stiffness distribution of the tread is defined as shown in Eq. (5):

$$k_z = \frac{f_z}{d_z}, \tag{5}$$

where f_z is the ground pressure of the tread node in [Pa], and d_z is the radial deformation of the tread node in [m].

The ground pressure and radial deformation of the tread nodes in a contact patch are calculated from the output of Abaqus Software, and the radial deformation stiffness profile of the tire is computed in Matlab Software.

3.2.2 Effects of Tread Deformation of Contour Design on Noise

Fig. 14 shows the radial deformation distribution using the non-natural equilibrium contour design with the minimum vibration noise. It can be seen that the radial deformation of the tread at the central area is large, the deformation at the surrounding areas is small, and it rapidly reduces from the central area to the surrounding area. The largest central deformation area is not continuous, which is caused by the longitudinal grooves; therefore, it leads to stress concentration phenomenon in the contact width y-direction. The maximum deformation in the contact area is 38.562 mm, and the minimum deformation in the edges is 8.19 mm in the contact length x-direction.

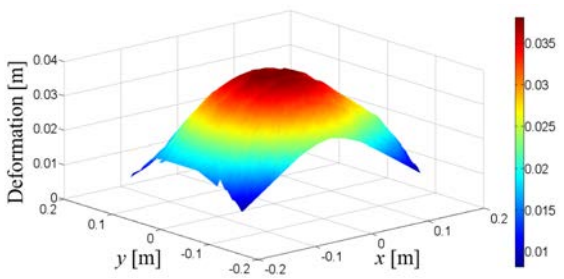

Fig. 14. *Tire radial deformation distribution in the noise minimization using contour design*

To further obtain ground parameters, the contact area is divided into five subareas: C_A for the ground front, C_B for the ground centre area, C_C for the ground back, and C_D and C_E for the tread on both sides of the tire shoulder area, as shown in Fig. 15. The deformation stiffness in the five subareas is the average deformation stiffnesses of the tread nodes, which is calculated using Eq. (6).

$$K_{(C_A,C_B,...,C_E)} = \frac{\sum_{i=1}^{n} k_{zi}}{n}. \tag{6}$$

Many studies [1] and [2] have shown that the vibration noise produced by the front and rear of a tire coming into contact with the ground is asymmetrical. Therefore, the above five subareas must be studied separately. In order to determine the principle of subareas division, the skewness of tread deformation is studied by changing the size of the five subareas. When the skewness of the each of subareas reaches a relative minimum, the subareas profile are fixed for partitioning the areas.

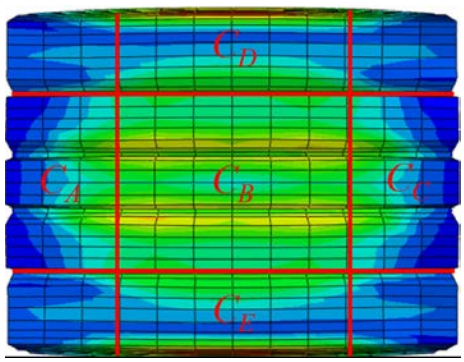

Fig. 15. *Tire contact area division*

Table 5. *Tire radial deformation in the noise minimization design and original design*

Minimum noise	Tread radial deformation skewness $\times 10^{-3}$					Noise [dB]
	C_A	C_B	C_C	C_D	C_E	
Structure design	5.3655	3.3903	5.3655	2.6793	2.6786	81.73
Original design	5.4327	3.4428	5.4327	2.7678	2.7680	91.77

The skewness of the tread radial deformation of the five subareas shown in Fig. 15 is studied and compared with the skewness of the tread radial deformation under the noise minimization contour design and the original structural design. The comparable results are listed in Table 5. As shown in the table, the skewness of the tread radial deformation of the two tires at the front and rear ends (C_A and C_C) and both sides of the tread (C_D and C_E) are similar and symmetrical. It is also observed that the skewness of the tread radial deformation at C_A, C_B, C_C, C_D, and C_E of the tire with the original design is larger than that of the noise minimization contour design.

Fig. 16 shows the radial deformation stiffness of the noise minimization contour design and original design. It can be seen that the subarea C_B of the two

tires is relatively high, and that of the C_A and C_C regions are relatively low. Stress concentrates near the shoulder because of the stirrup effect of the belt layer. The concave part in Fig. 16 is caused by the discontinuity of the longitudinal grooves.

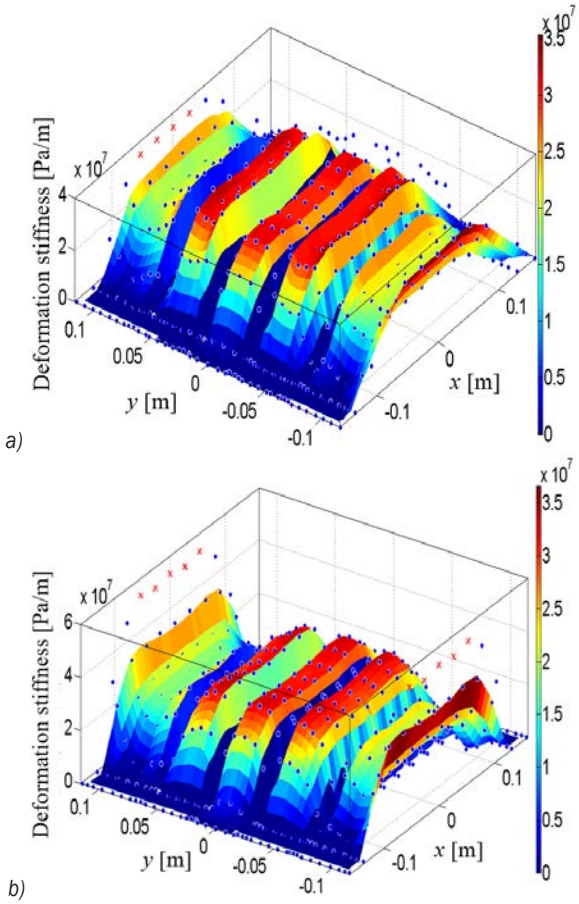

Fig. 16. *Tire radial deformation stiffness in noise minimization using a) contour design; and b) original design*

The average values of the radial deformation stiffness of the five subareas in the noise minimization design and original design are listed in Table 6, in which it can be seen that the tread radial deformation stiffness is the largest on both sides of the tread near the shoulder (C_D and C_E), followed by the tread centre area (C_B). The radial deformation stiffness of the tread at C_A and C_C is the smallest. The radial deformation stiffnesses of the treads near the shoulder (C_D and C_E) are similar to each other, and so are the radial deformation stiffnesses at the front and rear (C_A and C_C); the distribution is symmetrical. By comparing the two tires, it is found that the tread radial deformation stiffness values at C_B, C_D, and C_E are larger in the noise minimization design, whereas the radial deformation stiffness values of the tread at C_A and C_C in both designs are similar with small differences.

Table 6. *Average values of tire radial deformation stiffness in noise minimization design and original design*

Minimum noise	Deformation stiffness [$\times 10^6$ Pa/m]					Noise [dB]
	C_A	C_B	C_C	C_D	C_E	
Structure design	5.8518	15.8462	5.8516	32.5315	32.5357	81.73
Original design	5.6066	14.7364	5.6068	28.3505	28.3522	91.77

3.2.3 Effects of Tread Deformation of Belt Design on Noise

Fig. 17 shows the radial deformation of the tread used in the noise minimization using belt design. As seen in the figure, the radial deformation of the tread at the central area is large, and the deformation in the surrounding areas is small, and it is radially reduced from the central area to surrounding area. Continuous deformation is not observed in the central area, which is caused by the longitudinal grooves. The maximum deformation in the contact area is 37.607 mm, and the minimum deformation in the edges is 8.111 mm.

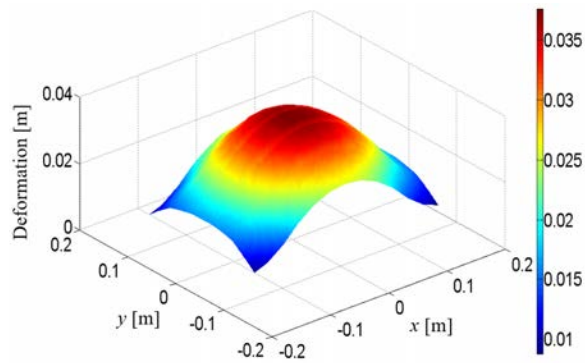

Fig. 17. *Tire radial deformation distribution in noise minimization using belt design*

The skewness of the tread radial deformation in the noise minimization belt design and original design is listed shown in Table 7. As seen in the table, the skewness values of the tread radial deformation of the two tires at the front and rear ends (C_A and C_C) are similar to each other and symmetrical, as are the skewness values on both sides of the tread (C_D and C_E). By comparing and analysing the skewness of the tread radial deformation of the two tires, it is found that the skewness values of the tread radial deformation at C_A, C_B, C_C, C_D, and C_E in the original design are larger than that of the noise minimization belt structure design.

Table 7. *Standard deviation of tire radial deformation in noise minimization design and original design*

Minimum noise	Tread radial deformation skewness $\times 10^{-3}$					Noise [dB]
	C_A	C_B	C_C	C_D	C_E	
Structure design	5.2338	3.3412	5.2338	2.6755	2.6755	84.22
Original design	5.4327	3.4428	5.4327	2.7678	2.7680	91.77

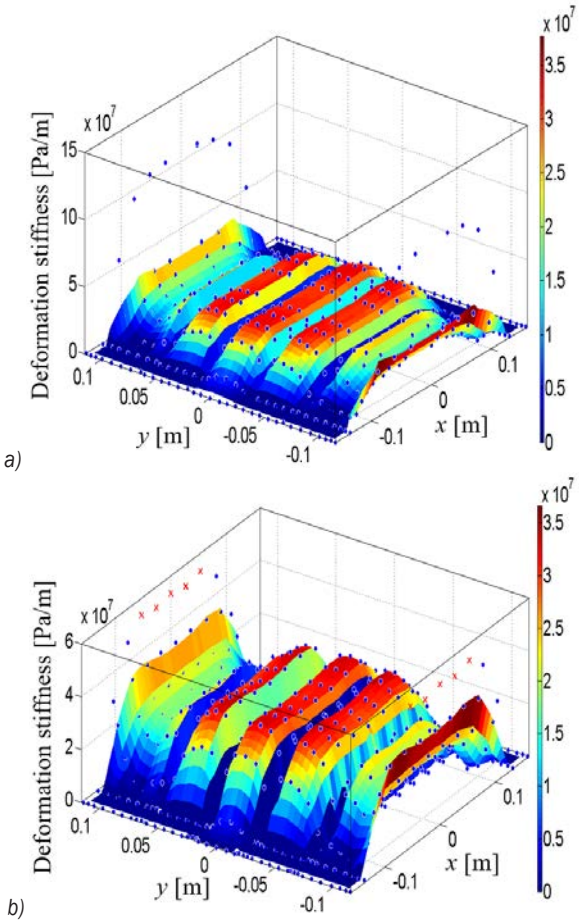

Fig. 18. *Tire radial deformation stiffness in noise minimization: a) using belt design; and b) original design*

The results of a comparative analysis of the radial deformation stiffness of the noise minimization belt structure design and the original design are shown in Fig. 18. As shown in the figure, the radial deformation stiffness of the tread at the center (C_B) in the two tires is relatively high, whereas that at C_A and C_C is relatively low. The concave part of the Fig 18 is caused by the longitudinal grooves of the tire.

The average values of tire radial deformation stiffness of five subareas in the noise minimization belt structure design and original design are listed in Table 8. As listed in Table 8, the tread radial deformation stiffness is the largest on both sides of the tread (C_D and C_E), followed by the tread centre area (C_B). The radial deformation stiffness of the tread at C_A and C_C is the smallest. The radial deformation stiffness of the tread near the shoulder (C_D and C_E) are similar, as are the radial deformation stiffness at the front and rear (C_A and C_C); the distribution is symmetrical. By comparing the two tires, it is found that the tread radial deformation stiffness at C_A, C_B, C_C, C_D, and C_E are higher in the noise minimization belt structure design.

3.3 Relationship between Tire Radial Excitation Force and Noise

In the signal spectrum analysis, the power spectral density is not only reflecting the signal energy change in frequency range but also reflects the vibration energy [28]. Therefore, the causes of minimum tire vibration noise reduction can be analysed from the power spectral density of the tire radial force excitation.

Fig. 19 shows the tire excitation power spectral density of the noise minimization design using the new non-natural equilibrium contour design and that of the original design. It can be seen that the peak value and number of the power spectral density in the noise minimization are less compared with the original design, especially in 50 Hz to 130 Hz, 220 Hz to 340 Hz, and 440 Hz to 500 Hz frequency ranges. At the same time, considering the noise spectrum characteristics showed in Fig.10, it can been that, the spectral density is low at the sensitive frequencies of 440 Hz and 488 Hz, and the reduction in tire vibration noise is due to the reduction in the energy of tire radial excitation force.

Fig. 20 shows the tire excitation power spectral density the noise minimization design using the belt

Table 8. *Average values of tire radial deformation stiffness in the noise minimization design and original design*

Minimum noise	Deformation stiffness $\times 10^6$					Noise [dB]
	C_A	C_B	C_C	C_D	C_E	
Structure design	8.6286	22.1175	8.3738	37.3629	37.3629	81.73
Original design	5.6066	14.7364	5.6068	28.3505	28.3522	91.77

design and that of the original design. As shown in the figure, the peak value of the exciting power spectrum density of the noise minimization design using the belt optimization reduces remarkably. Combining the sound pressure frequency-response function of Fig. 10, it shows that the belt optimization design could result in a minimum excitation power spectral density compared with the original design, and the impacts of the 220 Hz to 260 Hz and 380 Hz to 450 Hz frequency ranges of the power spectrum are significantly reduced. In particular, at the sensitive frequency of 440 Hz, the power density of the tire radial force excitation decreases.

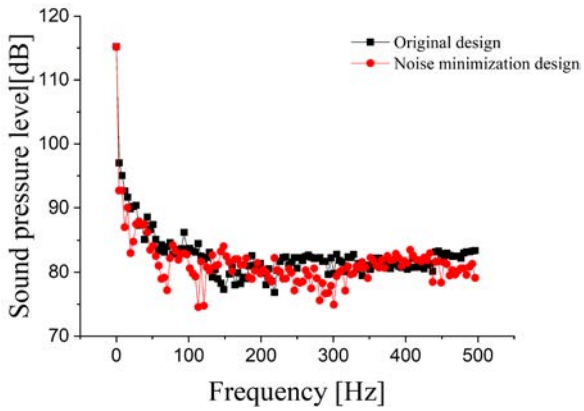

Fig. 19. *Comparison of power spectral density in the noise minimization contour design and original design*

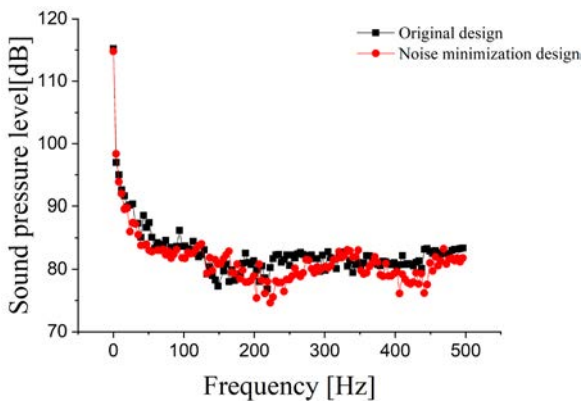

Fig. 20. *Comparison of power spectral density in the noise minimization belt design and original design*

4 CONCLUSIONS

1. Numerical simulations are conducted to establish a tire model and analyse tire vibration noise. The results of the tire modal and noise of different tire structures designed using the orthogonal experimental design method showed that the structural design of a tire had only a slight impact on the tire's natural frequency but a considerable impact on vibration noise.
2. This study introduced a series of geometric and mechanical parameters to describe the tire ground characteristics, and the relationship between ground characteristics and vibration noise is established. Reduction in the coefficient of the third-longest axis LF_{avg} and increase in the coefficient of the second-longest axis DOF_{avg} would enhance tire vibration noise; there is no significant relationship between contact width W and tire vibration noise; the value of the shape coefficient of the tire-ground F_{sr} being close to 1 means the large tire vibration noise.
3. The tire contact patch is divided into five subareas, and the skewness and stiffness of the radial deformation of the tread at these five subareas are analysed; the results showed that the skewness had a positive correlation with tire vibration noise (i.e., the smaller the skewness of the tread radial deformation is, the lower the vibration noise is). The radial deformation stiffness of the tread had a negative correlation with the tire vibration noise (i.e., tire vibration noise increased as the tread deformation stiffness decreased).
4. The power spectral density is selected to describe the impact force response of the rolling tire in contact with the road. A comparison between the power spectral density of the noise minimization design and that of the original design, the results showed that the peak value and quantity of power spectral density of the noise minimum structure design decreased significantly, especially at the sensitive frequencies of 440 Hz and 488 Hz. It infers that a decreasing tire radial impact reduces the tire vibration noise.

5 ACKNOWLEDGEMENTS

This work is supported by the National Natural Science Foundation of China under Grant 52072156 and 51675240.

6 REFERENCES

[1] Sandberg, U., Ejsmont, J.A. (2002). *Tyre/Road Noise Reference Book*. INFORMEX, Kisa.

[2] Li, T. (2018). Literature review of tire-pavement interaction noise and reduction approaches. *Journal of Vibroengineering*, vol. 20, no. 6, p. 2424-2452, **DOI:10.21595/jve.2018.19935**.

[3] Diaz, C.G., Kindt, P., Middelberg, J., Vercammen, S., Thiry, C., Close, R., Leyssens, J. (2016). Dynamic behaviour of a

rolling tyre: Experimental and numerical analyses. *Journal of Sound and Vibration*, vol. 364, p. 147-164, **DOI:10.1016/j.jsv.2015.11.025**.

[4] Del Pizzo, A., Teti, L., Moro, A., Bianco, F., Fredianelli, L., Licitra, G. (2020). Influence of texture on tyre road noise spectra in rubberized pavements. *Applied Acoustics*, vol. 159, p. 1-12, **DOI:10.1016/j.apacoust.2019.107080**.

[5] Keltie, R.F. (1982). Analytical model of the truck tire vibration sound mechanism. *The Journal of the Acoustical Society of America*, vol. 71, no. 2, p. 359-367, **DOI:10.1121/1.387460**.

[6] Belgacem, W., Berry, A., Masson, P. (2012). Active vibration control on a quarter-car forconcellation of road noise distribution. *Journal of Sound and Vibration*, vol. 331, no. 14, p. 3240-3254, **DOI:10.1016/j.jsv.2012.02.030**.

[7] Dubois, G., Cesbron, J., Yin, H.P., Anfosso-Lédée, F., Duhamel, D. (2013). Statistical estimation of low frequency tyre/road noise from numerical contact forces. *Applied Acoustics*, vol. 74, no. 9, p. 1085-1093, **DOI:10.1016/j.apacoust.2013.03.011**.

[8] Zhou, H., Wang, G., Zhang, Y., Yang, J., Zheng, Z. (2017). Study of the influence of tire belt structure on vibration noise. *Recent Patents on Mechanical Engineering*, vol. 10, no. 4, p. 270-278, **DOI:10.2174/2212797610666170817095107**.

[9] Wang, G.L., Pei, X.P., Zhou, H.C., Zhao, F., Yang, J. (2015). Acoustic contribution of tire structure vibration and method for noise reduction. *Journal of Vibration and Shock*, no. 24, p. 53-58, **DOI:10.13465/j.cnki.jvs.2015.24.009**. (in Chinese)

[10] Zhang, Z., Fu, H., Liang, X., Chen, X., Tan, D. (2020). Comparative analysis of static and dynamic performance of nonpneumatic tire with flexible spoke structure. *Strojniški vestnik - Journal of Mechanical Engineering*, vol. 66, no. 6-7, p. 458-466, **DOI:10.5545/sv-jme.2020.6676**.

[11] Wang, G.L., Qian, H., Zhou, H.C., Qiao, L., Liu, C.Z. (2019). Relationship between the tire hydroplaning speed and noise performance based on grounding characteristics. *Journal of Jilin University (Engineering and Technology Edition)*, vol. 49, no. 1, p. 14-23, D**OI:10.13229/j.cnki.jdxbgxb20171057**. (in Chinese)

[12] Li, T. (2018). Influencing parameters on tire–pavement interaction noise: Review, experiments, and design considerations. *Designs*, vol. 2, no. 4, p. 1-38, **DOI:10.3390/designs2040038**.

[13] Du, X., Zhao, Y., Wang, Q., Fu, H., Lin, F. (2019). Grounding characteristics of a non-pneumatic mechanical elastic tire in a rolling state with a camber angle. *Strojniški vestnik - Journal of Mechanical Engineering*, vol. 65, no. 5, p. 287-296, **DOI:10.5545/sv-jme.2018.5845**.

[14] Wang, G.L., Zhang, P., Zhou, H.C., Yang, J., Zheng, Z., Ren, X.J. (2017). Effect of tread deformation and stiffness on road holding performance. *Journal of Mechanical Engineering*, vol. 53, no, 10, p. 108-115, **DOI:10.3901/JME.2017.10.108**. (in Chinese)

[15] Liang, C., Zhao, F., Wang, G.L., Yang, J., Zhou, H.C., Wang, Z.J. (2015). Tire vibration noise study of radial truck tire based on a new non-natural equilibrium design. *Journal of Vibration Engineering*, vol. 28, no. 5, p. 800-808, **DOI:10.16385/j.cnki.issn.1004-4523.2015.05.016**.

[16] Hubbell, D.R. Jr. (2001). EP0944484B1. *Method for Characterizing Noise Level of Rotating Tire*. European Patent Office, Munich.

[17] Cesbron, J., Anfosso-Lédé, F., Duhamel, D., Yin, H. P., Le Houédec, D. (2009). Experimental study of tyre/road contact forces in rolling conditions for noise prediction. *Journal of Sound and Vibration*, vol. 320, no. 1-2, p. 125-144, **DOI:10.1016/j.jsv.2008.07.018**.

[18] Cohn, A. (2015). Commercial trailer tires: Tire inflation and its effect on rolling resistance, fuel economy, and tire footprint. *Tire Science and Technology*, vol. 43, no. 2, p. 144-162, **DOI:10.2346/tire.15.430201**.

[19] Zhou, H., Wang, G., Ding, Y., Yang, J., Liang, C., Fu, J. (2015). Effect of friction model and tire maneuvering on tire-pavement contact stress. *Advances in Materials Science & Engineering*, vol. 2015, p. 1-11, **DOI:10.1155/2015/632647**.

[20] Wei, Y., Feng, X., Fuqiang, Z., Xiang, D. (2016). Simulation of rolling noise based on the mixed Lagrangian-Eulerian method. *Tire Science and Technology*, vol. 44, no. 1, p. 36-50, **DOI:10.2346/tire.16.440103**.

[21] Citarella, R., Federico, L., Cicatiello, A. (2007). Modal acoustic transfer vector approach in a FEM-BEM vibro-acoustic analysis. *Engineering Analysis with Boundary Elements*, vol. 31, no. 3, p. 248-258, **DOI:10.1016/j.enganabound.2006.09.004**.

[22] Iwao, K., Yamazaki, I. (1996). A study on the mechanism of tire/road noise. *JSAE Review*, vol. 17, no. 2, p. 139-144, **DOI:10.1016/0389-4304(95)00004-6**.

[23] Liu, Z.C., Ming, L., Li, J., Fang, Y., Dong, M.H. (2011). Effect of belt structure on footprint,radial stiffness and noise of PCR tire. *Tire Industry*, vol. 31, no. 9, p. 534-536, **DOI:10.3969/j.issn.1006-8171.2011.09.004**.

[24] Sakai, E.H. (1995). Measurement and visualization of the contact pressure distribution of rubber disks and tires. *Tire Science and Technology*, vol. 23, p. 238-255, **DOI:10.2346/1.2137506**.

[25] Yang, J., Wang, G.L., Wang, Z.J. (2015). A study on the new Non-natural equilibrium contour design of vehicle tires with conflicting performance compatibility. *Automotive Engineering*, vol. 37, no. 12, p. 1418-1425, **DOI:10.3969/j.issn.1000-680X.2015.12.011**. (in Chinese)

[26] Wang, Y.Q., Huo, X.W. (2018). Multi-objective optimization design and performance prediction of centrifugal pump based on orthogonal test. *Advances in Materials Science and Engineering*, vol. 2018, p. 1-10, **DOI:10.1155/2018/6218178**.

[27] Wang, G.L., Qiao, L., Zhou, H.C., Qiao, H., Liu, C.Z. (2019). Influence of PCR tire grounding characteristics to noise and rolling resistance. *Journal of Mechanical Engineering*, vol. 55, no. 16, p. 123-131, **DOI:10.3901/JME.2019.16.123**. (in Chinese)

[28] Múčka, P., Stein, G.J., Tobolka, P. (2020). Whole-body vibration and vertical road profile displacement power spectral density. *Vehicle System Dynamics*, vol. 58, no. 4, p. 630-656, **DOI:10.1080/00423114.2019.1595675**.

Strojniški vestnik - Journal of Mechanical Engineering 67(2021)1-2, 27-35

DOI:10.5545/sv-jme.2020.6953 Original Scientific Paper
Received for review: 2020-09-25
Received revised form: 2020-12-10
Accepted for publication: 2021-01-27

Evaluation of Mechanical, Microstructures and Wear Behaviours of Aluminium Alloy Reinforced with Mussel Shell Powder for Automobile Applications

Idawu Yakubu Suleiman[1] – Auwal Kasim[2] – Abdullahi Tanko Mohammed[3] – Munir Zubairu Sirajo[4]

[1]University of Nigeria, Department of Metallurgical and Materials Engineering, Nigeria
[2]Ahmadu Bello University, Department of Metallurgical and Materials Engineering, Nigeria
[3]Waziri Umaru Federal Polytechnic, Department of Mechanical Engineering, Nigeria
[4]Petroleum Technology Development Fund, Abuja, Nigeria

This paper aims to investigate the mechanical (tensile, hardness, impact, elongation), microstructure and wear behaviours of aluminium alloy reinforced with mussel shell powder (MSP) at different weight percentages (0 wt. % to 15 wt. %) at 3 wt. % interval. The mussel shell powder was characterized by X-ray fluorescence (XRF). The matrix and the composites' morphology were studied using a scanning electron microscope attached with energy dispersive spectroscopy for the distribution of mussel shell powder particles within the matrix. The wear behaviour of the alloy and composites produced at various reinforcements were carried out using a Taber abrasion wear-testing machine. The XRF showed the compositions of MSP to contain calcium oxide (95.70 %), silica (0.83 %) and others. Mechanical properties showed that tensile values increase with increases in MSP, hardness value increases from 6 wt. % to 15 wt. % of MSP. The impact energy decreased from 42.6 J at 3 wt. % to 22.6 J at 15 wt. %; the percentage elongation also decreased from 37.4 % at 3 wt. % to 20.5 % at 15 wt. % MSP, respectively. The bending stress results increase with increases in the percentage of reinforcement. The morphologies revealed that uniform distribution of MSP within the matrix resulted to improvement in mechanical properties. The wear resistance of the composites increases with increase in the applied load and decreases with increases in the weight percentage of MSP and can be used in the production of brake pads and insulators in the automobile industry.

Keyword: aluminium alloy, composites, mussel shell powder, mechanical properties, microstructures, wear behaviour

Highlights

- *The use of aquaculture (mussel) shell waste material as reinforcement in aluminium metal composites has proved to be a cost-effective, environmentally friendly and good substitute to imported synthetic reinforcements, which can be utilized in the automobile industry.*
- *The XRF analysis of mussel shell powder contains ceramic materials, such as calcium oxide (CaO), silica (SiO_2), iron oxide (Fe_2O_3), magnesium oxide (MgO), aluminium oxide (Al_2O_3), and strontium (SrO), which were uniformly distributed within the composites and contributed immensely to the properties investigated.*
- *The wear rate was significantly lower in the aluminium metal composites produced, and varies with normal load, and the cumulative volume loss increases with increasing applied normal load. The reinforcement of mussel shell powder particles in the Al-Si-Mg alloy matrix decreased the wear resistance of the composites produced.*
- *The mechanical results obtained showed that the composite produced can be tailored toward achieving the desired or unique properties for particular applications in the automobile or aerospace industries.*

0 INTRODUCTION

The growth of world's population and increase of living standard due to technological development have increased the quantity of waste materials generated through industrial, mining and agricultural activities substantially. The waste materials are becoming major concern to both environmentalists and human beings globally [1]. Utilization of waste materials could reduce contamination and free up spaces for disposal or recycling of waste materials by converting it into useful material for applications in aerospace and automobile/construction industries could save the world from natural disasters as being observed [2].

Aluminium matrix composites (AMCs) are presently produced by employing several conventional and patented methods. The properties of AMCs are governed by the processing method. A liquid route, such as casting, is relatively simple and economical, but the limited wettability of reinforcement in molten aluminium limits its usage. The economy, simplicity and ability to produce large and intricate parts are the key parameters that make stir casting the most preferred method for producing AMCs. The limitation of stir casting is the wettability between the molten aluminium matrix and the ceramic particle. AMCs produced through conventional casting offer difficulties in the even mixing of the reinforcement in main matrix [2]. The difference in densities of the

*Corr. Author's Address: University of Nigeria, Department of Metallurgical and Materials Engineering, Nsukka, Enugu City, Nigeria, idawu.suleiman@unn.edu.ng

base matrix and reinforcement hinders the distribution of reinforcement in the main matrix and promotes the formation of agglomerates or clusters. This can be avoided by employing a stirrer in the molten mixture so that the difference in energies may be checked. The stirring of the molten mixture before pouring into the mould cavity promotes the uniform distribution of reinforcement in the aluminium matrix, induces vortex formation, and the reinforced particles are mixed at the side of the vortex [3].

The reinforced materials with ashes or powders had produced materials that are quite friendly with environmental and cost-effective benefits [3]. Aluminium-based Metal Matrix Composites (MMCs) have received increasing attention in recent decades as engineering materials, and the introduction of ceramic material into a metal matrix produces a composite material that resulted in an attractive combination of physical, chemical, and mechanical properties that cannot be obtained with the aluminium alloys alone [4].

Different reinforcements such as aluminium oxide (Al_2O_3), silicon carbide (SiC), titanium carbide (TiC), tungsten (W), calcium oxide (CaO), silica (SiO_2) etc have been used to enhance aluminium composite properties. Studies had also shown that hardness, toughness, tensile and wear rate behaviours were enhanced [5]. These unnatural reinforcers frequently used were difficult to obtain in Nigeria and the importation of such materials are at high cost and time constraint, which may impede the production of the composites. An alternative to these reinforcements in developing countries is to explore agricultural and aquaculture wastes, either in the form of ashes or powder. The wastes of bagasse [6], melon shell ash studied [7], periwinkle shell powder was used [8], and oyster shells, among others, for the development of AMCs had been investigated [9]. The results had also shown that waste ashes and powder generated contain high percentages of refractory materials, such as alumina (Al_2O_3), silica (SiO_2), hematite (Fe_2O_3), carbonate ($CaCO_3$) and calcium (Ca), among others, which can be explored for the production of composite

Mussel shell is an aquaculture waste generated across the southern part of Nigeria and poses a serious threat to both the environment and human lives. In order to relieve this region of this threat, the mussel shells were collected, subjected to treatments, and convert to powder under strict conditions. From the above aforementioned, the present paper, therefore, investigates the use of aquaculture- mussel shell powder (MSP) of particle size 100 µm by dispersing it into an alloy via liquid metallurgy to obtain composite. Mussel powder was varied from 0 wt. % to 15 wt. % at 3 wt. % interval. The chemical analysis of mussel powder was also carried out, mechanical, microstructure and the wear rate of the matrix and composites were carried out simultaneously.

1 EXPERIMENTAL

1.1 Material Preparation

Mussel shell powder was prepared by cleaning, washing, drying, grinding and sieving it to obtain a uniform size. The sieving was done at the Department of Agriculture and Bio-resources Engineering, University of Nigeria, Nsukka with an electric-powered sieving machine. A sieve of 100 µm was used to sieve the mussel powder to uniform sizes. Fig. 1a show the mussel shell collection while fig. 1b also showed the MSP of particle size 100 µm produced respectively. The chemical compositions of the MSP are presented in Table 1.

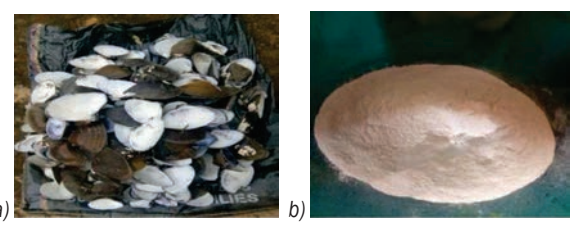
a) b)

Fig. 1. *a) Mussel shell collections, and b) mussel shell of particle size of 100 µm*

Table 1. *The mussel powder analysis*

Compounds	Mussel shell powder [%]
CaO	95.70
K_2O	0.35
SiO_2	0.83
SrO	0.26
Fe_2O_3	0.67
SO_3	0.46
MgO	0.48
Al_2O_3	0.46

1.2 Production of Al-Mg-Si/Mussel shell powder particulate composites

The present study utilized aluminium alloy and mussel shell powder with a particle size of 100 µm as base matrix and reinforcement, respectively. The chemical composition of the alloy is presented in Table 2. The amounts of mussel shell powder (MSP) used as reinforcers were determined using charge

calculations presented in Table 3. The aluminium alloy was superheated to 800 °C after being charged into a crucible furnace. The stainless-steel stirrer was used to stir the molten alloy/composites manually. The reinforcement particles, MSP, were preheated to 200 °C for 30 minutes. After preheating, MSP particles were consolidated into the melt to exclude moisture. To reduce the porosity, the addition of the degassing tablet was added after the alloy/composites were completely melted. The wettability was enriched by the composition of magnesium in the melt. This magnesium improves the wettability between the matrix alloy, reinforcement thus, 3 wt. % to 15 wt. % at 3 wt. % interval by equal MSP proportions used. Preheated moulds were set before casting the alloy and the composite of 30 mm by 100 mm, respectively. Chemical analyses were performed on the alloy and the composite. Fig. 2 shows the preparation, equipment and cast products (alloy/composite) for this research.

Table 2. *Al-Mg-Si alloy analysis*

Compositions	Mg	Si	Fe	Mn	Cr	Cu	Al
Weight percent [wt. %]	1.0	.60	.01	.02	.01	.03	Bal.

Table 3. *Summary of charge calculations in weight percent [wt. %]*

S/No.	0 wt.% MSP	3 wt.% MSP	6 wt.% MSP	9 wt.% MSP	12 wt.% MSP	15 wt.% MSP
[MSP]	0	3	6	9	12	15
Silicon (Si)	0.600	0.600	0.600	0.600	0.600	0.600
Magnesium	1.000	1.000	1.000	1.000	1.000	1.000
Aluminium	98.400	95.400	92.400	89.400	86.400	83.400
Total	100	100	100	100	100	100

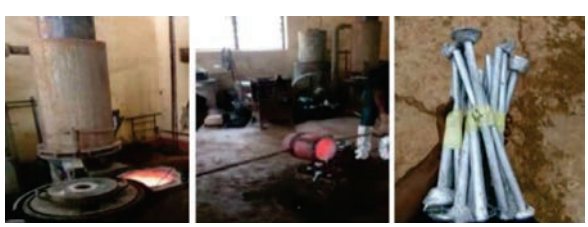

Fig. 2. *The casting to the finished products*

1.3 The Alloy and Composites Tensile Strength

A universal tensile testing machine was used to evaluate the tensile properties of the alloy/composites produced. The test specimen preparation and testing procedure were in accordance with ASTM E8/E8M-15a **[10]** and shown in Fig. 3.

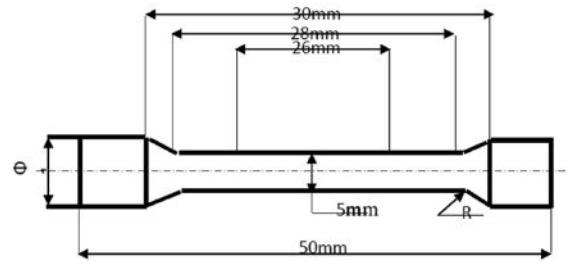

Fig. 3. *Dimensions of tensile test specimen*

1.4 Hardness Values

The sample preparation and testing procedure was performed in accordance with ASTM E18-16 **[11]**. The hardness values within the range of 2 % were averaged to obtain the hardness value for the alloy and composites.

1.5 Impact Toughness

The impact specimen was placed on a horizontal stand of the Izod Impact Machine. It was arranged such that the notch was directly opposite to the point of impact of a heavily suspended mass. With the gauge set properly, the suspended mass was released from a height to hit the specimen. The energy absorbed by the specimen was reflected on a calibrated scale as reported by **[12]**, and **[13]**. The results obtained were thus analysed.

1.6 Microstructure of the Alloy/Composite

Analysis of the microstructures of the alloy/composite was carried out using model JEOL 840 of scanning electron microscope attached with energy dispersive spectroscopy (SEM/EDS) after cutting, grinding, and polishing the specimens with different grades of papers in accordance with **[14]** and **[15]**. Etching was carried by wiping the specimen surface with wool soaked in natal to give a dull reflection surface **[16]**.

1.7 Wear Test

The wear behaviour of the test samples (alloy and composites) was determined using the pin-on-disc test under dry conditions as stated for wear testing in **[17]**. It was carried out with the use of a Taber abrasion wear-testing machine. The wear test samples were produced in the form of a disc and machined to specifications (200 mm diameter and 5 mm thickness). 10 N and 20 N loads were used, and the wear loss was evaluated according to **[18]**.

2 RESULTS

2.1 Mussel Powder Compositions

The results revealed by the elemental analysis mussel shell powder from X-Ray Fluorescence (XRF) are presented in Table 1 and the powder particle size of 100 μm. From the table, the mussel shell powder contains calcium oxide content of 95.70 %, alumina of 0.46 %, silica of 0.83 %, magnesium oxide of 0.48 %, aluminium oxide of 0.46 %, iron oxide of 0.67 % and the remaining balance was lost on ignition (LOI) respectively.

2.2 Microstructures

The morphologies of the alloy and EDS are presented in Fig. 4, while the composites at various weight percent of the reinforcements from 0 wt. % to 15 wt. % of MSP was presented in Fig. 5.

2.3 Mechanical Properties

The results of the mechanical properties investigated such as hardness, tensile, impact toughness and percentage of elongation are also presented in Fig. 6 and Table 5, respectively.

2.4 The Wear of the Alloy/Composites

Figs. 7 and 8 presented the effect of reinforcement on specific wear rate and the morphologies of wear rate before and after the tests.

3 DISCUSSION

3.1 Microstructure

The performance of alloys or composite can be known through their microstructures. The alloys/reinforcement with mussel powder examined were at 2000× magnification. The micrograph presented in Fig. 4 represents the aluminium alloy and its energy dispersive spectroscopy while Fig. 5 shows the composites produced with different percentage of MSP at 3 wt. %, 6 wt. %, 9 wt. %, 12 wt. % and 15 wt. %. From the figures, the calcium oxides (CaO) distributed within the structures reveal fairly uniform distributions of MSP in the produced composite. There appears to be a reasonably uniform distribution of MSP in the alloy, which can be as a result of good interfacial bonding, decreases in particle size and increases in specific surface of the reinforcement for a given volume fraction [19]. The volume of CaO and SiO in MSP is shown in black while the white showed the matrix and conformed to the findings of [20].

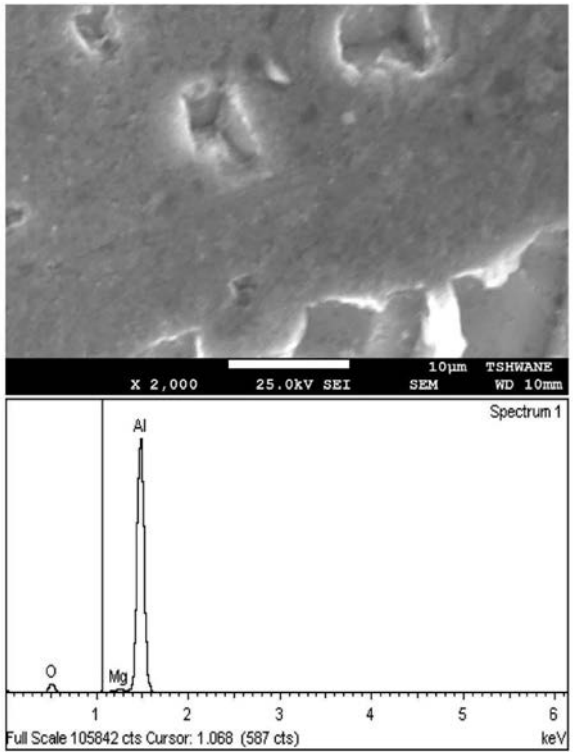

Fig. 4. *SEM/EDS of aluminium alloy without reinforcement*

Table 4. *The EDS of the elements in Al-Mg-Si alloy*

Element	Weight %
O K	0.03
Cu K	0.01
Mg K	1.00
Al K	Balance
Si K	0.58
Cl K	0.02
Fe K	0.01
Ni K	0.04
Mn K	0.03
Totals	100.00

3.2 Mechanical Properties of Alloy/Composites

3.2.1 Hardness Values

The hardness, tensile strength, impact toughness and percentage elongation of the alloy and the composites were presented in Fig. 6 and Table 5. The hardness value of the alloy was 49.78 HRC decreased to 13.16 HRC at 6 wt. % of MSP and later increased to 53.52

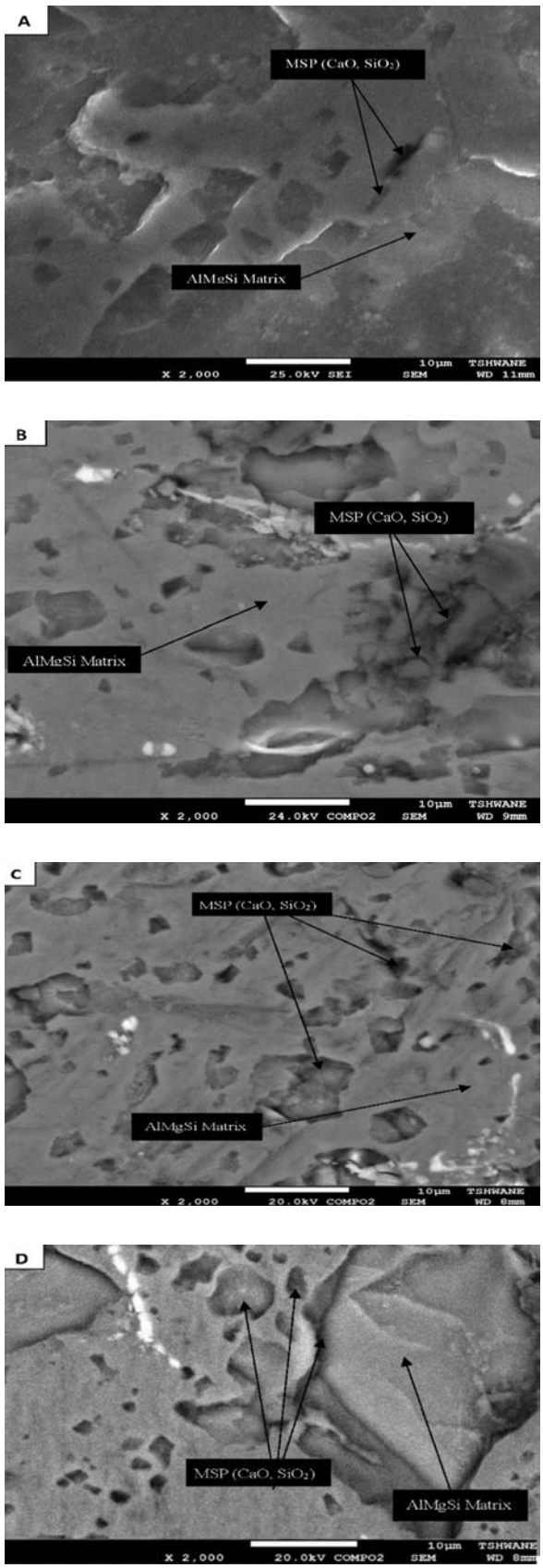

Fig. 5. *SEM morphologies of aluminium alloy/composites at: a) 3 wt. % MSP, b) 6 wt. % MSP, c) 9 wt. % MSP, d) 12 wt. % MSP, and e) 15 wt. % wt. % MSP*

HRC at 15 wt. % MSP. That is a decrease of 73.56 % of the alloy to the composite at 6 wt. %, and an increase of 75.41 % at 15 wt. % of MSP was recorded. Previous works attributed this increase in hardness to the decreased particle size and increased specific surface of the reinforcement for a given volume fraction [21]. The hardness values were improved at higher wt. % of MSP loading. The improvement of the hardness of the composites to the increased particle volume fraction, and increased strain energy at the periphery of particles dispersed in the matrix confirmed the previous studies [22] and [23].

3.2.2 Tensile Strength

The alloy/composite with mussel powder results is shown in Fig. 6. The addition of mussel powder particles significantly improved the tensile strength of the composites compared to the alloy. The improvement observed in tensile strength of the composite was attributed to the fact that the mussel shell powder acts as filler and possesses higher strength which was more resistance [24]. The mussel shell contains ceramic materials, such as CaO, SiO_2, Al_2O_3, Fe_2O_3 which had a favourable combination of density; the hardness exhibits a significant increase in its elastic modulus, hardness, strength and wear resistance, accordingly [25]. Furthermore, the studies on Al-MMCs are mainly concentrated on Al–SiC, Al–Al_2O_3 based systems with limited studies on Al–TiO_2 composites, though TiO_2 particles have excellent mechanical properties [26] and [27]. Hence, improvement in the strength of the composites can be explained by the presence of ceramic particles in the mussel shell powder. It was therefore estimated that

about 45 % increase in the tensile strength from 0 wt. % to 3 wt. % MSP and 2.30 % from 3 wt. % to 15 wt. % MSP, respectively.

3.2.3 Elongation

The percentage of elongation is shown in Fig. 6. It increases from 0 wt. % to 3 wt. % MSP and decreased from 3 wt. % to 15 wt. % MSP. However, at the particle size (100 μm) of the filler due to high surface area and good wettability, the porosity of the composite decreases, which give rise to high strength at low percentage from 3 wt. % to 15 wt. % of the filler in the matrix [28].

3.2.4 Impact Toughness

The toughness results presented in Fig. 6 showed an increase from 0 wt. % to 3wt. % and an decrease from 6 wt. % to 9 wt. % and an increase from 9 wt. % to 15 wt. % MSP. This sinusoidal change can be attributed to particle and interfacial cracking initially. The toughness values became virtually constant at 6 wt. % to 15 wt. % MSP and similar to works of [29].

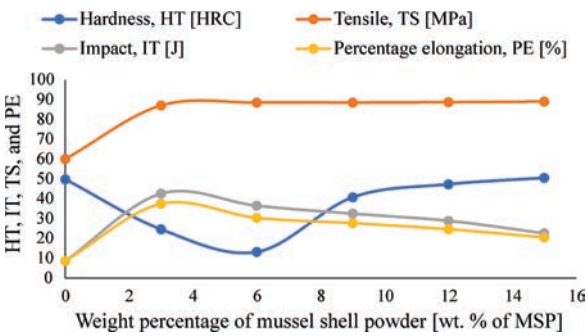

Fig. 6. *Variations of hardness, tensile, impact and elongation of Alloy and composites against wt. % MSP*

Table 5. *Values of the mechanical properties studied*

Wt. % MSP	Hardness [HRC]	Tensile stress [MPa]	Impact test [J]	Percentage elongation [%]
0	49.78	60	8.6	8.6
3	24.58	87	42.6	37.4
6	13.16	88.5	36.5	30.3
9	40.7	88.5	32.5	27.7
12	47.28	88.7	28.9	24.6
15	50.52	89	22.6	20.5

3.2.5 Bending Test

The bending test carried presented in Table 6 and Fig. 7. Bending results showed an increase from 0 wt. % to 15wt. % of mussel shell powder and made of compressive and tensile stresses. This change can be attributed to particle and interfacial cracking which confirm the results of percentage elongation and impact results and similar to the previous works of [30], and, [31].

Table 6. *Values of the Bending test at various reinforcements*

wt. % MSP	Stress [MPa]
0	119.5
3	149.7
6	150
9	154.2
12	160.3
15	165.51

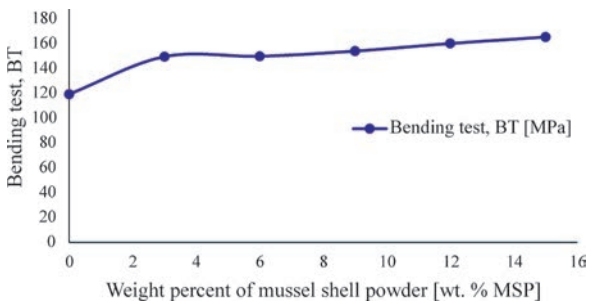

Fig. 7. *Bending test of Aluminium alloy and composites against wt. % MSP*

3.3 Wear Alloy/Composite Behaviours

Wear is the gradual loss of material due to relative motion between a surface and the contacting substance and the wear damage may be in the form of micro-cracks or localized plastic deformation [32].

From Fig. 8, the wear rate of the composite decreases with increase in the wt. % MSP reinforcement. Still in the figure, an increase in the applied load resulted in an increase in the wear rate of the samples investigated. The MSP beneficial effect on the wear resistance of the AlMgSi alloy composites is observed to be the best at low load and reduces with increase in applied load. Increases in MSP in the composite restricts deformation of the matrix material with respect to load; hence, the wear rate for the higher content of MSP composites decreases as seen in the figure and similar to work of [33]. The composites exhibited higher wear resistance at different applied loads. Wear rate at 9 wt. % MSP are 30 $mm^3/(Nm)$ and 47 $mm^3/(Nm)$ at 10 N and 20 N, respectively. This behaviour was attributed to the presence of MSP on the counter surface, which act as a transfer layer and

effective barriers to prevent large scale fragmentation of the Al-Si-Mg matrix. Fig. 9 show the uniform distribution of MSP within the matrix before and after, supported with the low wear rate obtained. The wear rate increases with increase in applied load while it decreases with increase in the volume fraction of the reinforcement, as seen in Fig. 8 and supported the findings [34].

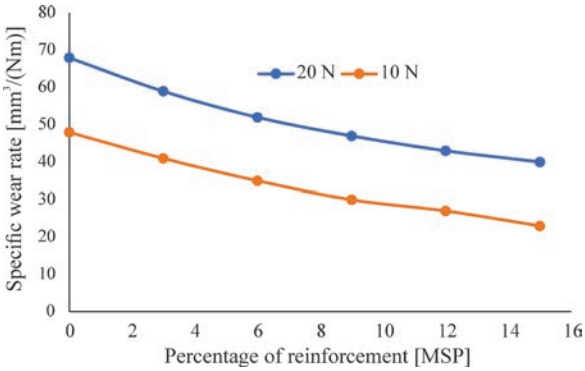

Fig. 8. *Effect of reinforcement on specific wear rate*

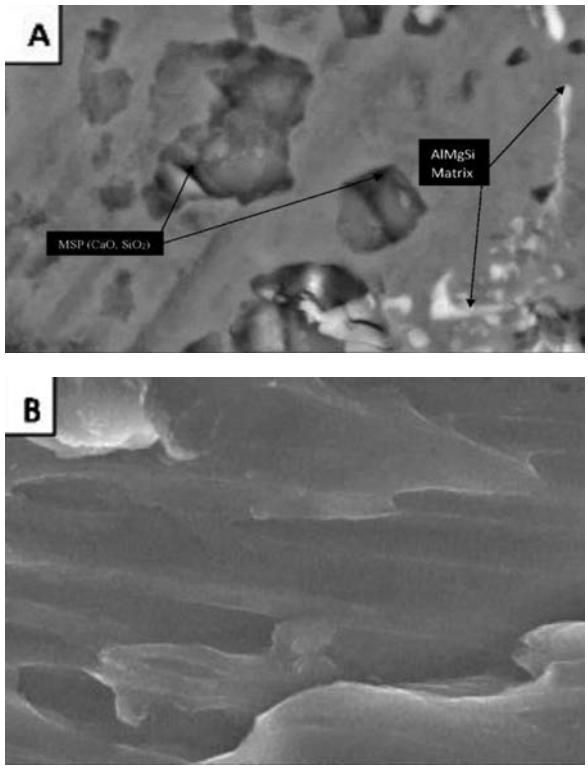

Fig. 9. *Morphology of Aluminium alloy/ 6 wt. % MSP a) before wear, and b) after wear*

Fig. 10 shows the variation of the coefficient of friction with different applied loads. The coefficient of friction of both unreinforced Al-Mg-Si alloy and Al-Mg-Si/MSP composites decreases as the applied load increase. The coefficient of friction increases as the amount of mussel shell powder particles reinforcement increases in the alloy. The amount of mussel shell powder particles was well-bonded with the matrix during sliding, the aluminium alloy matrix surrounding the particles were then worn away, which left the counter face and the reinforcing particles to be effectively in contact. If the particle has easy decohesion, contact occurred between the counter face and the matrix, and the hard particles cause a third body abrasion mechanism. It is then obvious that greater roughness and friction coefficient in the reinforced aluminium alloy (composites) than unreinforced aluminium alloy and also confirmed the previous works [34] and [35].

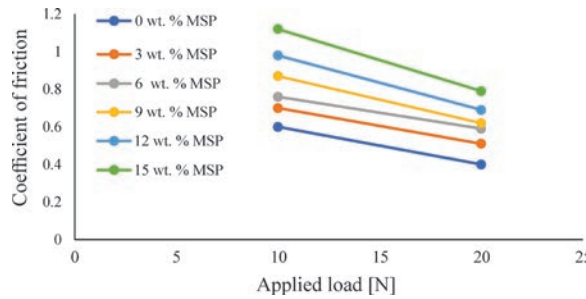

Fig. 10. *Variations of coefficient of friction with applied load*

4 CONCLUSIONS

The purpose of this work was to investigates the use of aquaculture MSP of particle size 100 µm by dispersing it into aluminium metal composites via liquid metallurgy to obtain composites for mechanical, microstructure and wear properties analyses. Therefore, the following conclusion have been drawn from the results:

1. The mussel shell powder is a potential reinforcer that had improved mechanical and wear rate behaviours investigated.
2. Hardness value decreases with increase in wt. % mussel shell powder and later increase as the wt. % of MSP was increased because of the higher particle size of MSP. The tensile strength, impact toughness, and elongation were also enhanced positively at different composition of MSP.
3. Microstructures clearly revealed that the composites materials produced by stir casting method showed no voids and discontinuities of MSP particulates in the matrix which resulted in sound castings.

4. The wear resistance of the composites increases with increase in the applied load and decrease with increase in the weight percentage of MSP.
5. The morphologies of the wear rate of the composite revealed that the material removal was mainly due to micro-cutting and as such, MSP was a good substitute for the imported material, in addition to being easily available, cheap, and environmentally friendly.

5 ACKNOWLEDGEMENTS

The authors are thankful to the staff of Department of Metallurgical and Materials Engineering, University of Nigeria, Nsukka and Department of Chemical, Metallurgical and Materials Engineering, Tshwane University of Technology, Pretoria, South Africa, Main Campus Pretoria West

6 REFERENCES

[1] Chak, V., Chattopadhyay, H., Dora, T.L. (2020). A review on fabrication methods, reinforcements and mechanical properties of aluminum matrix composites. *Journal of Manufacturing Processes*, vol. 56 p. 1059-1074. **DOI:10.1016/j.jmapro.2020.05.042**.

[2] Arunachalam, R., Krishnan, .PK., Muraliraja, R. (2019). A review on the production of metal matrix composites through stir casting–Furnace design, properties, challenges, and research opportunities. *Journal of Manufacturing Process*, vol. 42, p. 213-245, **DOI:10.1016/j.jmapro.2019.04.017**.

[3] Kala, H., Mer, K.K.S., Kumar, S. (2014). A review on mechanical and tribological behaviors of stir cast aluminum matrix composites. *Procedia Materials Science*, vol. 6, p. 1951-1960, **DOI:10.1016/j.mspro.2014.07.229**.

[4] Ofem, M.I., Umar, M., (2012). Effect of filler content on the mechanical properties of periwikle shell reinforced cnsl resin composites. *ARPN Journal of Engineering and Applied Sciences*, vol. 7, p. 212-215.

[5] Alaneme, K.K., Adewale, T.M., Olubambi, P.A. (2014). Corrosion and wear behaviour of Al–Mg–Si alloy matrix hybrid composites reinforced with rice husk ash and silicon carbide. *Journal of Materials Research Technology*, vol. 3, no. 1, p. 9-16, **DOI:10.1016/j.jmrt.2013.10.008**.

[6] Agunsoye, J.O., Talabi, S.I., Bello, S.A., Awe, I.O. (2014). The effects of cocos nucifera (coconut shell) on the mechanical and tribological properties of recycled waste aluminium can composites. *Tribology in Industry*, vol. 36, no. 2, p. 155-162.

[7] Kok, M. (2005.) Production and mechanical properties of Al203 particle-reinforced 2024 aluminium alloy composites. *Journal of Materials Process and Technology*, vol. 161, no. 3, p. 381-387, **DOI:10.1016/j.jmatprotec.2004.07.068**.

[8] Usman, A.M., Raji A., Hassan, M.A., Waziri, N.H., (2014). A comparative study on the properties of Al-7%Si-rice husk ash and Al-7%Si-bagasse ash composites produced by stir casting. *International of Journal of Engineering Sciences*, vol. 3, no. 8, p. 1-7.

[9] Umunakwe, R., Olaleye, D.J., Oyetunji, A., Okoye, O.C., Umunakwe, I.J. (2017). Assessment of the density and mechanical properties of particulate periwinkle shell-aluminium 6063 metal matrix composites (PPS-ALMMC) produced by two-step casting. *Nigerian Journal of Technology*, vol. 36, no. 2, p. 421-427, **DOI:10.4314/njt.v36i2.14**.

[10] ASTM E8 / E8M-15a (2015). *Standard Test Methods for Tension Testing of Metallic Materials*, ASTM International, West Conshohocken.

[11] ASTM E18-16 (2016). *Standard Test Methods for Rockwell Hardness of Metallic Materials*, ASTM International, West Conshohocken.

[12] Nandakumar, N., (2018). Experimental Investigation on Mechanical Properties of Al6061 Hybrid Metal Matrix Composite Reinforced with Silicon Carbide and Graphite. *International Journal of Computer Sciences and Engineering*, vol 6, no. 5, p 397-402, **DOI:10.26438/ijcse/v6i5.397402**.

[13] Pandey, U., Purohit, R., Agarwal, P., Dhakad, S.K., Rana, R.S. (2017). Effect of TiC particles on the mechanical properties of aluminium alloy metal matrix composites (MMCs). *Materials Today: Proceedings*, vol. 4, no. 4, p 5452-5460, **DOI:10.1016/j.matpr.2017.05.057**.

[14] Niranjan, K.N., Shivaraj, B.N., Sunil Kumar, M., Deepak, A.R. (2017). Study of mechanical properties on Al 6061 hybrid composites by stir casting method. *International Research Journal of Engineering and Technology*, vol. 4, no. 1, p. 1036-1040.

[15] Suleiman, I.Y., Sani, A.S., Mohammed, T.A., (2018). Investigation of mechanical, microstructure, and wear behaviors of Al-12%Si/reinforced with melon shell ash particulates. *The International Journal of Advanced Manufacturing Technology*, vol. 97, p. 4137-4144, **DOI:10.1007/s00170-018-2157-9**.

[16] Dieter, G.E. (1998). *Mechanical Metallurgy*. McGraw-Hill, New york.

[17] Meena, K.L., Manna, A., Banwait, S.S,, Jaswanti. (2013). An analysis of mechanical properties of the developed Al/SiC-MMC's. *American Journal of Mechanical Engineering*, vol. 1, no. 1, p. 14-19, **DOI:10.12691/ajme-1-1-3**.

[18] Apasi, A., Yawas, D.S., Abdulkareem, S., Kolawole, M.Y. (2016). Improving mechanical properties of aluminium alloy through addition of coconut shell-ash. *Journal of Science Technology*, vol. 36, no. 3, p. 34-43.

[19] Deuis, R.L., Subramanian, C., Yellup, J.M., (1996). Abrasive wear of aluminium composites—a review. *Wear*, vol. 201, no. 1-2, p. 132–144, **DOI:10.1016/S0043-1648(96)07228-6**.

[20] Thakur, S.K., Dhindaw, B.K. (2001). The influence of interfacial characteristics between SiCp and Mg/Al metal matrix on wear, coefficient of friction and microhardness. *Wear*, vol. 247, no. 2, p. 191–201, **DOI:10.1016/s0043-1648(00)00536-6**.

[21] Mahmoud, T. S. (2008). Tribological behaviour of A390/Grp metal matrix composites fabricated using a combination of rheocasting and squeeze casting techniques. *Proceedings of the Institution of Mechanical Engineers, Part C: Journal of Mechanical Engineering Science*, vol. 222, no. 2, p. 257-265. **DOI:10.1243/09544062JMES468**.

[22] Sozhamannan, G.G., Balasivanandha Prabu, S., Venkatagalapathy, V.S.K. (2012). Effect of processing paramters on metal matrix composites: Stir casting process. *Journal of Surface Engineered Materials and Advanced Technology*, vol. 2, no. 1, p. 11-15, **DOI:10.4236/jsemat.2012.21002**.

[23] Gomes, J.R., Ramalho, A., Gaspar, M.C., Carvalho, S.F. (2005). Reciprocating wear tests of Al–Si/SiCp composites: A study of the effect of stroke length. *Wear*, vol. 259, no. 1-6, p. 545–552, **DOI:10.1016/j.wear.2005.02.088**.

[24] Howell, G.J., Ball, A. (1995). Dry sliding wear of particulate-reinforced aluminium alloys against automobile friction materials. *Wear*, vol. 181-183, p. 379-390, **DOI:10.1016/0043-1648(95)90045-4**.

[25] Vencl, A., Bobić, I., Mišković, Z., (2008). Effect of thixocasting and heat treatment on the tribological properties of hypoeutectic Al–Si alloy. *Wear*, vol. 264, no. 7-8, p. 616-623, **DOI:10.1016/j.wear.2007.05.011**.

[26] Gireesh, Ch.H., Durga Prasad,.K.G., Ramji, K., Vinay, P.V. (2018). Mechanical characterization of aluminium metal matrix composite reinforced with aloe vera powder. *Materials Today: Proceedings*, vol. 5, no. 2, p. 3289-3297, **DOI:10.1016/j.matpr.2017.11.571**.

[27] Sharma, V.K., Singh, R.C., Chaudhary, R. (2017). Effect of fly ash particles with aluminium melt on the wear of aluminium metal matrix composites. *Engineering Science and Technology, an International Journal*, vol. 20, no. 4, p. 1318–1323, **DOI:10.1016/j.jestch.2017.08.004**.

[28] Nirmal, U-, Hashim, J., Megat Ahmad, M.M.H. (2015). A review on tribological performance of natural fiber polymeric composites. *Tribology International*, vol. 83, p. 77–104. **DOI:10.1016/j.triboint.2014.11.003**.

[29] Chauhan, H., Irfan, Chauhan, A. (2017). Variation of mechanical properties (tensile strength h & microstructure) of Al6061 / (Al_2O_3 and fly ash), hybrid metal matrix composite produced by stir casting. *International Research Journal of Engineering and Technology*, vol. 4, no. 7, p. 2407-2414.

[30] Tugiman, Ariani, F., Taher, F., Hasibuan, M.S., Suprianto (2017). The analysis of composite properties reinforced with particles from palm oil industry waste produced by casting methods. *IOP Conference Series: Materials Science and Engineering*, vol. 277, art. ID 012028, **DOI:10.1088/1757-899X/277/1/012028**.

[31] Francis Xavier, L., Paramasivam, S. (2016). Wear behavior of aluminium metal matrix composite prepared from industrial waste. *The Scientific World Journal*, vol. 2016, art. ID 6538345, **DOI:10.1155/2016/6538345**.

[32] Abdulwahab, M., Dodo, R.M., Suleiman, I.Y., Gebi, A.I., Umar, I. (2017). Wear Behavior of Al-7%Si-0.3%Mg/melon shell ash particulate composites. *Heliyon*, vol. 3, no. 8, art. ID e00375, **DOI:10.1016/j.heliyon.2017.e00375**.

[33] Phanibhushana, M.V., Chandrappa, C.N., Niranjan, H.B. (2017). Study of wear characteristics of hematite reinforced aluminum metal matrix composites. *Materials Today: Proceedings*, vol. 4, no. 2, p. 3484–3493, **DOI:10.1016/j.matpr.2017.02.238**.

[34] Chandla, N.K., Yashpal, K., Jawalkar, C.S., Suri, N.M. (2017). Review on analysis of stir casting aluminium metal matrix composites from agro-industrial waste. *i-Manager's Journal of Materials Science*, vol. 5, no. 2, p. 35-46, **DOI:10.26634/jms.5.2.13658**.

[35] Lancaster, L., Lung, M.H., Sujan, D. (2013). Utilization of agro-industrial waste in metal matrix composites: Towards sustainability. *International Journal of Environmental, Ecological, Geomatics, Earth Science and Engineering*, vol. 7, no. 1, p. 35-43, **HDL:20.500.11937/37923**.

Strojniški vestnik - Journal of Mechanical Engineering 67(2021)1-2, 36-44,

DOI:10.5545/sv-jme.2020.6937 Original Scientific Paper
Received for review: 2020-09-18
Received revised form: 2020-12-08
Accepted for publication: 2020-12-24

A Model for Material Strengthening under the Combined Effect of Cavitation-Bubble Collapse and Al_2O_3 Particles, and Its Test Verification

Lei Liu* – Huafeng Guo – Ping Yu
Xuzhou University of Technology, School of Mechanical and Electrical Engineering, China

A magnesium alloy was subjected to strengthening treatment by coupling cavitation bubbles with Al_2O_3 nanoparticles. The samples were strengthened by embedding Al_2O_3 nanoparticles with the energy generated by cavitation-bubble collapse, following which a strengthening model was established to perform test verification. The result showed that, after experiencing the combined effect for 5 min, nanoparticles appear on the sample surface, observed under the scanning electron microscope (SEM); by applying the X-ray diffractometer (XRD) and X-ray photoelectron spectrometer (XPS), it is found that the Al_2O_3 content increases, implying that Al_2O_3 particles have been embedded in the sample surface. The microhardness of the samples improves by 36 %. In terms of the strengthening mechanism under the combined effect, the energy generated due to cavitation-bubble collapse is transferred to the Al_2O_3 particles to enable them to strike the sample surface. Thus, the samples have a more gentle impact, and the transition zone with pits formed on the sample surface is significantly smoother and more continuous. Moreover, the samples are further strengthened after Al_2O_3 nanoparticles are embedded within the sample surface, as these nanoparticles present high strength and microhardness. However, with the increasing duration of the strengthening process, the failure characteristics of surface morphologies of the samples gradually develop; after experiencing the combined effect for 10 min, a large area of the surface is damaged. XRD and XPS results indicate that Al_2O_3 particles induce a decrease in the binding capacity with the surface layer of the samples and thus gradually separate from the samples. Therefore, the properties of the samples are adversely affected.
Keywords: cavitation-bubble collapse, nanoparticles, coupling, strengthening model

Highlights

- *A magnesium alloy was subjected to strengthening treatment by coupling cavitation bubbles with Al_2O_3 nanoparticles.*
- *When cavitation bubbles collapsed near the wall of the specimens, the Al_2O_3 particles would strike the surface of the Mg alloy and be embedded therein, thus strengthening the Mg alloy under the effect of shock waves formed by impingent micro-jets.*
- *The embedding of Al_2O_3 particles in the sample surface is the main factor affecting the coupled strengthening model, contributing to the strengthening of the properties of the samples.*
- *Al_2O_3 particles are exfoliated from the specimen surface with increasing duration of treatment, thus resulting in the degradation of the mechanical properties of the alloy.*

0 INTRODUCTION

Magnesium (Mg) ranks third among the metallic elements in the Earth's crust in terms of abundance; Mg and its alloys are environmentally-friendly engineering metals [1]. Although Mg alloys show many excellent properties, they exhibit lower absolute strength and hardness [2] and poorer wear resistance [3] compared with other traditional metal alloys, which hinders their more extensive application in many fields. Therefore, relieving the performance drawbacks and improving the strength and hardness of Mg alloys warrant investigation.

In recent years, corresponding strengthening theories and technologies of lightweight alloys have developed rapidly [4] to [6]. Surface aluminizing for magnesium alloy is an effective method to improve corrosion resistance [7]. Zhang and Tian [8] explored the effect of mechanical shot peening on the fatigue resistance of ZK60 Mg alloy. Cavitation bubble-based strengthening shows a similar basic principle with shot peening, through which better surface quality can be obtained; moreover, cavitation bubble-based strengthening can better improve the fatigue strength of complex or miniature parts [9]. High-speed micro-jets generated during the pulsation of cavitation bubbles are equivalent to a micro-jet mechanism by which the water hammer pressure in a flow field is applied to the surface of solid materials, thus changing the surface properties thereof [10] and [11]; Orthaber [12] designed equipment to generate cavitation bubbles by utilizing high-speed jets for the surface modification of materials. High-speed water jets increase the residual compressive stress and improve the mechanical properties of the material surface. Relative to shot peening, the resulting materials present smoother surface morphologies. The research has shown that after cavitation shot peening, the surface of pure titanium was strengthened, and the surface damage was small [13].

The morphology, texture, and grain size of the material surface can influence the material properties.

*Corr. Author's Address: School of Mechanical and Electrical Engineering, Xuzhou University of Technology, Xuzhou, China, leiliu86@sina.cn

Thus, by combining mechanical shot peening with cavitation bubble-based strengthening, tests were conducted by taking a magnesium-aluminium (Mg-Al) alloy as the research object. To be specific, Al_2O_3 nanoparticles are added in water and then embedded within the samples via the energy generated due to cavitation-bubble collapse to realize the strengthening of the samples.

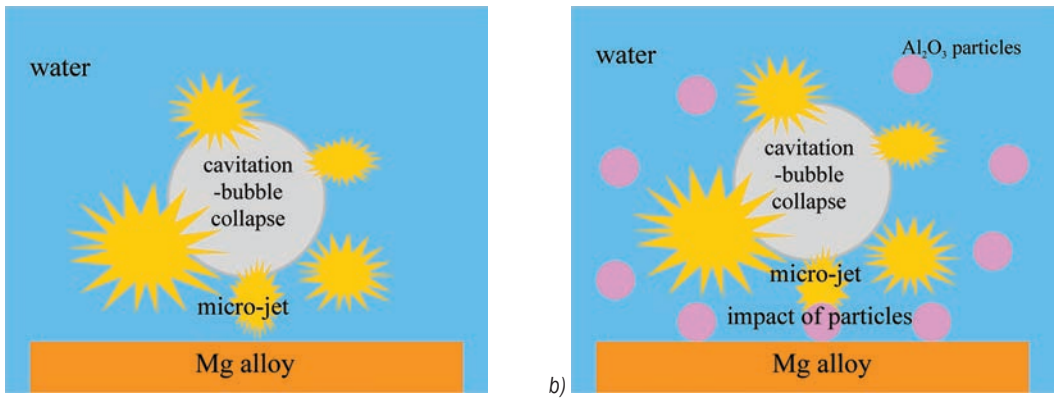

Fig. 1. *Model for material strengthening; a) cavitation bubble-based strengthening model, and b) coupled strengthening model of cavitation-bubble collapse and Al_2O_3 nanoparticles*

1 ESTABLISHMENT OF MODELS AND THEIR CHARACTERISTIC ANALYSIS

A model for material strengthening is established and investigated, as shown in Fig. 1.

1.1 Governing Fluid Dynamics Equation

After cavitation-bubble collapse, energy is mainly released in the form of micro-jets and heat. To simplify the model, it is supposed that the whole process of cavitation-bubble collapse is heat-insulated.

Model A: a cavitation bubble-based strengthening model for which the energy generated due to cavitation-bubble collapse is transformed into kinetic energy in the form of micro-jets.

Model B: a coupled strengthening model for which the energy generated due to cavitation-bubble collapse is converted into the kinetic energy of nanoparticles through micro-jets.

The motion of micro-jets satisfies the law of mass conservation, which is expressed as follows:

$$\frac{\partial \rho}{\partial t}+\frac{\partial(\rho v_x)}{\partial x}+\frac{\partial(\rho v_y)}{\partial y}+\frac{\partial(\rho v_z)}{\partial z}=0, \qquad (1)$$

where, ρ and t refer to density and time, respectively; v_x, v_y, and v_z separately denote the components of the velocity vector in the x, y, and z-directions. This indicates that the mass increment of a micro-element in the unit time is equal to the increased net mass of the micro-element at the same time.

According to the Navier-Stokes equation, the body force, pressure difference, viscous force, and inertial force of fluid micro-elements during movement reach an equilibrium.

$$\vec{f}-\frac{1}{\rho}\nabla p+\frac{\mu}{\rho}\nabla^2\vec{v}+\frac{1}{3}\frac{\mu}{\rho}\nabla\left(\nabla\cdot\vec{v}\right)=\frac{\mathrm{d}\vec{v}}{\mathrm{d}t}. \qquad (2)$$

It can be seen from Eq. (2) that viscous force plays a dominant role in micro-jets, and the fluid field significantly blocks the micro-jet. A distance of 100 μm (in water) is sufficient to decelerate the micro-jet to 2.5 m/s from the initial 755 m/s [14].

It can be seen from Eq. (1) that the mass before and after the motion of micro-jets is unchanged, and the energy lost by micro-jets is equal to the work done to overcome friction. According to the theorem of kinetic energy [15]:

$$\frac{1}{2}m\left(v_2^2-v_1^2\right)=-\int_{R_c}^{H}\frac{1}{2}C_D\rho v_1^2 S\mathrm{d}l, \qquad (3)$$

where, m, v_2, and v_1 refer to the mass of a micro-jet, the speed of the micro-jet reaching the sample surface, and the initial speed of the micro-jet, respectively; C_D, ρ, S, and l represent the drag coefficient of the micro-jet, the density of the liquid phases, the cross-sectional area of the micro-jet, and the distance from the centre of the cavitation bubbles to the sample surface, respectively; R_c and H denote the instantaneous radius at cavitation-bubble collapse and the distance from the centre of cavitation bubbles to the wall, respectively.

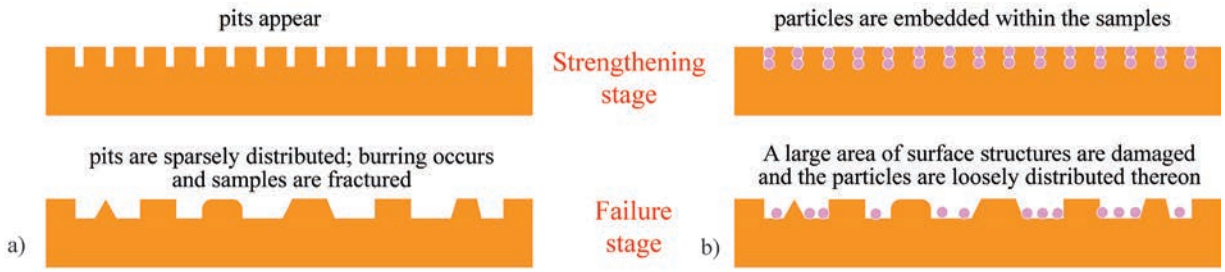

Fig. 2. *Strengthening effect and failure mechanism of the two models; a) cavitation bubble-based strengthening model, and b) coupled strengthening model*

It can be determined that, in *Model A*, the upper limit of the integral varies from H to L due to the absence of Al_2O_3 particles; however, owing to the position of cavitation-bubble collapse being close to the wall (a micron-size distance), the values of H and L are quite low. Therefore, the energy loss in *Model A* is approximately equal to that in *Model B*. Thus, it can be assumed that the energy applied to the samples by the same cavitation bubble source within the same time under the two models is equivalent.

1.2 Strengthening Effect and Failure Mechanism

The two models show the strengthening effect while they will play an adverse effect for a long time, as shown in Fig. 2.

Model A: The Mg alloy is placed into the pure water solution and strengthened based on the energy impact generated due to cavitation-bubble collapse near the wall. In the strengthening stage, because of micro-jetting, pits develop on the sample surface, and the chemical state of elements varies due to heat release during cavitation-bubble collapse; eventually, the sample surface is subjected to cavitation erosion under their long-term action.

Model B: based on the first model, Al_2O_3 nanoparticles are added in pure water, and the mixture is stirred to allow the nanoparticles to suspend in water. When the cavitation-bubble collapse occurs near the wall, the Al_2O_3 nanoparticles strike the surface of the Mg alloy at a certain speed and are embedded into the alloy under the effect of shock waves induced by the micro-jets, thus strengthening the Mg alloy. Finally, failure occurs under the long-term influence thereof.

By comparing the two functional models, it can be found that, owing to Al_2O_3 particles' favourable properties, *Model B* shows a superior strengthening effect under conditions involving the appropriate parameters. The models were verified experimentally.

2 TEST METHODS

The test was conducted by utilizing an SLQS1000 ultrasonic cavitation testing machine (Fig. 3).

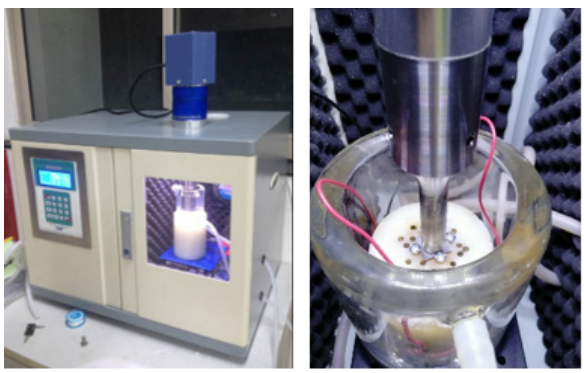

Fig. 3. *Test equipment*

The test parameters were as follows: ultrasonic power of 500 W; ultrasonic frequency of 20 kHz; the amplitude-measuring transformer with a diameter of 15 mm at a distance of 1 mm to the sample surface; the test temperature was 20 °C. The diameter of cavitation bubbles produced by ultrasonic vibration is about 2 mm to 5 mm, and the trigger frequency is about 60 Hz.

AZ31 Mg alloy specimens, measuring 20 mm × 20 mm × 0.5 mm, were selected as the research object; the diameter of Al_2O_3 particles was less than 500 nm; the Mg alloy samples were grit-polished (8000 mesh) before testing; after completing the test, the samples were cleaned, dried with cold air, then preserved in sealed containers.

The test process: the tests were separately performed based on the two function models for 5 min, 10 min, 15 min, and 20 min. At first, the strengthening effect and influence of different models within the same time were analysed; after that, the process from strengthening to failure was analysed. Hence, the proposed model was verified.

The samples were characterized and tested by applying a scanning electron microscope (SEM) (FEI Inspect F50), an X-ray diffractometer (XRD) (BRUKER D8 advance), an X-ray photoelectron spectrometer (XPS) (Thermo Fisher EscaLab 250Xi), and a Vickers hardness tester. On this basis, the changes of various parameters (including surface morphology, phase composition, chemical state, and microhardness) of the samples were explored.

3 RESULTS AND DISCUSSION

3.1 The Influence of the Mode of Treatment

Fig. 4 shows the SEM surface morphologies of the samples obtained by separately using cavitation bubble-based strengthening and coupled strengthening method after treatment for 5 min.

As shown in Fig. 4a, non-uniformly distributed circular pits with a diameter of 1 μm to 10 μm are found on the sample surface under the effect of cavitation bubbles alone: these are caused by the micro-jet impact generated by cavitation-bubble collapse. In the initial stage, slight deformation appears at the point subjected to the micro-jet impact on the sample surface and shear failure is gradually generated at the edge, thus finally forming erosion pits. Additionally, owing to the micro-jets differing in impact direction and intensity, certain positions on the sample surface are more significantly deformed; thus, the diameters of the pits differ greatly. The morphological characteristics at the scale of 1 μm in Fig. 4a are induced by the heat released during cavitation-bubble collapse.

Fig. 4b differs significantly from Fig. 4a: pits of relatively uniform size (8 μm to 10 μm) are found on the sample surface under the coupling effect of cavitation-bubble collapse and Al_2O_3 particles; moreover, it can be found that spherical particles smaller than 100 nm in diameter are present in the pits, indicating that Al_2O_3 particles are embedded within the sample surface. The strengthening mechanism after adding Al_2O_3 particles is such that the sample surface is impacted by the particles after the energy generated due to cavitation-bubble collapse is transferred to the particles instead of being directly applied to the samples; therefore, the samples are subject to a lower impact force and the transition zone with pits is more significantly continuous and smooth: this is conducive to the avoidance of unwanted deformation via microcracks and sharp edges [16]. In addition, Al_2O_3 nanoparticles present favourable

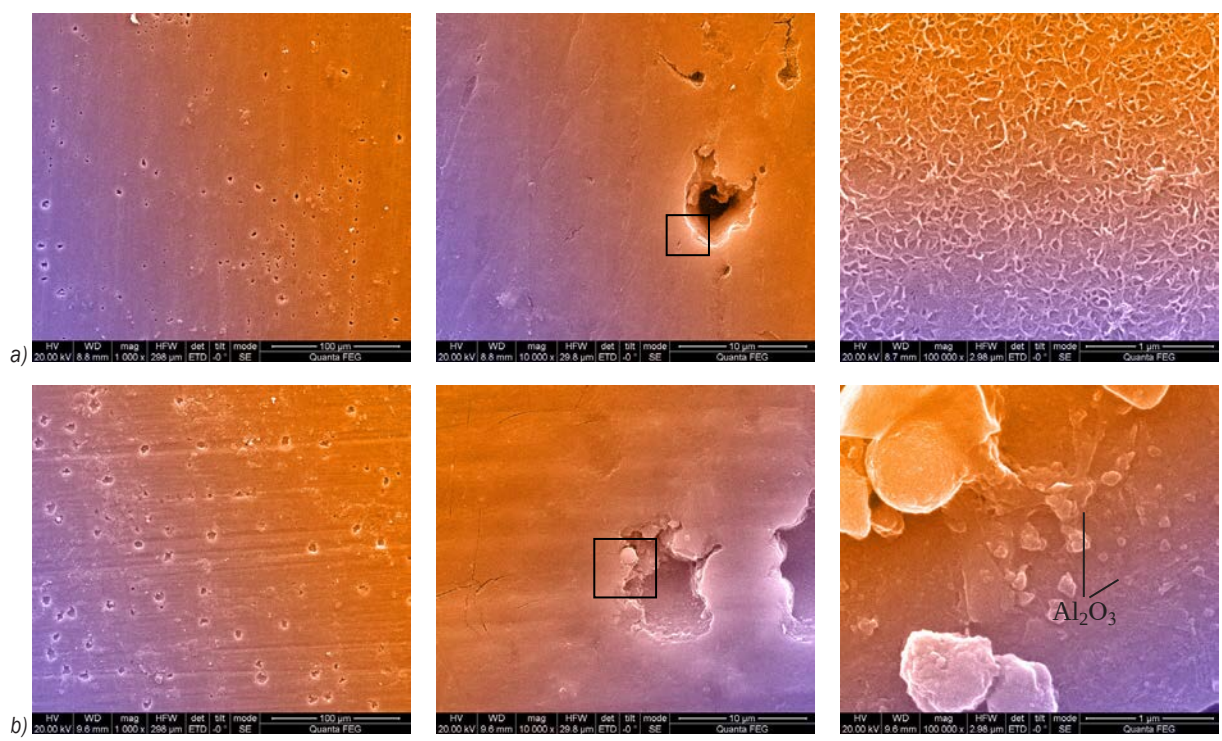

Fig. 4. *Comparison of surface morphologies of the samples after being treated for 5 min using different strengthening methods; a) cavitation bubble-based strengthening, and b) coupled strengthening*

strength and hardness and thus a better strengthening effect after they are embedded within the sample surface. Hence, it is verified that the strengthening process proposed by the models in Fig. 2 is correct. Moreover, the morphological characteristics at the scale of 1 μm in Fig. 4b are remarkably different from those under the strengthening effect of cavitation bubbles alone. This implies that most of the heat released during cavitation-bubble collapse is absorbed by Al_2O_3 particles, thus marginally influencing the surface microstructures of the samples.

The further to validate the embedment of Al_2O_3 particles, the phase spectrum of the samples is shown in Fig. 5.

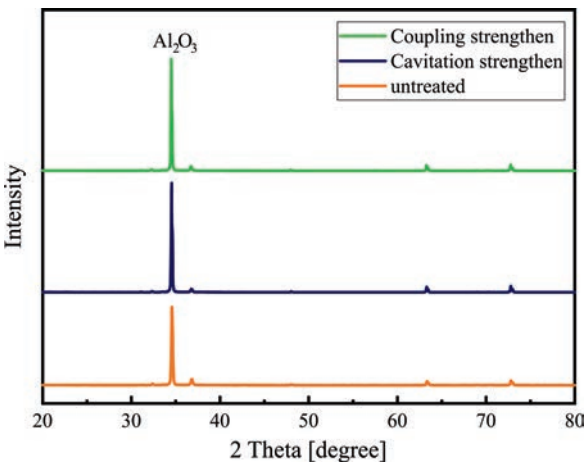

Fig. 5. *XRD spectra of the samples*

As shown in Fig. 5, the phase compositions of the original samples are consistent with those of the strengthening samples; however, the samples vary significantly in terms of their composition. According to existing research [17], the highest diffraction peak in the figure corresponds to Al_2O_3: the Al_2O_3 content in the samples after being subjected to one of the two strengthening effects both increase; however, the Al_2O_3 content is higher after application of the coupled strengthening effect, which indicates that Al_2O_3 particles are embedded within the samples, in addition to the beneficial effect of transformation of metal Al into Al_2O_3.

To analyse the changes in elemental composition in specimens under the two strengthening models, the high-resolution XPS spectra of Mg1s and Al2p for samples subject to each of the two strengthening models are shown in Fig. 6.

As shown in Fig. 6a, for the element Mg, the binding energy at the peak after the coupled strengthening is 1303.1 eV, which corresponds to metal Mg found according to previous research [18]; the binding energy at the peak after the cavitation bubble-based strengthening is 1303.6 eV, which also corresponds to metallic Mg; the peak of the original samples delivers a binding energy of 1303.9 eV, which corresponds to MgO. The reason for this is that the metal Mg on the sample surface is exposed to air for a long time and oxidized to MgO before the strengthening tests are conducted: this indicates that both the modes of strengthening change the surface morphologies and exfoliate the MgO from the original surface while exposing metal Mg at greater depth.

It can be seen from Fig. 6b that the binding energies of Al elements in the samples under the two strengthening models appear at the same position, indicating similar compositions; however, the peak intensity differs significantly: the peak under the coupled strengthening is higher than that under cavitation bubble-based strengthening. The specific parameters are as follows: the Al2p peak of the original

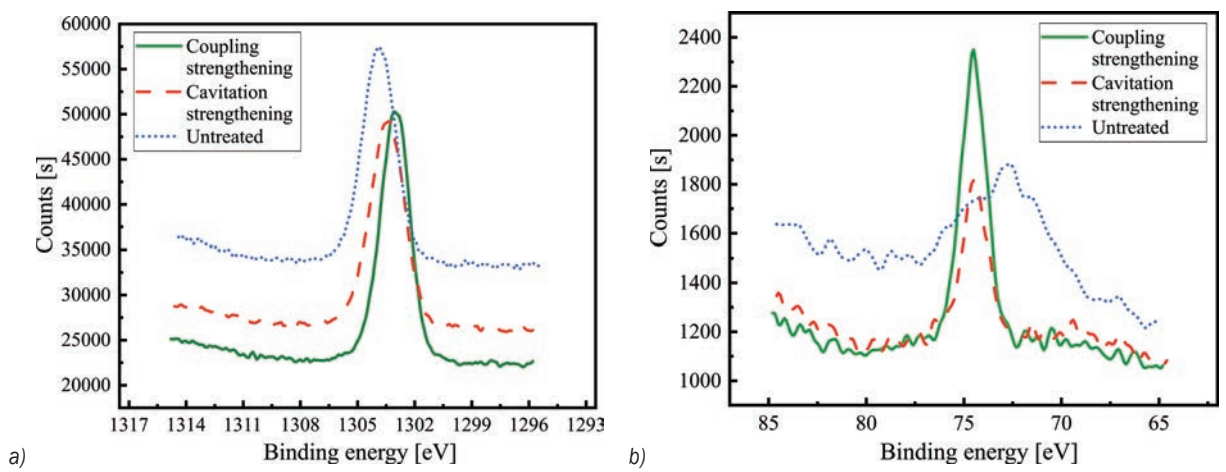

Fig. 6. *High-resolution XPS spectra; a) Mg1s, and b) Al2p*

samples corresponds to a binding energy of 72.7 eV, mainly shown as metallic Al; after cavitation bubble-based strengthening, the peak shifts to the position of high binding energy at 74.5 eV. This implies that the metallic Al is transformed into Al^{3+} in the form of Al_2O_3 due to the loss of electrons, which is attributed to heat release during cavitation-bubble collapse. Therefore, relative to the original samples, the binding energy varies while the strength of the samples remains practically unchanged after cavitation bubble-based strengthening treatment, indicating that the valence state of Al elements is changed while their content remains unchanged; after coupled strengthening, the peak also appears at 74.5 eV while there is larger binding energy. This indicates that Al_2O_3 particles in the solution are embedded within the samples adjunct to the metal Al being transformed into Al_2O_3 under the effect of heat release during cavitation-bubble collapse; therefore, the elemental Al content increases (Table 1). The correctness of the strengthening effect of the two models shown in Fig. 2 is validated again.

Table 1. *The proportional elemental Al content*

Treatment mode	Original	Cavitation bubble-based strengthening	Coupled strengthening
Content [%]	2.36	2.33	3.4

To determine the specific chemical state of the elemental Al, peak fitting was applied to the XPS curves of Al2p, as shown in Fig. 7.

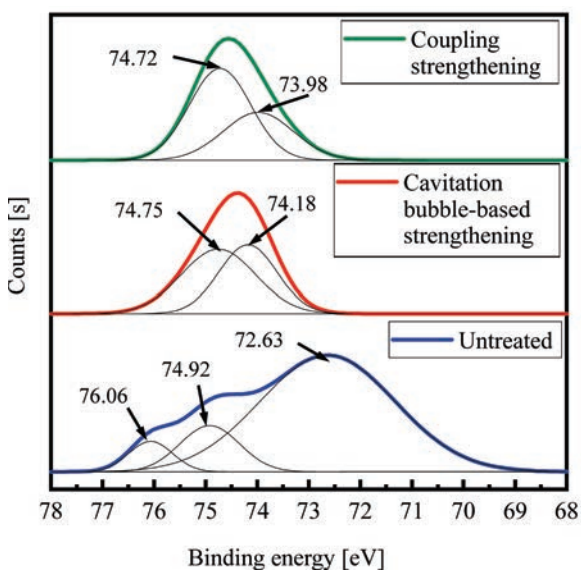

Fig. 7. *Peak fitting curves: Al2p*

As shown in Fig. 7, there are three peaks in the original samples at 72.63 eV, 74.92 eV, and 76.06 eV separately, corresponding to Al, Al_2O_3, and Al_2O_3/A1. Two peaks appear in the samples after cavitation bubble-based strengthening at 74.18 eV and 74.75 eV; two peaks occur in the samples after coupled strengthening at 73.98 eV and 74.72 eV, both corresponding to Al_2O_3.

The A12p binding energy of the aluminium-oxide tetrahedron [AlO_4] is about 73.8±0.4 eV and that of the aluminium-oxide octahedron [AlO_6] is about 74.5±0.4 eV [19]; however, the sub-peaks of Al2p under each of the two strengthening modes (Fig. 7) are located within the two ranges. This indicates that all of the Al in the samples after being subjected to the two strengthening treatments appears as Al_2O_3 while showing different coordination modes. The comparison of the surface hardness is displayed in Fig. 8.

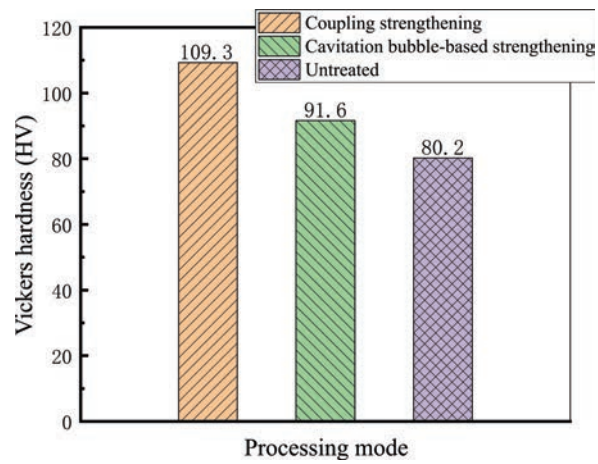

Fig. 8. *Comparison of the surface hardness of the samples after being treated for 5 min*

It can be found that the surface hardness of Mg alloy, after cavitation bubble-based strengthening for 5 min, increased by 11.4 HV and by 29.1 HV after coupled strengthening. This indicates that the strengthening effect is related to the improvement of surface morphology, and that the addition of Al_2O_3 particles also greatly enhances the strengthening effect.

3.2 The Influence of Treatment Duration

After long-term treatment under the two modes of strengthening, the surface is damaged, and the properties of the samples are impaired (Fig. 9).

As shown in Fig. 9, with prolongation of treatment, the failure characteristics of surface morphologies of the specimens under each of the two modes of strengthening appear gradually; in particular

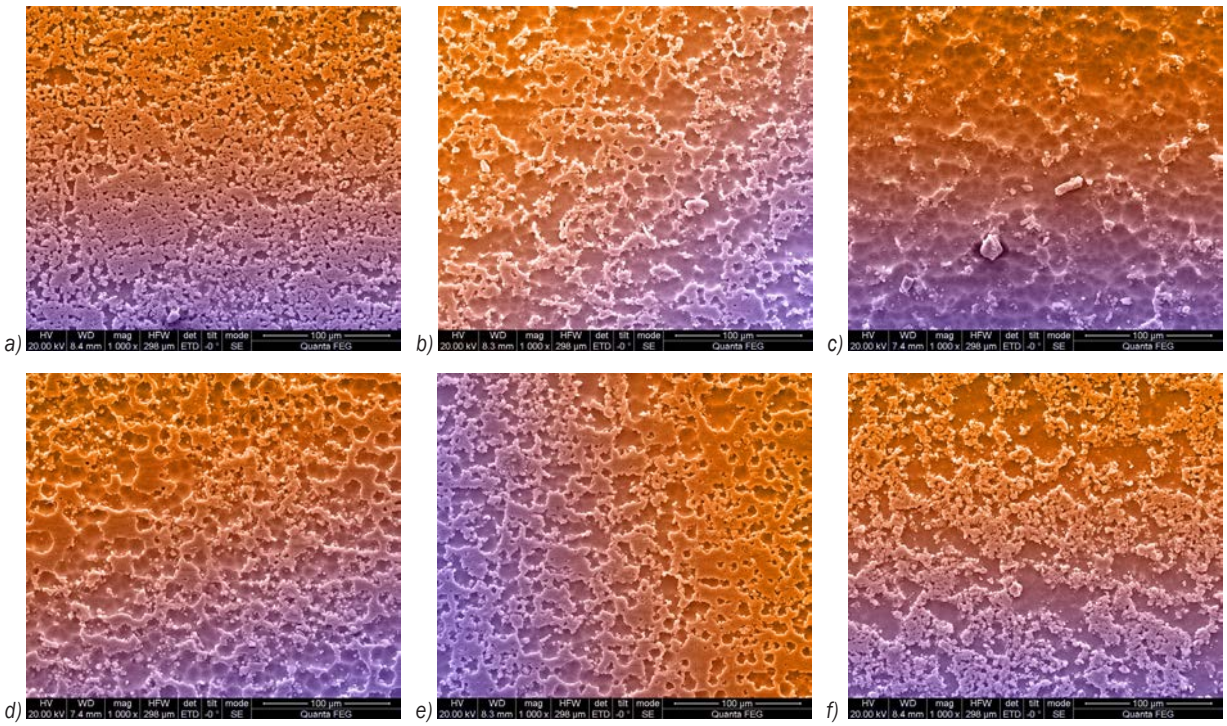

Fig. 9. *SEM surface morphologies of specimens subject to the two modes of strengthening for different times; a) bubble-based strengthening for 10 min, b) bubble-based strengthening for 15 min, c) bubble-based strengthening for 20 min, d) coupled strengthening for 10 min, e) coupled strengthening for 15 min, and f) coupled strengthening for 20 min*

the surface is more severely damaged from 15 min and onwards.

By comparing Figs 4a and 9a to c, it can be seen that after cavitation bubble-based strengthening for 10 min, micro-pits generated due to micro-jets striking the sample surface increase and their sizes also increase; moreover, the micro-pits gradually coalesce, and they tend to have completely coalesced by 20 min.

By comparing Figs. 4b and 9d to f, it can be determined that the process from strengthening to failure of the samples under the coupled strengthening mode is like that under cavitation bubble-based strengthening. The sample surface begins to suffer damage after 10 min. In this case, the binding capacity between Al_2O_3 particles and the surface layer of the samples decreases, and most particles are gradually exfoliated from the sample surface.

The correctness of the failure process proposed by the models in Fig. 2 is thus verified. As the surface is damaged, Al_2O_3 particles are exfoliated. In this context, the phase compositions of the samples remain practically unchanged while the Al_2O_3 content in the samples decreases with increasing treatment duration (Fig. 10).

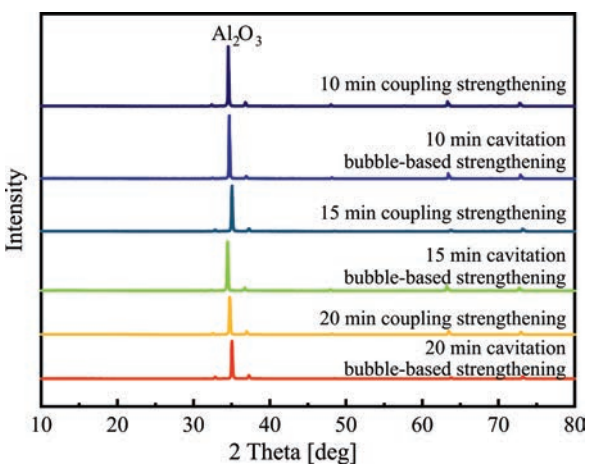

Fig. 10. *XRD spectra of the samples treated for different durations*

As shown in Fig. 10, the Al_2O_3 content decreases as a result of the long-term action of the coupling effect, and it gradually becomes equivalent to that under the influence of cavitation bubble-based strengthening. This reveals that Al_2O_3 particles have been exfoliated from the sample surface. In addition, the chemical state of Al elements tends to that under cavitation bubble-based strengthening (Fig. 11).

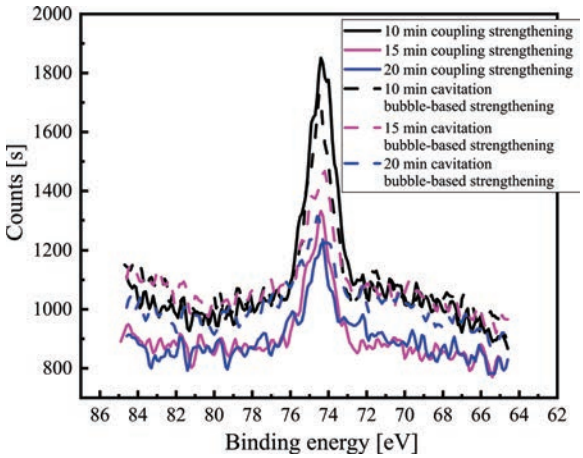

Fig. 11. *XPS spectra of Al2p treated for different durations*

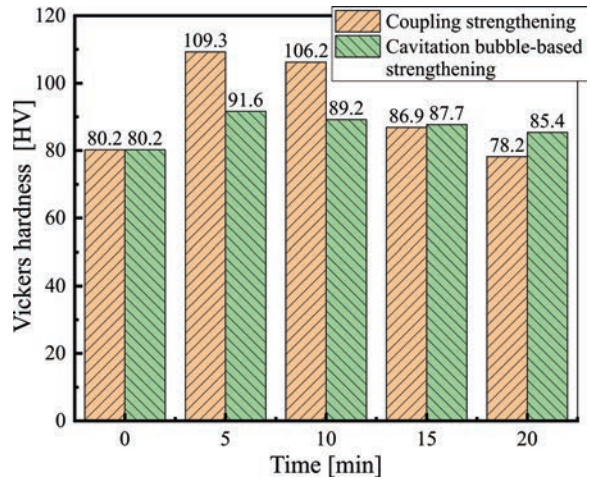

Fig. 12. *The changes in microhardness with treatment duration*

As shown in Fig. 11, the binding energy of Al element in the samples under the two functional models appears in a similar position with the change of treatment duration, implying that the same chemical state exists. After being treated from 10 min to 15 min, the peak amplitude decreases and the Al^{3+} content decreases to a significant extent, mainly due to the morphological damage; the Al_2O_3 particles, which had been deep into the sample, separated from it, so its content would decrease; after treatment for 15 min to 20 min, the peak under the cavitation bubble-based strengthening effect is higher than that under the coupled strengthening effect while the difference therein is insignificant (Table 2).

Table 2. *The proportional elemental Al content after treatment for different durations*

Time	10 min	15 min	20 min
Coupled strengthening [%]	3.82	2.43	2.41
Cavitation bubble-based strengthening [%]	2.73	2.6	2.53

The changes in microhardness with treatment duration are shown in Fig. 12.

It can be seen from Fig. 12 that the strengthening effect of the two modes of treatment on the specimens conforms to the Gaussian distribution: the optimal strengthening effect appears within 5 min to 10 min; after that, the rate of reduction of the microhardness increases, in which the microhardness declines more rapidly under the effects of coupled strengthening. Moreover, it can be seen from Fig. 9 that the failure starts after 10 min, indicating that the microhardness is related to the morphology of the specimen and the amount of Al_2O_3 particles therein.

4 CONCLUSION

A cavitation bubble-based strengthening model was established to realize shock strengthening via the energy generated by cavitation-bubble collapse near the wall of the specimens. In the strengthening stage, micro-pits were formed on the specimen surface, and the elemental composition thereof also varied; in the failure stage, the failure of surface morphologies appeared under the long-term application of the strengthening effect. The test results reveal that micro-pits on the surface are a key factor influencing the strengthening of this alloy; moreover, the transformation of Al elements from the metallic state to the oxidation state is also an important influencing factor. With the prolongation of strengthening treatment, the surface is subjected to cavitation erosion, leading to the degradation of its mechanical properties.

A coupled strengthening model involving cavitation bubbles and Al_2O_3 particles was established. When cavitation bubbles collapsed near the wall of the specimens, Al_2O_3 particles would strike the surface of the Mg alloy and be embedded therein, thus strengthening the Mg alloy under the effect of shock waves formed by impingent micro-jets; eventually, failure occurred due to long-term impact effects and Al_2O_3 particles were exfoliated from the specimen surface. The test results show that, compared with the cavitation bubble-based strengthening model, the embedding of Al_2O_3 particles in the sample surface is the main factor affecting the coupled strengthening model, contributing to the strengthening of the properties of the samples. Thus, the elemental Al content in the oxidation state is significantly higher,

and Al_2O_3 particles are exfoliated from the specimen surface with increasing duration of treatment, thus resulting in the degradation of the mechanical properties of the alloy.

5 ACKNOWLEDGEMENT

This work is supported by the University Natural Science Research Programme of Jiangsu Province (Grant No. 18KJB460028), Project of Xuzhou University of Technology (Grant No. XKY2019215), the Natural Science Foundation of Jiangsu Province (Grant No. BK20180177), and the Xuzhou Science & Technology Project (Grant No. KC18014).

6 REFERENCES

[1] Mehranpour, M.S., Heydarinia, A., Emamy, M., Mirzadeh, H., Razi, R. (2021). Enhanced mechanical properties of AZ91 magnesium alloy by inoculation and hot deformation. *Materials Science and Engineering: A*, vol. 802, p. 140667. **DOI:10.1016/J.MSEA.2020.140667**.

[2] Sun, J.P., Xu, B.Q., Yang, Z.Q. Han, J., Liang, N.N., Han, Y., Jiang, J.H., Wu. G.S. (2021). Mediating the strength, ductility and corrosion resistance of high aluminum containing magnesium alloy by engineering hierarchical precipitates. *Journal of Alloys and Compounds*, vol. 857, p. 158277, **DOI:10.1016/J.JALLCOM.2020.158277**.

[3] Ballóková, B., Falat, L., Puchý, V., Molčanová, Z., Besterci, M., Džunda, R., Abbas, A., Huang, S.J. (2020). The influence of laser surface remelting on the tribological behavior of the ECAP-processed AZ61 Mg alloy and AZ61–Al2O3 metal matrix composite. *Materials*, Vol. 13, no. 12, p. 2688, **DOI: 10.3390/ma13122688**.

[4] Luo, X.C., Zhang, D.T., Cao, G.H., Qiu, C., Chen, D.L. (2019). Multi-pass submerged friction stir processing of AZ61 magnesium alloy: strengthening mechanisms and fracture behavior. *Journal of Materials Science*, vol. 54, no. 11, p. 8640-8654, **DOI:10.1007/s10853-018-03259-w**.

[5] Straumal, B.B., Pontikis, V., Kilmametov, A.R., Mazilkin, A.A., Dobatkin, S.V., Baretzky, B. (2017). Competition between precipitation and dissolution in Cu-Ag alloys under high pressure torsion. *Acta Materialia*, vol.122, p. 60-71, **DOI:10.1016/j.actamat.2016.09.024**.

[6] Abdalla, J.A., Abu-Obeidah, A.R., Hawileh, R.A. (2019). Use of Aluminum Alloy Plates as Externally Bonded Shear Reinforcement for R/C Beams. *Procedia Structural Integrity*, vol. 17, p. 403-410, **DOI:10.1016/j.prostr.2019.08.053**.

[7] Zhang, C.H., Song, G.D., Wang, J., Zhao, X. (2020). Influence of surface nanocrystallization on aluminizing behavior of AZ91D magnesium alloy. *Rare Metal Materials and Engineering*, vol. 49, no. 2, p. 0447-0453.

[8] Zhang, W., Tian, L. (2014). Experimental study on fatigue property of ZK60 high-strength Mg alloy treated by shot peening. *Hot Working Technology*, vol. 43, no. 6, p. 153-155. (in Chinese)

[9] Takakuwa, O., Takeo, F., Sato, M., Soyama, H. (2016). Using cavitation peening to enhance the fatigue strength of duralumin plate containing a hole with rounded edges. *Surface and Coatings Technology*, vol. 307, p. 200-205, DOI:10.1016/j.surfcoat.2016.08.087.

[10] Taleyarkhan, R.P., Lapinskas, J., Xu, Y., Cho, J.S., Block, R.C., Lahey Jr., R.T., Nigmatulin, R.I. (2008). Modeling, analysis and prediction of neutron mission spectra from acoustic cavitation bubble fusion experiments. *Nuclear Engineering and Design*, vol. 238, no. 10, p. 2779-2791, **DOI:10.1016/j.nucengdes.2008.06.007**.

[11] Soyama, H. (2004). Introduction of compressive residual stress using a cavitating jet in air. *Journal of Engineering Materials and Technology*, vol. 126, no. 1, p. 123-128, **DOI:10.1115/1.1631434**.

[12] Orthaber, U., Petkovšek, R., Schille, J., Hartwig, L., Hawlina, G., Drnovšek-Olup, B., Vrečko, A., Poberaj, I. (2014). Effect of laser-induced cavitation bubble on a thin elastic membrane. *Optics & Laser Technology*, vol. 64, p. 94-100, **DOI:10.1016/j.optlastec.2014.05.008**.

[13] Cai, S.G., Liu, P.T., Zhao, X.J., Chen, C.H., Ren, R.M. (2014). Water cavitation peening-induced surface hardening and cavitation damage of pure titanium. *China Surface Engineering*, vol. 27, no. 1, p. 100-105. (in Chinese) DOI:10.3969/j.issn.1007-9289.2014.01.016.

[14] Haosheng, C., Jiang, L., Darong, C., Jidao, W. (2008). Damages on steel surface at the incubation stage of the vibration cavitation erosion in water. *Wear*, vol. 265, no. 5-6, p. 692-698, **DOI:10.1016/j.wear.2007.12.011**.

[15] Sun, Y., Huang, S.W., Mao, Y.L., Zhu, L.H. (2019). Effects of ultrasonic cavitation micro jet-flow on impact fine particle breakage near rigid walls. *China Mechanical Engineering*, vol. 30, no. 24, p. 2953-2960, **DOI:10.3969/j.issn.1004-132X.2019.24.008**. (in Chinese)

[16] Soyama, H., Takeo, F. (2016). Comparison between cavitation peening and shot peening for extending the fatigue life of a duralumin plate with a hole. *Journal of Materials Processing Technology*, vol. 227, p. 80-87, **DOI:10.1016/j.jmatprotec.2015.08.012**.

[17] Zhang, D., Yu, H.Y., Pan, X.L., Zhai, Y.C. (2015). Effect of alumina existing formation on mineralogical transformation of sintered clinker with low lime dosage. *The Chinese Journal of Nonferrous Metals*, vol. 25, no. 12, p. 3497-3504. (in Chinese)

[18] NIST X-ray Photoelectron Spectroscopy Database. National Institute of Standards and Technology, from *https://srdata.nist.gov/xps/Default.aspx*, accessed on 2012-09-15, DOI:**10.18434/T4T88K**.

[19] Wu, C.L., Wang, B.B., Tao, R., Fang, L.W., Li, H.X. (2018). Study of Mineral Structure Transformation of Coal Ash with High Ash Melting Temperature by XPS. *Spectroscopy and Spectral Analysis*, vol. 38, no. 7, p. 2296-2301, **DOI:10.3964/j.issn.1000-0593(2018)07-2296-06.** (in Chinese)

Strojniški vestnik - Journal of Mechanical Engineering 67(2021)1-2, 45-52,

DOI:10.5545/sv-jme.2020.6912 Original Scientific Paper
Received for review: 2020-08-27
Received revised form: 2020-12-16
Accepted for publication: 2021-01-14

An Investigation on Laser Welding Parameters on the Strength of TRIP Steel

Khot Rahul S[1] – T. Venkateshwara Rao[2] – Harshad Natu[3] –
H.N. Girish[4] – Tadashi Ishigaki[5] – Puttaswamy Madhusudan[6,7,*]

[1] K L University, Mechanical Department, India
[2] DBS Institute of Technology, Mechanical Department, India
[3] Magod Fusion Laser Welding System, India
[4] University of Mysore, Department of Earth Science, India
[5] Tottori University, Faculty of Engineering, Japan
[6] Environmental Engineering and Management Research Group, Ton Duc Thang University, Ho Chi Minh City, Vietnam
[7] Faculty of Environment and Labour Safety, Ton Duc Thang University, Ho Chi Minh City, Vietnam

The energy required for joining steel segments by using laser welding is relatively very low compared with arc welding, gas welding, or any other conventional welding techniques. Moreover, the rapid cooling may create a significant effect on different regions, such as the fusion zone (FZ), heat affected zone (HAZ), and base metal (BM), and in turn affect different parameters. In this study, the characteristics of the laser-welded joint were investigated by varying laser power, welding velocity and incident angle, and tensile strength. In our, experiments. the microhardness was increased by varying the power of laser welding. The strength of the joint was increased to 549 MPa with 2200 W high power, 30 mm/s velocity, and 80° laser incident angle. By increasing the power and velocity of the laser, the welding gun strength was improved; conversely, the angle of laser incident on the welding location decreased while its strength was increased.

Keywords: TRIP steel, laser welding, Nd:YAG laser, mechanical strength, microhardness

Highlights

- *The effect of laser power, laser welding velocity, and incident angle were examined, which revealed enhanced mechanical properties.*
- *Microhardness was increased to 549 MPa by increasing the power of laser welding.*
- *Welding strength is improved by varying the power and velocity.*
- *Varying the laser incident angle 9.62 % tensile strength and 67 % deformation was achieved.*

0 INTRODUCTION

Throughout the world fuel consumption is significantly increasing day by day, so to meet the increasing demand, energy costs have been considerably increasing **[1]** to **[3]**. In this regard, to reduce fuel consumption, automobile industries are considering cutting down the weight of vehicles to improve their overall performance and fuel economy **[4]** to **[6]**. The continuous development in new grades of steel from global steel industries, with the required features and ever-increasing strength, has remarkably improved the demand for advanced high-strength steels (AHSS) in the market **[7]**. The AHSS are complicated materials with precise chemical content and different phase, resulting from accurately restrained heating and cooling mechanisms **[8]** and **[9]**. Recently, a variety of strengthening methods have been developed to enhance the strength, flexibility, persistence, and lethargy properties in steel **[10]**. However, at present, tensile strengths as short of 440 MPa, are observed in several AHSS phases and hence, there is a need to utilize force as a threshold to enhance the AHSS steel. At present, it is recommended that an additional constituent of the family of AHSS-termed dual-phase (DP) steel is delicate at the sub-critical heat-damaged zone due to restraining of the martensite **[11]** to **[18]**.

Furthermore, the transformation induced plasticity (TRIP) steels with enormous strength and ductility properties has emerged as a new generation material to replace AHSS and thus to meet the requirements of automobile industries **[19]**. The base metal microstructure of TRIP steel is mainly constituted with a ferrite matrix along with trace amounts of martensite, bainite, and confined austenite alloys **[20]**. In plastic bucklings, austenite is converted into martensite to achieve superior extension steels with their excellent combination of strength and ductility **[21]** and **[22]**.

Henceforth, all the engineering applications which had been used earlier consist of straight lined joint over the levelled surface. The motivation for such variation is that the exceptional characteristics of the laser joint with the close connection between the depth and width of the joint are slightly distorted on the constituent, which can only be achieved

*Corr. Author's Address: Environmental Engineering and Management Research Group, Ton Duc Thang University, Ho Chi Minh City, Vietnam, puttaswamy.madhusudan@tdtu.edu.vn

through high welding acceleration [23]. Consequently, regarding potential industrial applications of the laser, the variations provide additional applications for laser beam welding in automobile bodies. The high-power concentration of a persistent laser beam offers many advantages over conventional joining techniques for rapid, recurring, high-quality welding of long, straight seams, and axisymmetric mechanism [24] and [25]. Furthermore, the multi-kilowatt neodymium yttrium aluminium garnet (Nd:YAG) lasers are also accessible, with the resilience of fibre optic beam distribution, and their use in the field of complex three-dimensional conversion is increasing [26]. Here, it must be mentioned that the Nd:YAG laser is a substitute beam source, which forms reasonable arrangement solutions for the welding of thin metal sheet production. Nevertheless, it also has defects in geometry, adhering gaps, or inhomogeneities in the material or its exterior that are vulnerable to the charge or generated by previous construction operations [27]. Yang et al. [28] illustrated that in the double-adjoin laser beam welding, the constraint such as incident beam position, beam angle, and beam dissolution distance greatly influence the metallurgical quality of the T-joints.

The laser beam welding (LBW) technique is one of the advanced automated techniques used in recent times. Primarily, there are two main LBW modes: the profound infiltration (or keyhole) welding method and the thermal conduction welding method. Further, the differences in laser wavelength, beam quality, and power induced are accountable for diverse welding development and their outcome [29]. Also, the ultimate tensile strength (UTS) and average yield strength (YS) of the soldered joint were not deprived related to base metal despite their existing softened zone. This claim has been further specified by Rizzi et al. [30] who extensively researched laser joining of TRIP, DP, and martensitic steels

Furthermore, Xia et al. [18] engaged laser welding on the Al-alloyed TRIP steel and observed that ferrite was solitary of the prevalent time in the fusion zone due to the ferrite-balance possessions of Al. Nevertheless, related to previous welding procedures, such as arc welding, solid-state welding, induction welding, and friction stir welding, less heat is coupled into the workpiece during laser welding, which arises in a heat-affected zone with low deformation [31] to [34]. To produce multiple phases in steels, with retained austenite (RA), martensite (M), ferrite (F), and tempered martensite (TM), a new heat treatment process was proposed and implemented [35] to [39].

In this manuscript, the laser welding of TRIP steel was explored by the laser beam welding process utilizing a high-quality Nd:YAG laser beam. The characterization of material was investigated, and the influence of different welding conditions, including the angle of the weld, the velocity of laser welding, and power of beam on the strength of the joint, was investigated. Furthermore, the microstructure, tensile behaviour, microhardness of TRIP laser-welded sheets, and their behaviour on the heat-affected zone (HAZ) and fusion zone (FZ) were examined and discussed.

1 MATERIALS AND METHODS

The TRIP steels under investigation were supplied by Nextgen Steels and Alloys Company in the form of a cold-drawn sheet with a thickness of 2 mm. The weld was performed on the transverse direction of the length of the specimen, which is prepared as per the ASTM E8/E8M [40] standards with the desired length. The laser welding setup with a schematic diagram along with the chemical compositions and mechanical properties of as-prepared materials can be obtained from our recent publication [41].

The TRIP steel sheets were welded using a Nd: YAG laser power welding system. The GmbH 56218 series laser machine (Karlich Germany) with three-phase 50 Hz to 60 Hz frequency, maximum power of 13.5 kW, and a 400 V to 480 V ±10 % power source and 900 nm to 1300 nm wavelength laser was used for welding. Furthermore, the butt welding was performed employing an ABB six-axis robot arm, which efficiently handles the welding process with a minimum scrap of 6 kg payload carrying capacity. The welding velocity was kept at 25 mm/s with a power of 2000 W, the beam diameter of 0.6 mm, and a focal distance of 113 m. The welding angle is considered to be 90° for the working table. The experimental setup and laser welding performance are shown in Fig. 1. In a typical experimental section, three different input variables were employed with different permutations and combinations. A sequence numbering system was specified for each sample according to the preparation conditions. The first number specifies the power used in the experiment, while the second number specifies the velocity, and the third number specifies the angle of the laser incident applied in the experiment. As shown in Fig. 2, the first number 1 indicates a laser beam of 1800 W power, while the second number 1 indicates 25 mm/s velocity used and the last number 1 indicates the laser incident angle employed during the experimental setup. Furthermore, the corresponding

input parameters are tabulated in Table 1. A total of 27 specimens with (3^3) diagonal array was investigated for different welding parameters, such as the angle of the weld, the velocity of laser welding, and power of beam on strength of the joint.

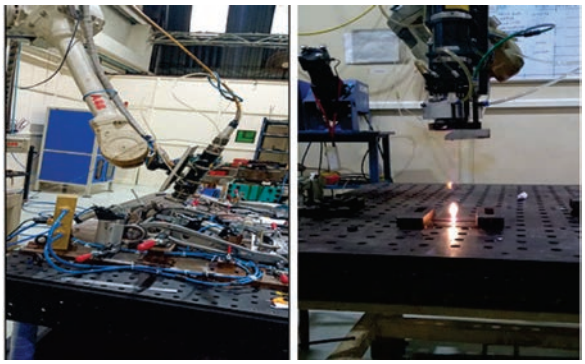

Fig. 1. *Laser welding setup with performing welding of plates*

The as-prepared samples were assessed for microstructure at FZ, HAZ, and base metal (BM), along the transverse cross-section of weldments. The cross-sections were mounted in black Bakelite power and heated at 70 °C followed by polishing using different silicon carbide grit paper. After polishing, the samples were further polished with a lapping machine using alumina powder with water. The polished samples were dipped in the 5 % nital solution and 95 % of methanol solution and used for further characterization. The microstructure deformation and ultimate tensile test were measured using a universal testing machine (UTM), manufactured by SAR Testing Systems with Model No. STS 248 with an operating velocity of 5 mm/min and the precision of the machine is ±1 %. The thermal image was recorded using a Testo 875i thermal imaging camera.

Table 1. *Levels of input parameters*

Level no.	Power (first digit) [W]	Velocity (second digit) [mm/s]	The angle of laser (third digit) [deg]
1	1800	25	80
2	2000	28	90
3	2200	30	100

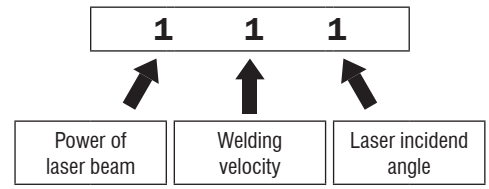

Fig. 2. *A nomenclature system for sample numbering*

2 RESULTS AND DISCUSSION

2.1 Microstructure Analysis

The microstructure of TRIP steel is composed of ferrite matrix along with varied fractions of bainite,

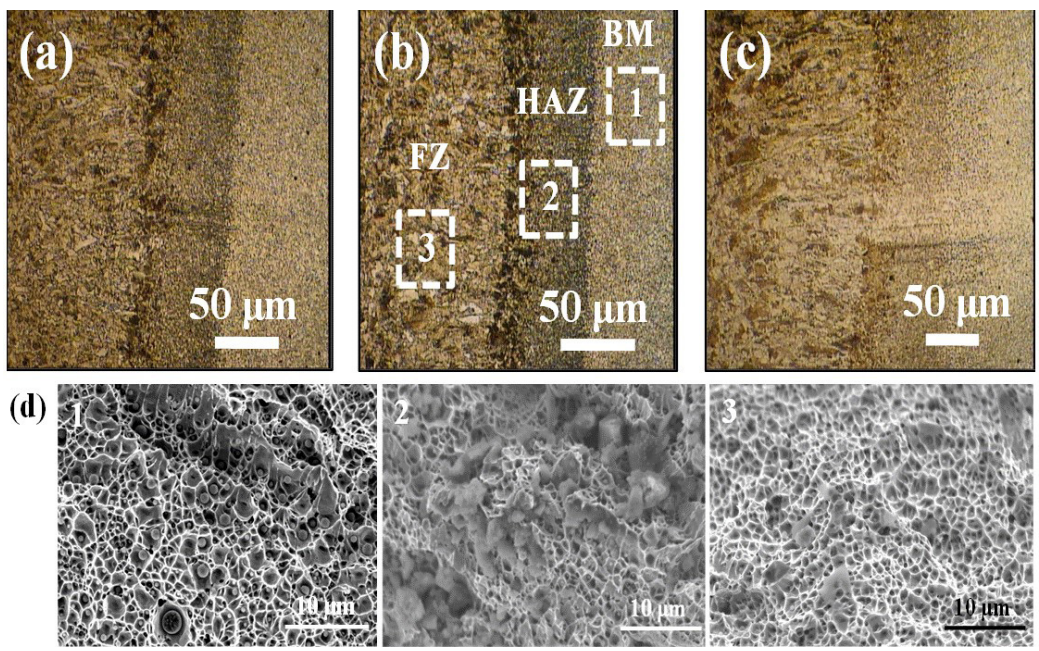

Fig. 3. *The microstructure of joint with different specimen a) 311, b) 322, c) 333 and d) FESEM images of the white rectangles in (b)*

martensite, and retained austenite. The microstructure of samples 311, 322, and 333 were measured using an optical microscope, Reichert (Austria) and the results are illustrated in Fig. 3. From Fig. 3a, it could be observed that the microstructures predominantly consist of ferrite as base metal throughout the samples and in the welding section, a segregated form of ferrite was observed along with some amount of bainite at weld imperfections with a significant absence of fractures. Furthermore, the measurement of FZ and HAZ zone was calculated on butt joints at three different locations: at the radiation exposure side, a centre of the weld, and the weld root region. As seen in Fig. 3b, the steel structure is divided into three distinct phases: FZ, HAZ, and BM marked as 1, 2, and 3, respectively. The boundary between the BM/HAZ and FZ/HAZ is very well demarcated with colour contrast and grain size boundary difference. Moreover, to understand the surface morphology of the three distinct phases, in Fig. 3b, field emission scanning electron microscopy (FESEM) was conducted, and the results are illustrated in Fig. 3d. From the FESEM images, it can be observed that the grain size distribution in HAZ is quite uniform with rounded smaller voids and less porous, whereas it should be noted that the BM and FZ displayed higher proportion and larger voids than that of the HAZ section.

2.2 Microhardness Analysis

The microhardness was measured using the Everone/MH-3 testing machine with 1000 gf load and 10 s dwelling time as a standard. The tests were performed at a distance of 0.5 mm from the top surface of the upper plate. When the power was kept at 2200 W, and other parameters are reserved at low conditions, it showed 185 HV1.0/10 hardness, when the other parameters were moved to its higher level, i.e., 30 mm/s velocity and 100° laser incident angle, then the hardness increased to 195 HV1.0/10. Nevertheless, when the power was kept at 1800 W, the hardness value significantly reduced to 110 HV1.0/10 for 90° angle and 116 HV1.0/10 for 100°. It is interesting to observe that when the velocity of the laser beam and laser incident angle were kept constant (i.e., 28 mm/s, and 90° incident angles with 2000 W power), the microhardness value reached 168 HV1.0/10. The corresponding microhardness value concerning the sample condition is shown in Table 2. From the above results, it is obvious that the microhardness value considerably changed as the power of laser welding, laser incident angle, and laser welding velocity was varied.

Table 2. *Microhardness values changing as per the sample condition is different*

Sample conditions	Hardness [HV1.0/10]
311	186
333	195
222	168
323	172
112	110
113	116
213	184
322	180
232	180
331	176

2.3 Tensile Strength Analysis

The optimum welding velocity for the prevention of porosity and crumple of the keyhole in weld samples was adopted from the previous publication results [35]. These values are used as a standard to attain the essential weld properties include strengthening at the reverse side of the weld, least allocation in micro-hardness, and homogeneous microstructure. Furthermore, during the joining process, it was observed that the power density for each procedure could be determined from the subsequent equation.

$$HI = \eta \frac{P_{Laser}}{S\left(\frac{\pi D^2}{4}\right)}, \quad (1)$$

where P_{Laser} is the laser power [W], η is the competence of the laser for low-carbon steel that was measured to be 0.6, while, S is the scan velocity [s], D is the diameter of the laser spot (0.4 mm).

2.3.1 Velocity

During the experimental condition, three different velocities are considered, as discussed previously. As shown in Fig. 4, when velocity is kept constant at 1800 W and indecent angle maintained at 80° and by altering the velocity, the change in maximum load withstand capacity, total strength, and deformations were observed. By altering the velocity load-carrying capacity, an increase in tensile strength with increased elongation was observed. Furthermore, by increasing the velocity from 25 mm/s to 30 mm/s and because of high velocity and rapid cooling of steel weld,

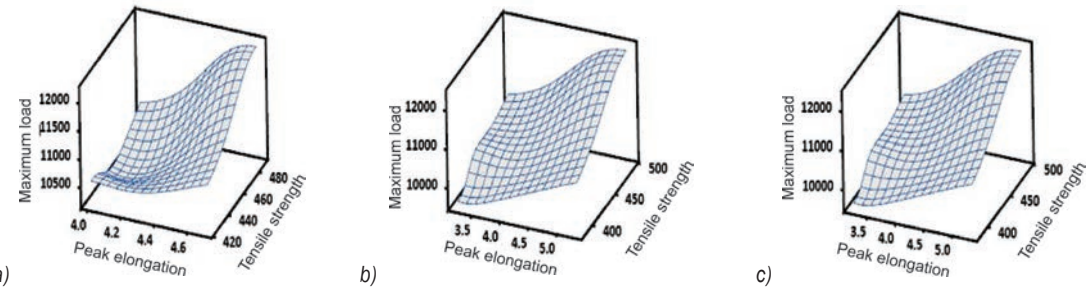

Fig. 4. *The surface plot of maximum load vs.tensile strength and peak elongation for keeping laser power and angle of the weld is constant; a) velocity 25 mm/s, b) velocity 28 mm/s, and c) velocity 30 mm/s (aspect ratio 5:4)*

the nature of elongation curve changed from a limp shape to a stiff shape, indicating an increase of tensile strength in as-prepared steel weld.

2.3.2 Laser Power

The power of the welding gun is kept constant at 2.2 kW and the variation was performed in terms of weld velocity and angle of laser incident. The velocities are 25 mm/s, 28 mm/s, and 30 mm/s, and the angle of the laser incident is changed from 80°, 90°, and 100°. As shown in Fig. 5, it could be observed that at 2200 W power and 25 mm/s velocity the tensile strength was decreased with an increase in laser incident angle from 80° to 100°. Furthermore, the deformation changed from 5.5 mm to 5.1 mm with an increase in incident angle. Interestingly, a minor increase in tensile strength was observed when the incident angle was changed from 90° to 100°. Also, as shown in Table 3, the tensile strength increased to 500.98 MPa for a joint prepared at 2.2 kW power, 25 mm/s velocity, and 80° incident angle. As the velocity was changed from 25 mm/s to 28 mm/s, the tensile strength was increased to 531.55 MPa; furthermore, when the incident angle was set to 100° the tensile strength enhanced to 549.19 MPa. When the velocity was increased from 25 mm/s to 28 mm/s and fixing the laser incident angle to 80°, the strength of the steel was improved, in contrast,

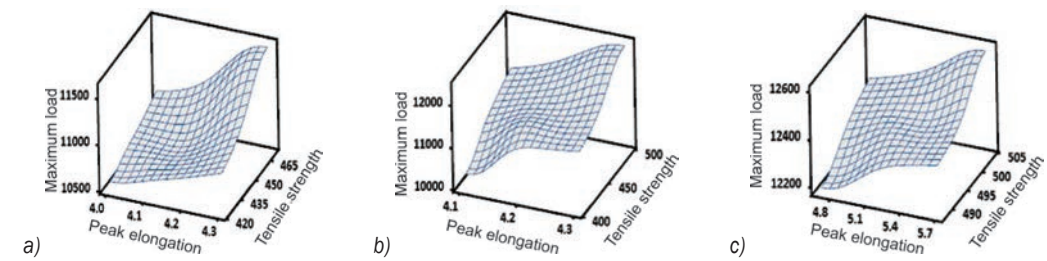

Fig. 5. *The surface plot of maximum load vs.tensile strength and peak elongation for keeping laser beam velocity and angle of the weld are constant; a) power 1800 W, b) 2000 W and c) 2200 W (aspect ratio 5:4).*

Table 3. *Variations in tensile strength by changing the velocity of the laser beam*

Serial no.	Sample number	Maximum load [N]	Peak elongation [mm]	Break load [N]	Break elongation [mm]	Tensile strength [N/mm^2]
1	311	12,524.4	4.8	10,887.8	5.5	500.98
2	312	12,191.2	4.7	11,064.2	5.4	487.65
3	313	12,299.0	4.8	12,034.4	5.1	491.96
4	321	13,897.6	8.5	12,289.2	8.8	531.55
5	322	12,376.6	5.3	11,260.2	5.9	494.71
6	323	10,917.2	4.5	10,035.2	4.5	486.69
7	331	13,729.8	8.9	12,299.0	9.2	549.19
8	332	12,602.8	5.7	10,113.6	6.3	504.11
9	333	12,014.8	4.4	7,379.4	5.2	480.59

the deformation changed from 5.5 mm to 8.8 mm. When the laser incident angle was set at 100°, the deformation of 9.2 mm was achieved. Interestingly, as the incident angle changed from 80° to 100° the ultimate tensile strength was increased by 9.62 % and in contradiction, the deformation was improved by 67 %. As shown in Table 4, it could be observed that at the laser incident angle of 100°, a lesser deviation occurred in the ultimate tensile strength and deformation. From the experimental results, it could be concluded that as the incident angle is increased the strength and deformation of the welded steel also increased.

Table 4. *Angle versus tensile strength difference results*

Serial. No.	Angle [°]	Tensile strength difference [MPa]
1	80	30.57
		17.65
2	90	7.06
		9.41
3	100	-5.27
		-8.10

2.4 Finite Element Analysis

The finite element analysis (FEA) is performed using Simufact software and the results show that the failure strength is nearly the same as in the experimental results. For instance, the ultimate strength of sample no 312 is determined to be 487.65 MPa; in contrast to the Simufact software analysis, it is revealed to be 485.18 MPa. These results clearly illustrate that there is an exceptionally less deviation as in software results with the ideal measured conditions [42] and [43]. Furthermore, the finite element modelling (FEM) was performed using Simufact welding software to understand the temperature-dependent thermophysical and mechanical properties of matter. Fig. 6 illustrates the temperature field in the selected time during the laser beam welding of sample number 312 with a laser power of 2200 W, the velocity of the laser beam is 25 mm/s, and the laser incident angle is 90º. The fusion zone is very narrow, and the temperature of the base metal distant from the weld centreline remained practically unchanged. Accordingly, the ultimate tensile strength of welded TRIP steel depending on the input parameters and its thermomechanical treatment showed an ultimate strength of 485.18 MPa. Due to the effect of the laser power, the temperature is very high, but the is transferred to the atmosphere through conduction, convection, radiation; all of this has to be completed within a split of a second. According to Fig. 6, the nuclear region is associated with a higher yellow zone, which has a higher temperature than other regions. The free end marked in blue indicates the temperature below the merging zone temperature.

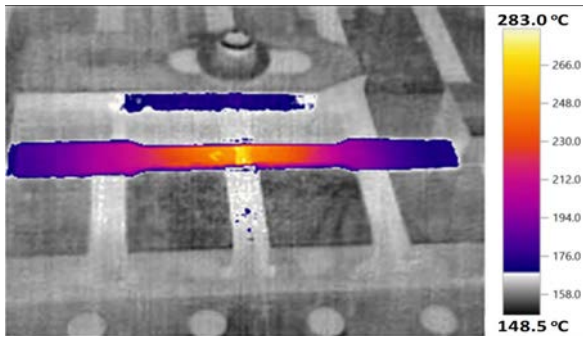

Fig. 6. *Thermal image capture for sample no. 312 (Scale: 1 mm = 20 mm with actual dimension)*

3 CONCLUSIONS

In this manuscript, the TRIP steel joints were characterized to understand their microhardness, tensile strength, and deformation, for laser power, laser incident angle, and laser welding velocity. The experimental result with sample no. 312 showed an ultimate strength of 487.65 MPa, in contrast to the simulation software, which showed the ultimate strength as 485.18 MPa, which is relatively less deviation from the experimental results. Furthermore, from the experimental results, it is clear that the laser incident angle played a substantial role in the enhancement of as-prepared steel strength. The maximum ultimate strength of 549 MPa was observed at an 80º incident angle with 30 mm/s velocity, and 2200 W power. Also, it could be observed that the deformation value and steel strength had increased as the power and velocity increased. Furthermore, our microstructure study illustrated that the microhardness in the fusion zone was increased to 185 HV1.0/10 by increasing the power and keeping the other parameters at a low level.

Nevertheless, by further increasing the power and velocity, the microhardness value could be increased to 195 HV1.0/10. Conversely, if the power is kept at the lower side (i.e., 1800 W), then the microhardness value dropped to 116 HV1.0/10. The finite element modelling showed no cracks or pores, confirming that as-prepared specimens are less thermally deformed.

4 ACKNOWLEDGEMENTS

The authors would like to thank Marathwada Mitra Mandal's College of Engineering (MMCOE) Karvenagar for providing characterization equipment. Dr Puttaswamy Madhusudan would like to acknowledge Ton Duc Thang University, Ho Chi Minh City, Vietnam for their financial support.

5 REFERENCES

[1] Rajashekhar, S.S., Molian, P. (2009). Yb:YAG laser welding of TRIP780 steel with dual-phase and mild steels for use in tailor welded blanks. *Materials & Design*, vol. 30, no. 10, p. 4146-4155, **DOI:10.1016/j.matdes.2009.04.033**.

[2] Wei, H., Zhang, Y., Tan, L., Zhong, Z. (2015). Energy efficiency evaluation of hot-wire laser welding based on process characteristic and power consumption. *Journal of Clean Production*, vol. 87, p. 255-262, **DOI:10.1016/j.jclepro.2014.10.009**.

[3] Quazi, M.M., Ishak, M., Fazal, M.A., Arslan, A., Rubaiee, S., Qaban, A., Aiman, M.H., Sultan, T., Ali, M.M., Manladan, S.M. (2020). Current research, and development status of dissimilar materials laser welding of titanium and its alloys. *Optics & Laser Technology*, vol. 126, art. ID 106090, **DOI:10.1016/j.optlastec.2020.106090**.

[4] Aslanlar, S. (2006). The effect of nucleus size on mechanical properties in electrical resistance spot welding of sheets used in automotive industry. *Materials & Design*, vol. 27, no. 2, p. 125-131, **DOI:10.1016/j.matdes.2004.09.025**.

[5] Zhang, X.Q., Chen, G.L., Zhang, Y.L. (2008). Characteristics of electrode wear in resistance spot welding dual-phase steels. *Materials & Design*, vol. 29, no. 1, p. 279-283, **DOI:10.1016/j.matdes.2006.10.025**.

[6] Razmpoosh, M.H., Macwan, A., Biro, E., Zhou, Y. (2020). Microstructure and dynamic tensile characteristics of dissimilar fiber laser welded advanced high strength steels. *Materials Science and Engineering: A*, vol. 773, art. ID 138729, **DOI:10.1016/j.msea.2019.138729**.

[7] Vercruysse, F., Castro Cerda, F.M., Verleysen, P., Petrov, R.H. (2020). Behavior of ultrafast annealed advanced high strength steels under static and dynamic conditions. *Materials Science and Engineering: A*, vol. 780, art. ID 139168, **DOI:10.1016/j.msea.2020.139168**.

[8] Mahmoudiniya, M., Kokabi, A.H., Goodarzi, M., Kestens, L.A.I. (2020). Friction stir welding of advanced high strength dual phase steel: Microstructure, mechanical properties and fracture behavior. *Materials Science and Engineering: A*, vol. 769, art. ID 38490, **DOI:10.1016/j.msea.2019.138490**.

[9] Sun, Y.F., Fujii, H., Takaki, N., Okitsu, Y. (2013). Microstructure and mechanical properties of dissimilar Al alloy/steel joints prepared by a flat spot friction stir welding technique. *Materials & Design*, vol. 47, p. 350-357, **DOI:10.1016/j.matdes.2012.12.007**.

[10] Ding, F.X., Lan, L.F., Yu, Y.J., Man, M.K. (2020). Experimental study of the effect of a slow-cooling heat treatment on the mechanical properties of high strength steels. *Construction and Building Materials*, vol. 241, art. ID 118020, **DOI:10.1016/j.conbuildmat.2020.118020**.

[11] Saha, D.C., Westerbaan, D., Nayak, S.S., Biro, E., Gerlich, A.P., Zhou, Y. (2014). Microstructure-properties correlation in fiber laser welding of dual-phase and HSLA steels. *Materials Science and Engineering: A*, vol. 607, p. 445-453, **DOI:10.1016/j.msea.2014.04.034**.

[12] Xia, M., Biro, E., Tian, Z., Zhou, Y.N. (2008). Effects of heat input and martensite on HAZ softening in laser welding of dual-phase steels. *ISIJ International*, vol. 48, no. 6, p. 809-814, **DOI:10.2355/isijinternational.48.809**.

[13] Biro, E., McDermid, J.R., Embury, J.D., Zhou, Y. (2010). Softening kinetics in the subcritical heat-affected zone of dual-phase steel welds. *Metallurgical and Materials Transaction A*, vol. 41, p. 2348-2356, **DOI:10.1007/s11661-010-0323-2**.

[14] Baltazar Hernandez, V.H., Nayak, S.S., Zhou, Y. (2011). Tempering of martensite in dual-phase steels and its effects on softening behavior. *Metallurgical and Materials Transaction A*, vol. 42, p. 3115-3129, **DOI:10.1007/s11661-011-0739-3**.

[15] Nayak, S.S., Baltazar Hernandez, V.H., Zhou, Y. (2011). Effect of chemistry on nonisothermal tempering and softening of dual-phase steels. *Metallurgical and Materials Transaction A*, vol. 42, p. 3242-3248, **DOI:10.1007/s11661-011-0868-8**.

[16] Biro, E., Vignier, S., Kaczynski, C., Mcdermid, J.R., Lucas, E., Embury, J.D., Zhou, Y.N. (2013). Predicting transient softening in the sub-critical heat-affected zone of dual-phase and martensitic steel welds. *ISIJ International*, vol. 53, no. 1, p. 110-118, **DOI:10.2355/isijinternational.53.110**.

[17] Zhao, L., Wibowo, M.K., Hermans, M.J.M., van Bohemen, S.M.C., Sietsma, J. (2009). Retention of austenite in the welded microstructure of a 0.16C-1.6Mn-1.5Si (wt%) TRIP steel. *Journal of Materials Processing Technology*, vol. 209, no. 12-13, p. 5286-5292, **DOI:10.1016/j.jmatprotec.2009.03.017**.

[18] Xia, M., Tian, Z., Zhao, L., Zhou, Y.N. (2008). Metallurgical and mechanical properties of fusion zones of TRIP steels in laser welding. *ISIJ International*, vol. 48, no. 4, p. 483-488, **DOI:10.1016/j.jmatprotec.2009.03.017**.

[19] Jeon, W.S., Sharma, A., Jung, J.P. (2020). Liquid metal embrittlement of galvanized TRIP steels in resistance spot welding. *Metals*, vol. 10, no. 6, art. ID 787, **DOI:10.3390/met10060787**.

[20] Gonçalves, T.S., de Faria, G.L., de Siqueira, R.H.M., de Lima, M.S.F. (2020). Weldability and mechanical behavior of laser-welded TRIP 750 steel sheets. *International Journal of Advanced Manufacturing Technology*, vol. 107 p. 2807-2815, **DOI:10.1007/s00170-020-05223-y**.

[21] Polatidis, E., Čapek, J., Arabi-Hashemi, A., Leinenbach, C., Strobl, M. (2020). High ductility and transformation-induced-plasticity in metastable stainless steel processed by selective laser melting with low power. *Scripta Materialia*, vol. 176, p. 53-57, **DOI:10.1016/j.scriptamat.2019.09.035**.

[22] Wang, X.H., Kang, J., Li, Y.J., Yuan, G., Misra, R.D.K., Wang, G.D. (2020). Characterisation on Al-bearing hot-rolled TRIP steel produced through isothermal bainite transformation. *Materials Science and Technology*, vol. 36, no. 2, p. 210-222, **DOI:10.1080/02670836.2019.1695079**.

[23] Atílio, I., Braga, V., de Siqueira, R.H.M., de Carvalho, S.M., de Lima, M.S.F. (2020). Comparing the weldability of AA60013-T4

aluminum alloy on DP600 dual-phase steel with laser welding and resistance spot welding. *Journal of Brazilian Society of Mechanical Science and Engineering*, vol. 42, art. ID 71, **DOI:10.1007/s40430-019-2158-0**.

[24] Pastor, M., Zhao, H., Martukanitz, R.P., Debroy, T. (1999). Porosity, underfill and magnesium loss during continuous-wave Nd:YAG laser welding of thin plates of aluminum alloys 5182 and 5754. *Welding Journal*, vol. 78, p. 207s-216s.

[25] Haboudou, A., Peyre, P., Vannes, A.B., Peix, G. (2003). Reduction of porosity content generated during Nd:YAG laser welding of A356 and AA5083 aluminum alloys. *Materials Science and Engineering A*, vol. 363, no. 1-2, p. 40-52, **DOI:10.1016/S0921-5093(03)00637-3**.

[26] Sun, Z., Ion, J.C. (1995). Laser welding of dissimilar metal combinations. *Journal of Materials Science*, vol. 30, p. 4205-4214, **DOI:10.1007/BF00361499**.

[27] Hoffmann, P., Geiger, Geiger, M. (1995). Recent developments in laser system technology for welding applications. *CIRP Annals*, vol. 44, no. 1, p. 151-156, **DOI:10.1016/S0007-8506(07)62295-1**.

[28] Yang, Z.B., Tao, W., Li, L.Q., Chen, Y.B., Li, F.Z., Zhang, Y.L. (2012). Double-sided laser beam welded T-joints for aluminum aircraft fuselage panels: process, microstructure, and mechanical properties. *Materials Design*, vol. 33, p. 652-658, **DOI:10.1016/j.matdes.2011.07.059**.

[29] Farrokhi, F., Nielsen, S.E., Schmidt, R.H., Pedersen, S.S., Kristiansen, M. (2015). Effect of cut quality on hybrid laser arc welding of thick section steels. *Physics Procedia*, vol. 78, p. 65-73, **DOI:10.1016/j.phpro.2015.11.018**.

[30] Rizzi, P., Bellingeri, S., Massimino, F., Baldissin, D., Battezzati, L. (2009). Microstructures in laser welded high strength steels. *Journal of Physics: Conference Series*, vol. 144, p. 1-4, **DOI:10.1088/1742-6596/144/1/012005**.

[31] Li, W., Ma, L., Peng, P., Jia, Q., Wan, Z., Zhu, Y., Guo, W. (2018). Microstructural evolution and deformation behavior of fiber laser welded QP980 steel joint. *Materials Science Engineering: A*, vol. 717, p. 124-133, **DOI:10.1016/j.msea.2018.01.050**.

[32] Mujica, L., Weber, S., Pinto, H., Thomy, C., Vollertsen, F. (2010). Microstructure and mechanical properties of laser welded joints of TWIP and TRIP steels. *Materials Science Engineering A*, vol. 527, no. 7-8, p. 2071-2078, **DOI:10.1016/j.msea.2009.11.050**.

[33] Atabaki, M.M., Yazdian, N., Ma, J., Kovacevic, R. (2016). High power laser welding of thick steel plates in a horizontal butt joint configuration. *Optics & Laser Technology*, vol. 83, p. 1-12, **DOI:10.1016/j.optlastec.2016.03.016**.

[34] Li, M., Wu, R.H., Cai, S., Chang, Z.D., Wang, Z.H., Chen, J. (2020). Experimental investigation on friction-stir-assisted incremental forming with synchronous bonding of aluminum alloy and steel sheets. *Journal of Materials Engineering and Performance*, vol. 29, p. 750-759, **DOI:10.1007/s11665-020-04600-8**.

[35] Mazar Atabaki, M., Ma, J., Yang, G., Kovacevic, R. (2014). Hybrid laser/arc welding of advanced high strength steel in different butt joint configurations. *Materials Design*, vol. 64, p. 573-587, **DOI:10.1016/j.matdes.2014.08.011**.

[36] Speer, J., Matlock, D. K., Cooman, B.C.D., Schroth, J.G. (2003). Carbon partitioning into austenite after martensite transformation. *Acta Materialia*, vol. 51, no. 9, p. 2611-2622, **DOI:10.1016/S1359-6454(03)00059-4**.

[37] Hajyakbary, F., Sietsma, J., Miyamoto, G., Kamikawa, N., Petrov, R.H., Furuhara, T., Santofimia, M.J. (2016). Analysis of the mechanical behavior of a 0.3C-1.6Si-3.5Mn (wt.%) quenching and partitioning steel. *Materials Science Engineering A*, vol. 677, p. 505-514, **DOI:10.1016/j.msea.2016.09.087.**

[38] Khot Rahul, S., Venkateswara Rao, T. (2020). Effect of quenching media on laser butt welded joint on transformed-induced plasticity (TRIP) steel. *International Journal of Advanced Trends in Computer Science and Engineering*, vol. 9, no. 5, p. 7544-7549, **DOI:10.30534/ijatcse/2020/90952020**.

[39] Khot Rahul, S., Venkateswara Rao, T. (2020). Investigation of mechanical behaviour of laser welded butt joint of transformed induced plasticity (TRIP) steel with effect laser incident angle. *International Journal of Engineering Research and Technology*, vol. 13, no. 11, p. 3398-3403, **DOI:10.37624/IJERT/13.11.2020.3398-3403**.

[40] ASTM International, (2009). *Standard Test Methods for Tension Testing of Metallic Materials*. ASTM International. ASTM E8, p. 1-27.

[41] Khot Rahul, S., Rao, T.V., Keskar, A., Girish, H.N., Madhusudan, P. (2020). Investigation on the effect of power and velocity of laser beam welding on the butt weld joint on TRIP steel. *Journal of Laser Application*, vol. 32, no. 1, art. ID 012016, **DOI:10.2351/1.5133158**.

[42] Santofimia, M.J., Zhao, L., Sietsma, J. (2009). Microstructural evolution of low-carbon steel during application of quenching and partitioning heat treatments after partial austenitization. *Metallurgical and Materials Transaction A*, vol. 40, p. 46, **DOI:10.1007/s11661-008-9701-4**.

[43] Anawa, E.M., Olabi, A.G. (2008). Optimization of tensile strength of ferritic/austenitic laser-welded components. *Optics and Laser in Engineering*, vol. 46, no. 8, p. 571-577, **DOI:10.1016/j.optlaseng.2008.04.014**.

Strojniški vestnik - Journal of Mechanical Engineering 67(2021)1-2, 53-66

DOI:10.5545/sv-jme.2020.6998 Original Scientific Paper
Received for review: 2020-10-19
Received revised form: 2020-12-18
Accepted for publication: 2021-01-13

Dynamic Analysis of Hydraulic Support with Single Clearance

Qingliang Zeng[1,2] – Yangyang Li[1] – Yang Yang[1,*]
[1] Shandong University of Science and Technology, College of Mechanical & Electronic Engineering, China
[2] Shandong Normal University, China

Hydraulic support is a complex parallel mechanism composed of multiple kinematic pairs. In the work of hydraulic support, clearances between kinematic pairs are inevitable, which lead to the deterioration of the support's working performance, and may even affect support's normal work in serious cases. To study the influence of clearances on hydraulic support and simultaneously avoid the mutual interference between different clearances, the normal and tangential force models of kinematic pairs with clearance are established, based on the Lankarani-Nikravesh contact force model and the Coulomb friction model. Furthermore, the dynamic model of the hydraulic support with single clearance is established by adding a clearance between the rear link and base and, according to the dynamic model of the hydraulic support, the research about the influence of clearance on the movement and force of hydraulic support is carried out, which proves the need to study the clearance of hydraulic support. Moreover, the influence of clearance, clearance size, and different oil inlet drive modes of front and rear columns on the stability of hydraulic support are analysed, and then the change of hydraulic support posture caused by clearance and clearance size is considered. The results show that clearance causes the movement and force of the rear link to fluctuate, which affects the stability of the hydraulic support. The clearance size affects the fluctuation degree of the movement and force, which is an important factor in the instability of hydraulic support. Also, the hydraulic support posture is changed by the clearance and clearance size. Different column oil inlet drive modes have different impacts on the clearance and have different effects on the stability of hydraulic support.
Keywords: dynamic analysis, kinematic pair clearance, clearance size, hydraulic support posture

Highlights
- *Taking the hydraulic support as the research subject, the dynamic analysis of the hydraulic support with clearance between the rear link and the base is carried out based on the Lankarani-Nikravesh model.*
- *The dynamic performance of hydraulic support with clearance and without clearance has been compared, proving the necessity of research on hydraulic support clearance.*
- *The dynamic performance of hydraulic support with clearance under different clearance size and oil inlet drive mode has been compared, and the influence of clearance size and oil inlet drive mode on hydraulic support has been analysed.*
- *The influence of clearance and clearance size on the posture of hydraulic support has been studied, and the influence of posture on the working performance of hydraulic support has been analysed.*

0 INTRODUCTION

As important supporting equipment in coal mining, hydraulic support has always been a research hotspot in the coal industry worldwide. With the introduction of the concept of intelligent mining, hydraulic support has begen to develop in the direction of intelligent posture monitoring [1], intelligent working face perception [2] and [3], intelligent control [4] and [5], etc. Moreover, support adaptability analysis [6] and load-bearing strength analysis [7] based on experimental verification and virtual simulation also tend to the working conditions, and the analysis and research of the new hydraulic support have also made progress [8]. As an inevitable component in the production process of hydraulic support, the impact of clearance on the working performance of hydraulic support is difficult to eliminate. Therefore, it is essential to study the influence of clearance on hydraulic support for improving the working performance and the stability of the hydraulic support. However, the research on the dynamic analysis of the hydraulic support with clearance is scarce at present, and it is urgent that it be carried out.

The key point of the dynamic analysis of mechanism with clearance is the model of the establishing contact force. At present, according to the different descriptions of the state between shaft and bearing, three kinds of contact force models are proposed: the continuous contact model, the two-state model, and the three-state model. Based on the contact force models, many research studies have been carried out by domestic and foreign scholars. Flores [9] and Flores et al. [10] studied the crank and analysed the influence of revolute pair with clearance on crank slider through numerical analysis and experiment. Li et al. [11] established a dynamic model of the spring operating mechanism based on the continuous contact model and obtained the influence of clearance on the movement state through a numerical solution. Pereira et al. [12] studied the influence of spherical and cylindrical contact force models on the crank slider

*Corr. Author's Address: Shandong University of Science and Technology, College of Mechanical & Electronic Engineering, Qingdao, China, yang.yang@sdust.edu.cn

revolute pairs, which further improved the validity of the modelling of the revolute pairs. Li et al. [13] established a dynamic model of a connecting rod with clearance between pairs based on the two-state model and analysed the influence of different factors on the movement and force of the mechanism. Li et al. [14] established the kinematics and dynamics model of the 5-prismatic–spherical–spherical/universal-prismatic-universal (5-PSS/UPU) parallel mechanism with spherical pair clearance through the two-state model, and analysed the impact of clearance size on the dynamic performance of the system. Erkaya [15[and [16] used the nonlinear spring damping model to conduct kinematics and dynamics analysis on the welding robot with clearance, and studied the impact of clearance on the movement error, vibration, and force of the welding robot. Bai et al. [17] established a new contact force model of planar linkage mechanism, and proposed a kinematics and dynamics optimization scheme of linkage structure to reduce the vibration peak caused by clearance. Wang et al. [18] and [19] proposed an improved normal contact force model and modified Coulomb friction model and took the crank slider and four-bar linkage mechanism as research objects to analyse the impact of clearance on the dynamic characteristics of the mechanism. Matekar and Fulambarkar [20] established a crank slider simulation model without clearance or adjustable clearance by Adams, analysed the impact of clearance on the slider displacement, and verified the simulation results through experimental devices. Tajaril et al. [21] established the mathematical model of the mechanical system by adding spherical clearance to a hexapod robot, obtained the impact of clearance on the position accuracy of the robot and verified the results through experiments. Xu et al. [22] studied the influence of clearance on the positional accuracy of the SCARA robot by establishing joint clearance model and experimental verification and analysed the determinants of clearance error. Gu et al. [23] carried out a dynamic analysis on the space manipulator with clearance based on Lankarani-Nikravesh contact force model and obtained the influence of clearance on the output results of the manipulator. Huang et al. [24] considered both the clearance and flexibility of the mechanism, and established the dynamic model of the 3-revolute-revolute-revolute (3-RRR) parallel mechanism by Adams to analyse the influence of different clearance on the displacement and velocity of the mechanism. Hou et al. [25] established a flexible 3-revolute-spherical-revolute (3-RSR) parallel mechanism simulation model based on Adams, and discussed the dynamic characteristics of the system under different clearance types. Zhang and Zhang [26] proposed that a redundant drive 4-RRR mechanism could effectively control the joint clearance through kinematics and dynamics analysis of the 3-degree of freedom (3-DOF) redundant drive 4-RRR mechanism. Erkaya [27] established a dynamic simulation model and experimental device of the spatial slider-crank mechanism system with clearance, and obtained the influence of clearance size and driving speed on the vibration response of the system. Based on an experimental device, Erkaya

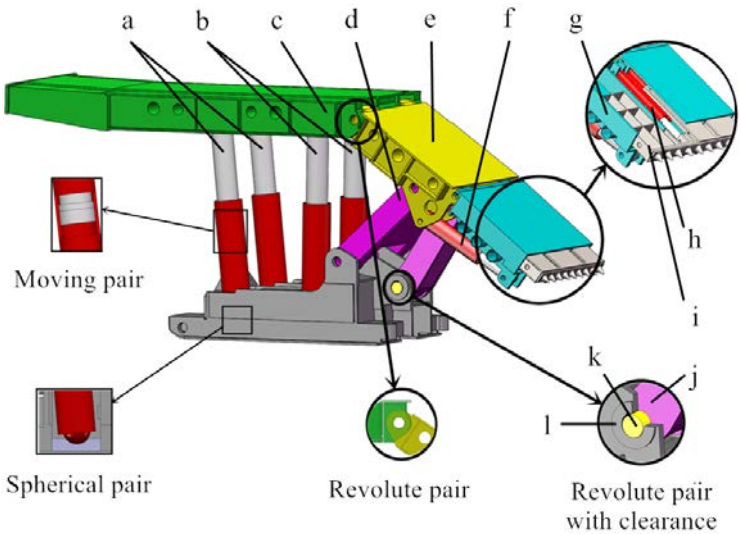

Fig. 1. *Structure of four columns hydraulic support for top coal caving; a) front columns, b) rear column, c) top beam, d) front linkage, e) shield beam, f) tail beam jack, g) tail beam, h) plug plate jack, i) plug plate, j) rear linkage, k) shaft, and l) base*

[28] analysed the influence of clearance on the current fluctuation and power consumption of the system actuator, and designed a neural predictor to predict and evaluate the current. Chen et al. [29] established the planar model of hydraulic rock-breaker with multi clearance based on the Lankarani-Nikravesh model and Lagrange multiplier method, analysed the dynamic response of hydraulic rock-breaker and studied the influence of clearance size, friction and other factors on the dynamic characteristics of hydraulic rock-breaker. Tian et al. [30] compared and analysed the planar and spatial modelling methods of mechanical system with clearances, introduced the modelling methods of different types of dry and lubrication clearances, and summarized the previous clearance analysis and experiments. Edler et al. [31] developed a one-dimensional (1-D) simulation model of the progressive flow control and used in hydrostatic bearing to obtain a constant bearing clearance.

Previous studies mainly focus on the analysis of clearance, and the research object is mostly simple linkage mechanism, and research on construction machinery is less common. This paper will take the hydraulic support in coal mining as the research object, combined with the actual working situation, analyse the influence of the clearance on the working performance of the hydraulic support, and provide a new direction for further improving the working performance of the hydraulic support.

Hydraulic support is a complex parallel mechanism containing spherical pair, moving pair and revolute pair. In practical work, the normal operation of hydraulic support is restricted due to the unavoidable clearances. Fig. 1 is the structure diagram of the hydraulic support. It can be seen that the positions of support kinematic pair are different, as are the clearance forms of different kinematic pairs. Moreover, the kinematic pairs with clearance affect each other.

If all the clearances of hydraulic support are considered at the same time, it is difficult to describe the influence of each clearance accurately. Therefore, the research of hydraulic support with clearance should start from the single clearance, and the selection of the clearance position is also very important for the research. As a parallel mechanism driven by oil cylinder, the hydraulic support controls the movement of the top beam through the front columns and rear columns, and controls the movement of the tail beam and the plug plate through the tail beam jack and the plug plate jack. The four-bar linkage mechanism composed of front and rear linkages, shield beam and base, which simultaneously affect the position change of top beam, tail beam and plug plate, which is the key to control the movement of the hydraulic support. Moreover, the rear linkage is the only single connected part containing the clearance of revolute pair in the hydraulic support, and it is an important part for the hydraulic support to bear the load. Therefore, the clearance between the rear linkage and the base is the best position to study the influence of single clearance on the hydraulic support. By establishing the dynamic model of hydraulic support with clearance between the rear linkage and base, this paper will discuss the influence of single clearance on the movement and force of hydraulic support, so as to provide theoretical and research basis for the subsequent research work of hydraulic support with clearance.

1 MODELLING OF HYDRAULIC SUPPORT WITH SINGLE CLEARANCE

1.1 The State Model at Single Clearance

The key point of analysing the mechanism with clearance is the establishment of a contact force model. In order to establish the contact force model between the rear linkage and base, the contact state of bearing and shaft should be described first. Fig. 2 is a simplified model of the clearance between the rear linkage and the base. In the ideal situation, the centre of shaft and bearing are in the same position; however, due to the existence of clearance, there is an eccentric distance between the shaft and the bearing in practical work. In the figure, O_1 and O_2 are the centre of the shaft and the bearing, respectively, and their radii are R_1 and R_2, so the clearance radius of shaft and bearing can be expressed as follows:

$$c = R_2 - R_1. \tag{1}$$

Under the fixed coordinate system O-XY, the position vectors of O_1 and O_2 are $\mathbf{r}_1$ and $\mathbf{r}_2$ respectively, then the offset vector between shaft and bearing can be expressed as:

$$\mathbf{e} = \mathbf{r}_2 - \mathbf{r}_1. \tag{2}$$

In addition, the offset distance between the shaft and bearing can be expressed as the norm of the offset vector, so the penetration depth between the shaft and bearing can be expressed as:

$$\delta = e - c. \tag{3}$$

According to Eq. (3), the movement state of shaft and bearing can be expressed by δ, when $\delta > 0$, the shaft and bearing are in collision state, and

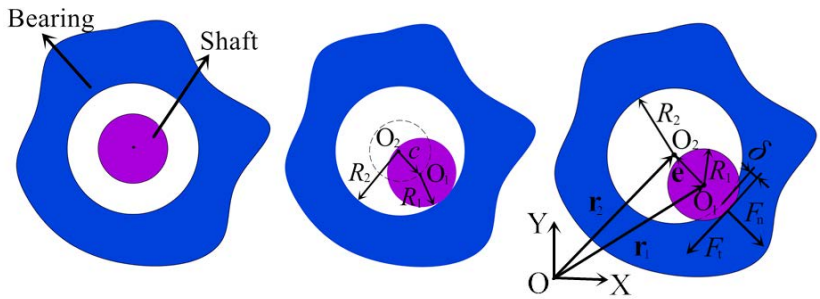

Fig. 2. *Clearance simplification model of revolute pairs*

the penetration depth is δ; When $\delta = 0$, the shaft and bearing are in a state of contact or separation. When $\delta < 0$, the shaft and bearing are in a separate state; they both move freely without contact.

1.2 Clearance Contact Force Model

Contact force will be generated during the collision between shaft and bearing and can be simply decomposed into normal force and tangential force. The direction of the normal force is the normal direction of the contact surface, mainly the normal collision force between the shaft and bearing, while the tangential force is the tangent direction of the contact surface, mainly the tangential friction between the shaft and bearing.

After years of research, various researchers have proposed various models of normal contact force based on Hertz contact models. The Lankarani-Nikravesh contact force model takes into account the energy dissipation in the collision process and becomes a widely used nonlinear spring damping model in clearance research. According to the Lankarani-Nikravesh contact force model, the normal contact force F_n in the contact process can be expressed as:

$$F_n = K\delta^n + Dv. \tag{4}$$

In Eq. (4), δ is the penetration depth between shaft and bearing; n is the force index, and $n = 1.5$ for the contact between metals; D is the damping coefficient of contact process; v is the normal collision speed between shaft and bearing; K is the stiffness coefficient of the contact process, and its equation is [32]:

$$K = \frac{4}{3\pi\left(h_1 + h_2\right)}\sqrt{\frac{R_1R_2}{R_1 + R_2}}, \tag{5}$$

$$h_i = \frac{1-u_i^2}{\pi E_i}, \quad i = 1,2. \tag{6}$$

In Eq. (5), h_1 and h_2 are the material coefficients of the contact object and the equation is Eq. (6), u_1 and u_2 are Poisson's ratio of the contact material, E_1 and E_2 are the elastic modulus of the contact material.

According to the different forms of friction, the tangential contact force model can be divided into a dry friction model and a lubrication friction model. The friction between the rear linkage and base belongs to dry friction, and the dry friction is generally modelled by the Coulomb friction model or the nonlinear friction model developed by domestic and foreign scholars. The nonlinear friction model proposed by Ambrósio based on the improvement of the Coulomb friction model is widely used, and its expression is as follows:

$$F_t = -\mu_d c_d F_n \mathbf{t}. \tag{7}$$

In Eq. (7), μ_d is the sliding friction coefficient; F_n is the normal contact force; v_T is the tangential relative velocity between the shaft and bearing; $\mathbf{t}$ is the direction of tangential contact force; c_d is the dynamic correction coefficient, which is expressed as:

$$c_d = \begin{cases} 0 & v_T \le v_s \\ \dfrac{v_T - v_s}{v_d - v_s} & v_s < v_T < v_d \\ 1 & v_T \ge v_d \end{cases}. \tag{8}$$

In Eq. (8), v_s and v_d are specific velocity limit values.

2 DYNAMIC ANALYSIS OF HYDRAULIC SUPPORT WITH SINGLE CLEARANCE

The key to the dynamic analysis of the hydraulic support with clearance between the rear linkage and base is to establish the clearance contact force model and simulate the hydraulic support model. The contact force model of the single clearance between the rear linkage and base can be described by the Lancarani-

Nikravesh contact force model and the developed nonlinear friction model. To simulate the contact force model between the shaft and bearing more realistically, the material of each part of the hydraulic support and the shaft should be defined. Here, the components of the hydraulic support are defined as steel material, and the material of shaft is 35CrMo, their material properties are shown in Table 1.

Table 1. *Material properties of hydraulic support and shaft*

Material	Density [kg×mm^{-3}]	Elastic modulus [MPa]	Poisso's ratio
Steel	7.801×10^{-6}	2.07×10^{5}	0.29
35CrMo	7.850×10^{-6}	2.06×10^{5}	0.3

Each part of hydraulic support is affected by the clearance between the rear linkage and base. This paper focuses on the influence of the clearance on the working performance of the hydraulic support during its rising process. To simulate the rising action of hydraulic support, the driving of front and rear columns is established based on step function, the tail beam jack is kept still, and the influence of plug plate and plug plate jack are ignored. Through the above driving and clearance contact force model, the dynamic models of the hydraulic support with single clearance between the rear linkage and base are analysed.

3 ANALYSIS OF THE INFLUENCE OF CLEARANCE ON HYDRAULIC SUPPORT

Combined with the previous research results on clearance, it can be seen that the existence of clearance will cause the performance of mechanical systems to decline. However, due to the lack of relevant research, the influence of the clearance between the rear linkage and base on the hydraulic support remains uncertain. Therefore, this section analyses how the existence

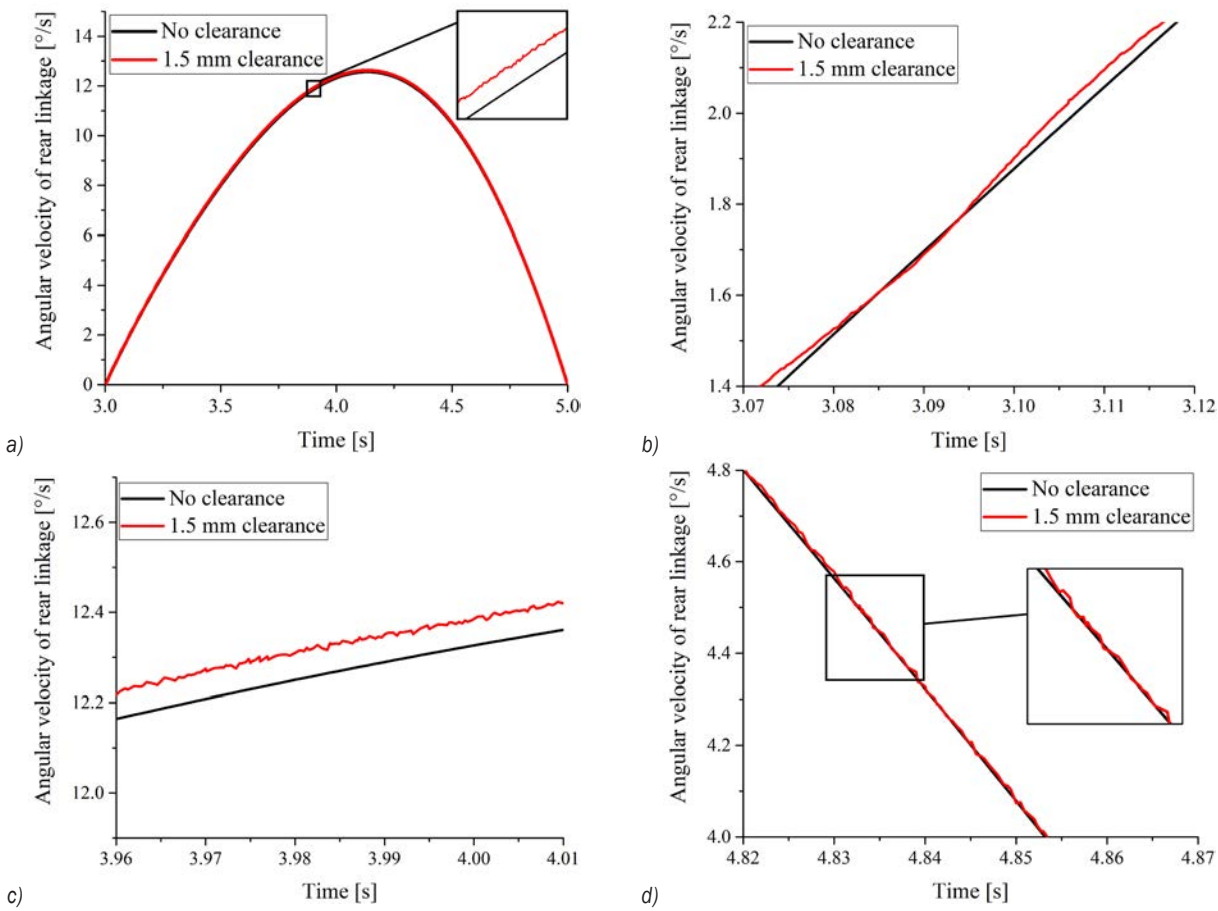

Fig. 3. *Dynamic performance of rear linkage with 1.5 mm clearance and without clearance: a) overall angular velocities of rear linkage, b) local enlarged curves of angular velocities in early stage, c) local enlarged curves of angular velocities in the middle stage, and d) local enlarged curves of angular velocities in later stage*

of clearance affects the movement and force of the hydraulic support. When there is a 1.5 mm clearance between the rear linkage and base, the movement and force of the rear linkage is compared with that without clearance, so as to study the influence of the clearance on the working performance of the hydraulic support.

Before the analysis of the hydraulic support with 1.5 mm clearance or without clearance, the stiffness coefficient of the contact between the bearing and shaft should be calculated. According to Eq. (5) and the material properties of shaft and bearing, the stiffness coefficient of shaft and bearing is 857942.947 when the clearance is 1.5 mm. Based on the stiffness coefficient, the dynamic model of the hydraulic support with 1.5 mm clearance and the dynamic model of the hydraulic support without clearance are analysed. The movement and force variation curves of the rear linkage are shown in Fig. 3. Fig. 3a shows the angular velocity curve of the rear linkage when there is no clearance and when there is a 1.5 mm clearance between the rear linkage and base. It can be seen from the figure that the angular velocities of the rear linkage in the two cases change in the same trend, and the angular velocity curve is very similar, but there are still some differences in the local curve. Fig. 3b to d shows the local enlarged view of the angular velocity curve of the rear linkage in different periods during the movement process. It can be seen that compared with the angular velocity of the rear linkage without clearance, the angular velocity of the rear linkage fluctuates when there is a 1.5 mm clearance between the rear linkage and base, and the angular velocity of the middle stage of the rear linkage with 1.5 mm clearance is higher than that without clearance.

Fig. 4 shows the angular acceleration curve of the rear linkage when there is no clearance and when there is a 1.5 mm clearance between the rear linkage and base. It can be seen from the figure that the angular acceleration of the rear linkage has a great fluctuation when there is a 1.5 mm clearance between the rear linkage and base, but the change trends of the angular acceleration curve in two cases are the same. Therefore, although the clearance does not change the movement trend of the hydraulic support, it will make the movement of the hydraulic support fluctuate, resulting in the decrease of the stability during the movement of hydraulic support. Fig. 5 shows the contact force curve of the rear linkage when there is no clearance and when there is a 1.5mm clearance between the rear linkage and base. This is the same as the difference of angular velocity and angular acceleration curve of the rear linkage, when there is a clearance between the rear linkage and base, the contact force at the rear linkage fluctuates greatly, but the variation trend of the contact force is the same as that without clearance. Therefore, the existence of clearance will lead to the fluctuation of contact force between the rear linkage and base during hydraulic support movement, which will seriously affect the working stability of hydraulic support and reduce the working performance of hydraulic support.

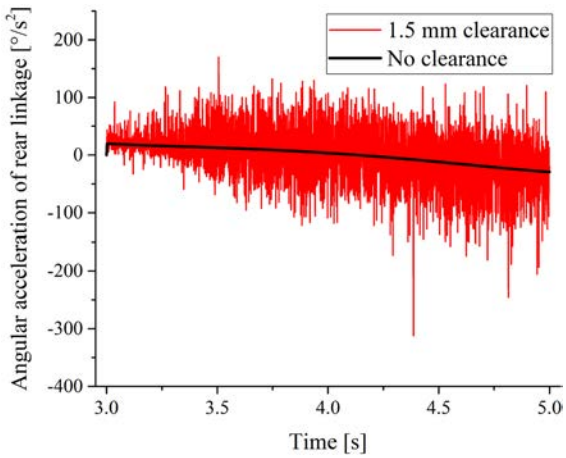

Fig. 4. *Angular accelerations of rear linkage with clearance and without clearance*

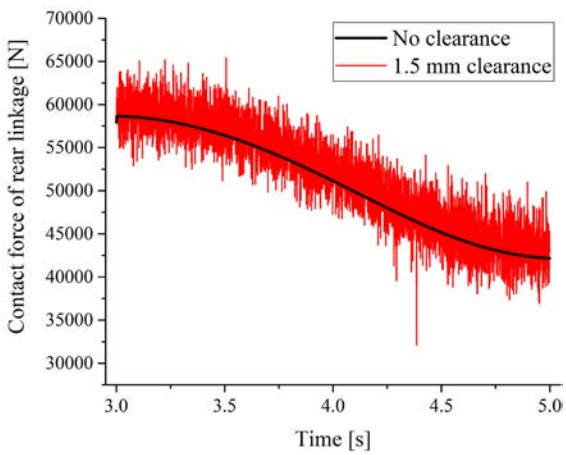

Fig. 5. *Contact forces of rear linkage with clearance and without clearance*

By comparing the dynamic performance of the rear linkage with and without clearance, it can be seen that the clearance has little influence on the overall change trend of the hydraulic support, but will lead to the fluctuation of the movement and force, aggravate the instability of the hydraulic support, and do great harm to the normal work of the support. Therefore, research on the clearance is very important for improving the working performance and the safety of the hydraulic support.

4 ANALYSIS OF THE INFLUENCE OF CLEARANCE SIZE ON HYDRAULIC SUPPORT

Through the dynamic comparative analysis of the hydraulic support with clearance or without clearance, it can be seen that the clearance affects the stability of the hydraulic support, leading to the decline of the working performance of the hydraulic support. In order to study the influence of clearance size on the hydraulic support, the dynamic models of hydraulic support with different clearance sizes between the rear linkage and base are established. The clearance dimensions of the rear linkage are taken as 0.5 mm, 1.0 mm, 1.5 mm and 2.0 mm. According to Eq. (5), the stiffness coefficients of shaft and bearing are calculated, as shown in Table 2. Based on the stiffness coefficient of different clearance sizes, the dynamic analysis of hydraulic support with different clearance sizes between the rear linkage and base are carried out, and the influence of clearance size on the movement, force and posture of the hydraulic support is studied.

Table 2. *Stiffness coefficient of different clearance*

Clearance radius [mm]	Shaft radius [mm]	Stiffness coefficient
0.5	65.0	861300.557
1.0	64.5	859629.849
1.5	64.0	857942.947
2.0	63.5	856239.607

4.1 The Influence of Clearance Size on the Movement of Hydraulic Support

To study the influence of clearance size on the movement of hydraulic support, the angular velocity and angular acceleration curves of the rear linkage

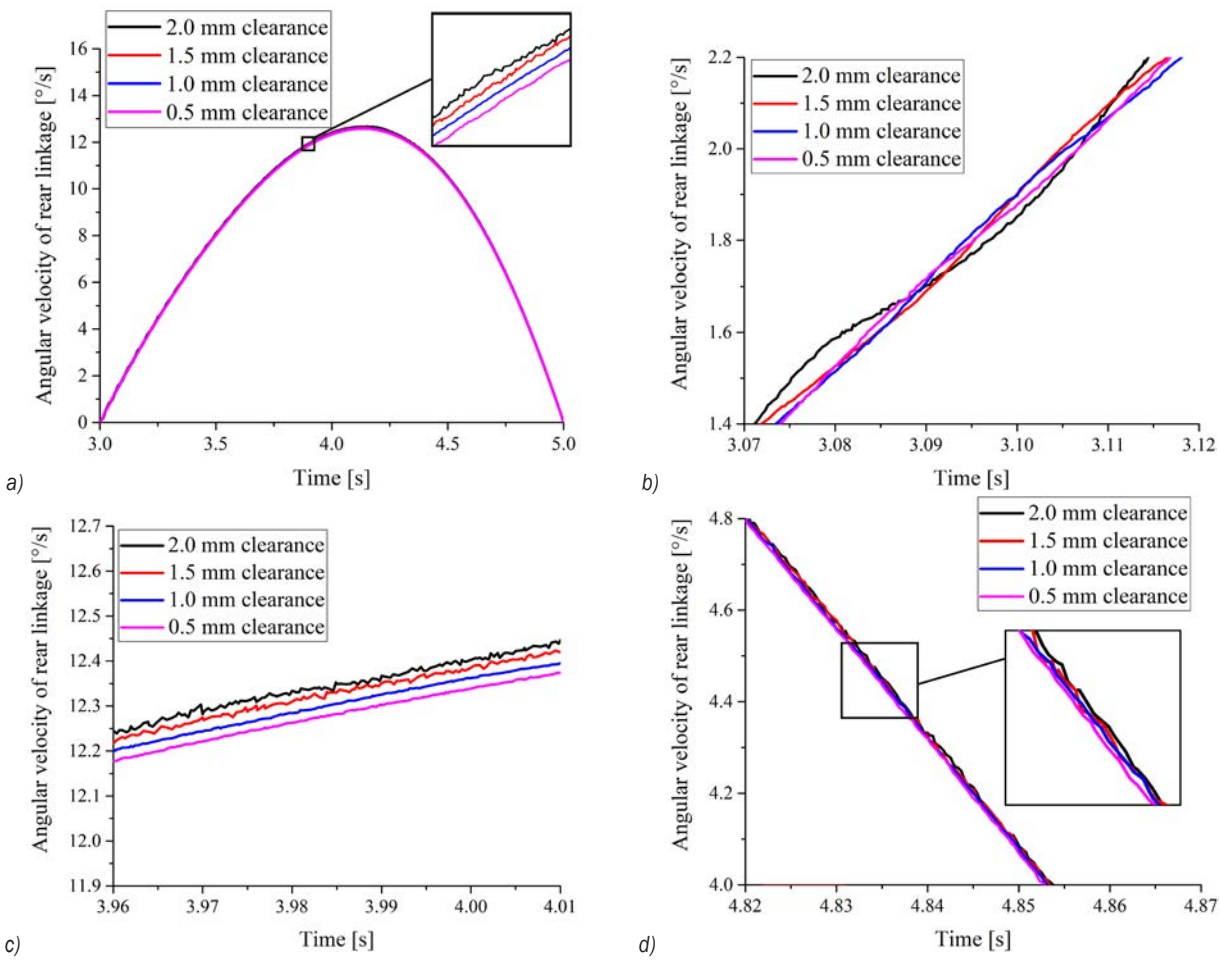

Fig. 6. *Angular velocities of rear linkage with different clearance size; a) overall angular velocities of rear linkage; b) local enlarged curves of angular velocities in early stage; c) local enlarged curves of angular velocities in the middle stage; and d) Local enlarged curves of angular velocities in later stage*

with different clearance sizes were compared. In Fig. 6a, the angular velocity of the rear linkage changes with different clearance sizes. It can be seen from the figure that the angular velocity of the rear linkage changes with time in different clearance sizes with the same trend, and clearance size has little effect on angular velocity, the angular velocity curves of the rear linkage in each situation are very similar. To analyse the impact of clearance size on the angular velocity of the rear linkage specifically, the local enlarged view of the angular velocity curves in different periods was taken for comparison. As shown in Fig. 6b to d, the angular velocities of the rear linkage with different clearance sizes in the early and late stage are similar. However, the degree of angular velocity fluctuations is different, and the larger the clearance size is, the greater the fluctuation of angular velocity is. The numerical value and fluctuation of the angular velocity of rear linkage are different in the middle stage with different clearance sizes. The larger the clearance is, the larger the numerical value of angular velocity in the middle stage and the larger the fluctuation of angular velocity are.

Fig. 7 shows the angular acceleration curves of the rear linkage with different clearance sizes. It can be seen from the figure that the angular accelerations with different clearance sizes change with the same trend over time, but the fluctuation degree of angular accelerations is different, the fluctuations of the angular acceleration with the clearance of 2.0 mm and 1.5 mm are much greater than that with the clearance of 1.0 mm and 0.5 mm. To further analyse the influence of clearance size on the angular acceleration of the rear linkage, the average angular acceleration values during the rising process of hydraulic supports with different clearance sizes were compared. The average angular acceleration values of 2.0 mm clearance was –0.3219 °/s², 1.5 mm was –0.2733 °/s², 1.0 mm was –0.0515 °/s², and 0.5mm was 0.0030 °/s² respectively. By comparing the average angular acceleration of

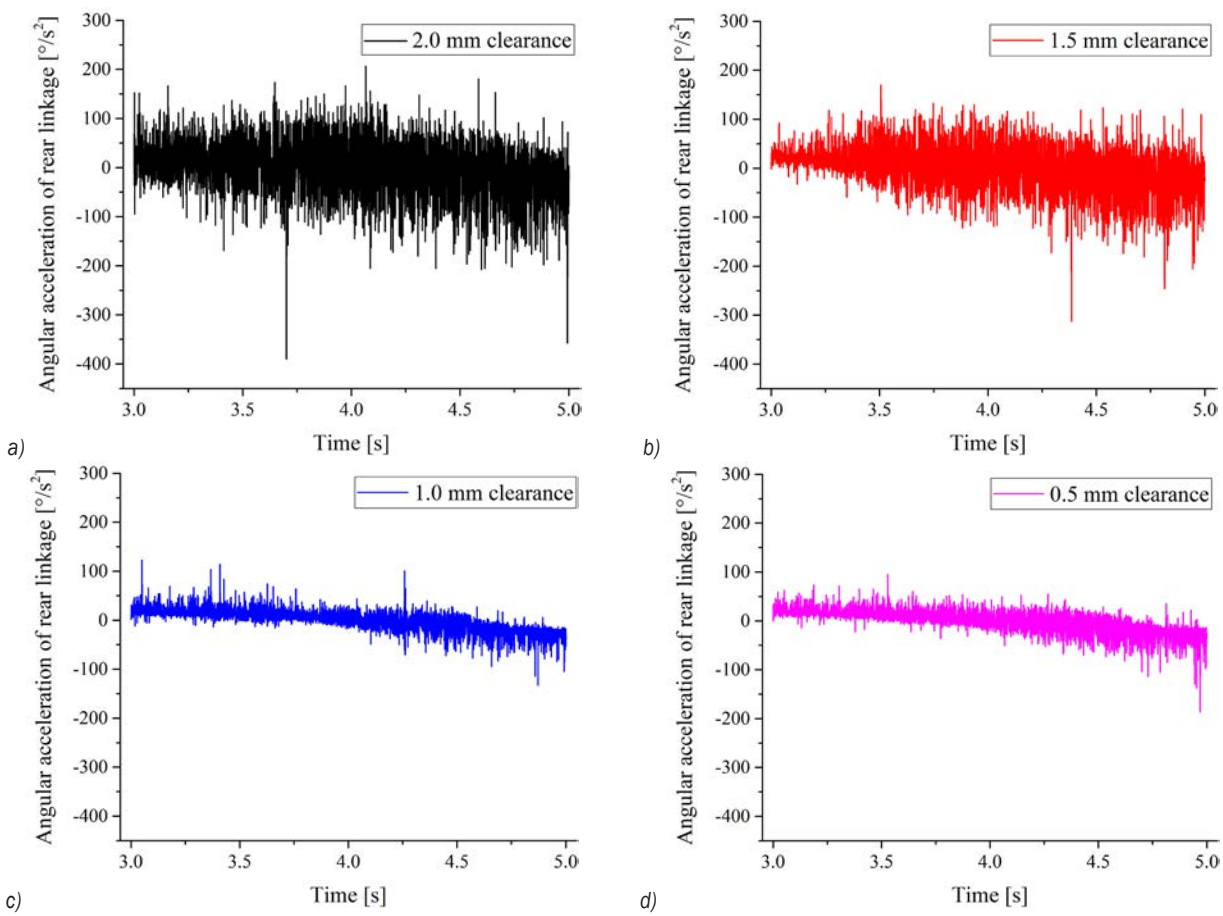

Fig. 7. *Angular accelerations of rear linkage with different clearance sizes; a) 2.0 mm clearance, b) 1.5 mm clearance, c) 1.0 mm clearance, and d) 0.5 mm clearance*

the rear linkage, it can be seen that the clearance size has little influence on the numerical value of angular acceleration, and the overall movement trend of the hydraulic support is basically unchanged.

The hydraulic supports with different clearance size have the same movement trend in Figs. 6 and 7. However, the clearance size between the rear linkage and base makes the angular velocity and angular acceleration of the rear linkage fluctuate differently. The larger the clearance size is, the greater the fluctuation degree of the rear linkage movement is, and the greater the impact on the stability of the hydraulic support is, the greater the harm will be caused. It can be seen that the clearance size is an important factor affecting the movement fluctuation of the hydraulic support, so a reasonable clearance size is very important to improve the working performance of the support and reduce the operation accidents of the support.

4.2 The Influence of Clearance Size on the Force of Hydraulic Support

To analyse the influence of the clearance size on the force of the hydraulic support, the contact forces of the rear linkage with different clearance sizes during the rising process of the hydraulic support were analysed. It can be seen from Fig. 8 that the variation trends of the contact force of the rear linkage with different clearance sizes are the same, but the fluctuations of the contact force are different. To accurately analyse the contact force of the rear linkage with different clearance sizes, the average values of the contact force in each case are taken for comparison, so as to judge the influence of the clearance size on the contact force value; the standard deviations of the contact force in each case are taken for comparison, so as to judge the influence of the clearance size on the fluctuation degree of the contact force. The mean and standard

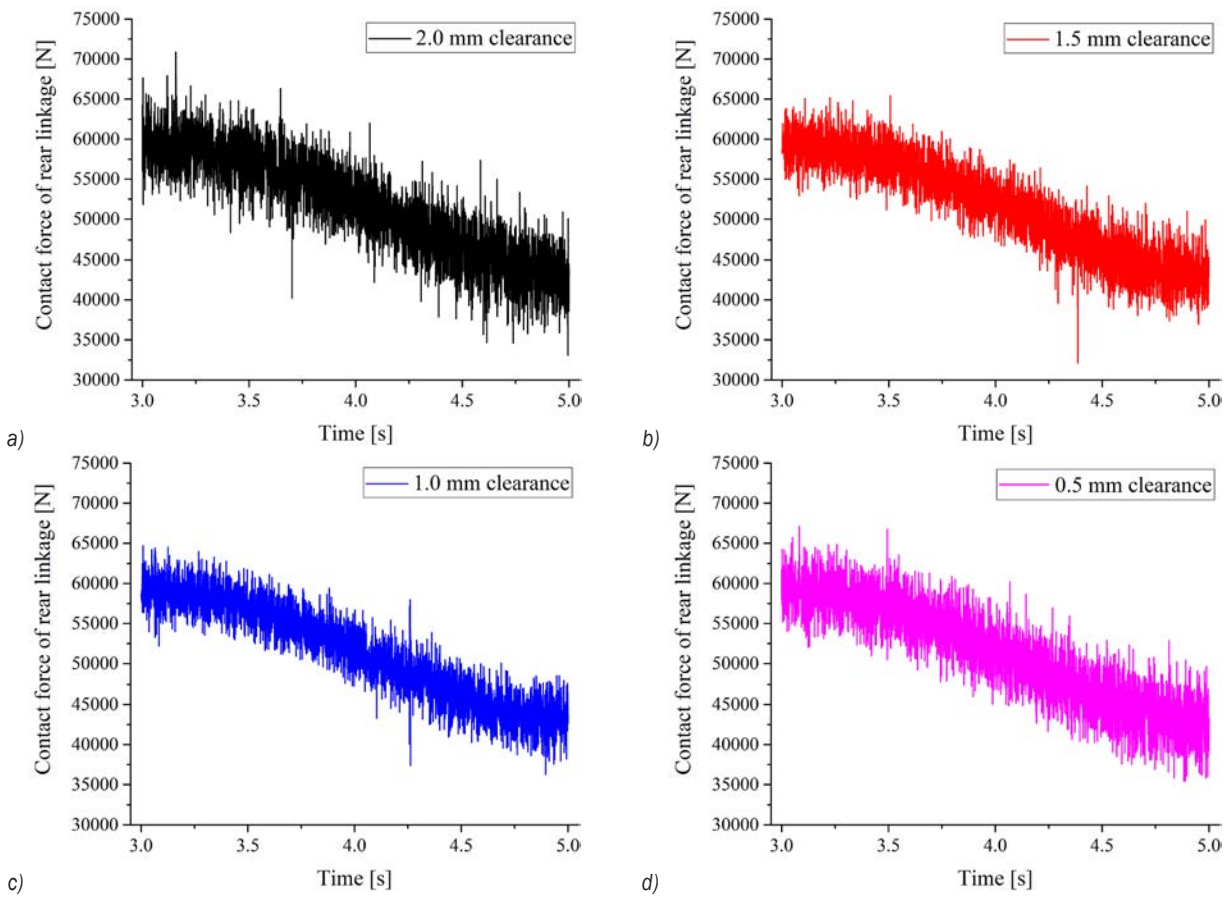

Fig. 8. *Contact forces of rear linkage with different clearance sizes; a) 2.0 mm clearance; b) 1.5 mm clearance; c) 1.0 mm clearance; d) 0.5 mm clearance*

deviations of the contact force of the rear linkage are shown in Table 3.

Table 3. *Average and standard deviation of contact force under different clearance sizes*

Clearance radius [mm]	Average of contact force [N]	Standard deviation of contact force [N]
0.500	51375.609	6114.940
1.000	51491.566	5938.103
1.500	51649.027	6013.112
2.000	51795.195	6188.895

The data in Table 3 show that the average of contact force of rear linkage increases with the increase of clearance size, but the increase in the average is small. The standard deviation of the contact force is also related to the clearance size. The standard deviation of contact force decreases at first and then increases with different clearance sizes. It can be seen from the change of the mean value and standard deviation that the clearance size has an influence on the force of hydraulic support, but the influence is relatively small, and the clearance size also affects the fluctuation degree of contact force, but the fluctuation of contact force does not decrease with the decrease of clearance size. Therefore, the clearance size also has an impact on the stability of the hydraulic support force, which will affect the working performance of the hydraulic support.

4.3 The Influence of Clearance on the Posture of Hydraulic Support

The rear linkage, as a part of the hydraulic support four-connecting-rod structure, has an important influence on the posture of the hydraulic support. To analyse the impact of clearance on the posture of hydraulic support, this section selects the movement trajectory of the endpoint of the top beam when there is no clearance and when there are different clearance sizes, obtains the impact of different clearances on the end distance between roof bar end and coal wall. It can be seen from Figs. 9 and 10 that the existence of the clearance changes the movement state of the four-bar structure of the hydraulic support, which causes the movement trajectory of the endpoint of the top beam to shift in the direction of the rear linkage during support's rising process.

Moreover, the larger the clearance size, the larger the distance of the movement trajectory of the rear linkage. In addition, it can be seen from the figure that the movement range of the end point of the top beam is similar in the horizontal direction when there is no clearance and when the clearance sizes are different. Therefore, the clearance and clearance size will increase the distance of the top beam end point, which reduces the stability of the support, but it has little influence on the horizontal movement range of the top beam.

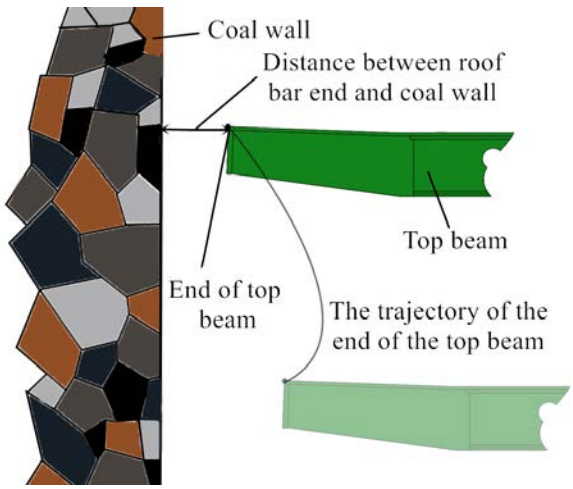

Fig. 9. *Position and movement trajectory of end point*

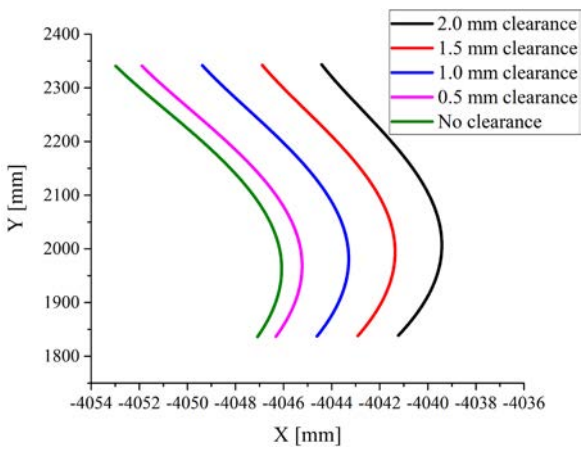

Fig. 10. *Change of end point with different clearances*

The front and rear columns are the main driving force source of the hydraulic support. The posture variation of the front and rear columns will have a great impact on the working performance of the hydraulic support. Therefore, the angles of the front and rear columns are defined in Fig. 12, and the variation of the angle of the front and rear columns when there is no clearance and when the clearance sizes are different are shown in Fig. 11. It can be seen from Fig. 11 that the front and rear columns deflect to the rear linkage for their horizontal angles decreasing, and the larger the clearance size is, the smaller the horizontal angles of the front and rear columns are.

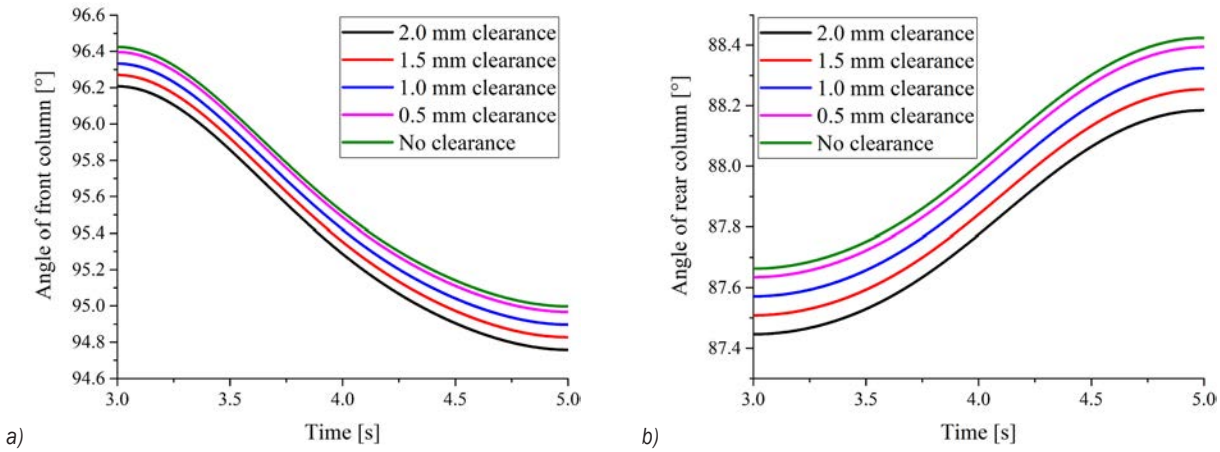

Fig. 11. *Angle change of columns with different clearances; a) angle change of front column; and b) angle change of rear column*

Although the deflection direction of the front and rear columns is the same, the effects on the front and rear columns are completely opposite, the clearance makes the front column tend to the vertical direction, which enhances its supporting capacity, and the clearance causes the rear column to deviate from the vertical direction, which decreases the support capacity of the rear column. Compared with the former results, the clearance not only changes the posture of the hydraulic support, but also affects the force situation of the hydraulic support and the difference of posture increases with the clearance size.

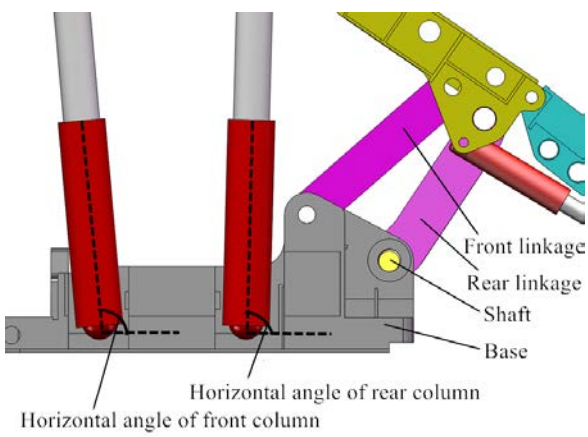

Fig. 12. *Horizontal angle of front and rear columns*

5 THE INFLUENCE OF THE OIL INLET DRIVE MODE ON HYDRAULIC SUPPORT WITH SINGLE CLEARANCE

Impact is one of the most serious factors affecting clearance. During the movement of hydraulic support, different oil inlet drive modes have different impacts on hydraulic support, and the existence of the clearance makes the impacts on hydraulic support more obvious. To study the influence of different oil inlet drive modes on the hydraulic support with clearance between the rear linkage and base, two different oil inlet drive modes are adopted for dynamic models. Fig. 13a shows the displacement curves of the front and rear columns of the hydraulic support in two oil inlet drive modes. In the figure, the oil inlet drive mode 1 is the uniform oil inlet drive model, the front and rear columns move directly at a speed from stationary without transition, which belongs to the direct oil inlet drive mode with impact, and oil inlet drive mode 2, which established by step function, makes the extension displacement of front and rear columns change smoothly with gently variable speed. Step function is a common description of the driver, and the expression of oil inlet drive mode 2 is STEP(TIME,0,0,3,0) + STEP(TIME,3,0,5,500).

6 CONCLUSIONS

The dynamic analysis of the hydraulic support with clearance between the rear linkage and base was carried out based on the Lancarani-Nikravesh contact force model. The dynamic performance of the rear linkage of hydraulic support with and without clearance was compared. The movement and force changes of hydraulic support with different clearance size and oil inlet drive mode were analysed, and the influence of clearance and clearance size on the posture of hydraulic support was studied. Comparing the dynamic characteristics of hydraulic support under different factors, the main results are as follows:

(1) Clearance is an important factor affecting the stability of hydraulic support. Compared with the hydraulic support without clearance, the existence

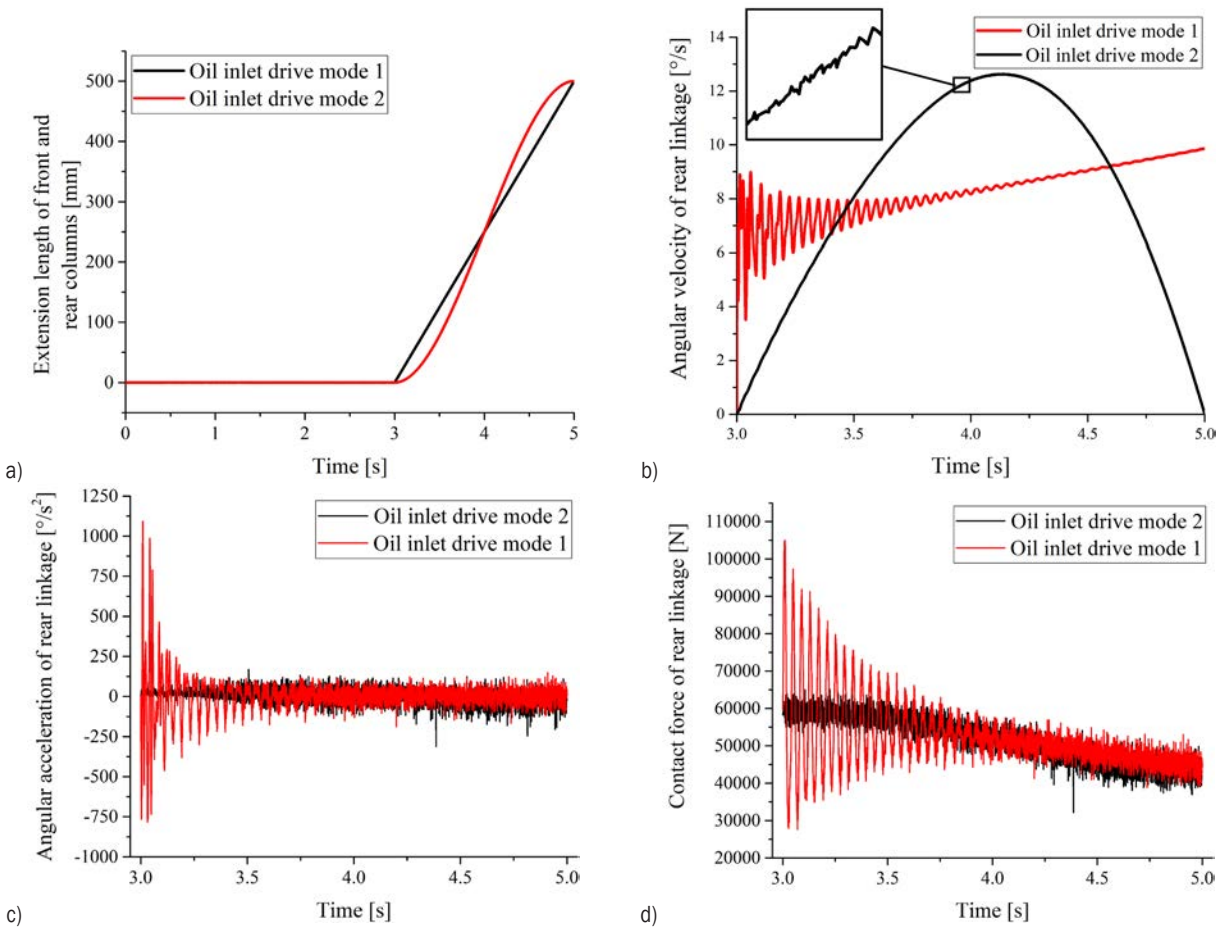

Fig. 13. *Dynamic performance of rear linkage during different oil inlet drive modes; a) displacements of front and rear columns during different oil inlet drive modes; b) angular velocities of rear linkage; c) angular accelerations of rear linkage; and d) contact forces of rear linkage*

of clearance makes the movement and force of the hydraulic support fluctuate, which reduces the working stability of the hydraulic support.

(2) Clearance size is an important point when studying the influence of clearance on hydraulic support. The clearance size changes the movement and force fluctuation of hydraulic support. The reasonable clearance size can improve the stability of hydraulic support.

(3) Different oil inlet drive modes have different responses to hydraulic supports with clearance. A smooth oil inlet drive mode can reduce the fluctuation caused by clearance; otherwise, it will affect the stable operation of hydraulic support.

(4) The clearance changes the posture of the hydraulic support. The clearance between the rear linkage and base changes the posture of the driving columns and changes the working performance of the columns.

To summarize, the clearance and clearance size affect the movement and force of the hydraulic support, change the posture of the support, and the response of clearance to different oil inlet drive modes is very different, which reduces the stability of the hydraulic support, and even affects the normal work of hydraulic support. Therefore, the clearance is an important part of the analysis of hydraulic support, which is of great significance to the further study of hydraulic support.

7 ACKNOWLEDGEMENTS

This work was supported by National Natural Science Foundation of China (Grant No. 51974170) and Special Funds for Climbing Project of Taishan Scholars. Shandong University of Science and Technology and Shandong Normal University

contributed to the work equally and should be regarded as co-first units.

8 REFERENCES

[1] Lian, Z.S., Yuan, X., Gao, F. (2020). Networked intelligent sensing control method for hydraulic support. *Acta Coal Sinica*, vol. 45, no. 6, p. 2078-2089, **DOI:10.13225/j.cnki.jccs.ZN20.0361**. (in Chinese)

[2] Fang, X.Q., Liang, M.F., Li, S. (2020). Key technology of multi parameter accurate perception and safety decision in intelligent working face. *Acta Coal Sinica*, vol. 45, no. 1, p. 493-508, **DOI:10.13225/j.cnki.jccs.YG19.1604**. (in Chinese)

[3] Du, Y.B. (2017). Supporting condition acquisition and fuzzy comprehensive evaluation method for hydraulic support. *Acta Coal Sinica*, vol. 42, p. 260-266, **DOI:10.13225/j.cnki.jccs.2016.1467**. (in Chinese)

[4] Bao, Y.S. (2020). Research on intelligent control key technology of fully mechanized top coal caving face in extra thick coal seam. *Coal Science and Technology*, vol. 48, no. 7, p. 55-61, **DOI:10.13199/j.cnki.cst.2020.07.004**. (in Chinese)

[5] You, X.S., Wan, H., Wei, W.Y. Research on support tracking automation based on genetic algorithm and BP neural network, from *http://kns.cnki.net/kcms/detail/11.2402.TD.20200527.1115.002.html*, accessed on 2020-06-06. (in Chinese)

[6] Wang, G.F., Hu, X.B., Liu, X.H. Yu, X., Liu, W.C., Lv, Y., Zheng, Z. (2020). Adaptability analysis of four column hydraulic support in large mining height caving mining face of kilometer deep mine. *Acta Coal Sinica*, vol. 45, no. 3, p. 865-875 **DOI:10.13225/j.cnki.jccs.SJ19.1516**. (in Chinese)

[7] Pan, Y.S., Xiao, Y.H., Li. G.Z. (2020). Research and application of roadway anti scour hydraulic support. *Acta Coal Sinica*, vol. 45, no. 1, p. 90-99, **DOI:10.13225/j.cnki.jccs.YG19.1762**. (in Chinese)

[8] Zeng, X.T., Meng, G.Y., Zheng, K. (2019). Force transmission analysis of sliding block-type hydraulic support under impact loads. *International Journal of Simulation Modelling*, vol. 18, no. 1, p. 100-111, **DOI:10.2507/IJSIMM18(1)466**.

[9] Flores, P. (2010). A parametric study on the dynamic response of planar multibody systems with multiple clearance joints. *Nonlinear Dynamics*, vol. 61, p. 633-653, **DOI:10.1007/s11071-010-9676-8**.

[10] Flores, P. Koshy, C.S., Lankarani, H.M., Ambrósio, J. (2011). Numerical and experimental investigation on multibody systems with revolute clearance joints. *Nonlinear Dynamics*, vol. 65, p. 389-398, **DOI:10.1007/s11071-010-9899-8**.

[11] Li, X.F., Wu, S.J., Li, X. (2019). Study on chaotic characteristics of spring operating mechanism considering joint clearance. *Journal of Huazhong University of science and Technology (Natural Science Edition)*, vol. 47, no. 4, p. 44-49, **DOI:10.13245/j.hust.190408**. (in Chinese)

[12] Pereira, C., Flores, P., Ramalho, A., Ambrósio, J, (2010). The influence of contact model, friction and lubrication on the dynamics of cylindrical clearance joints. *10th International Conference on Computational Structures Technology*, art. ID 218, **DOI:10.4203/ccp.93.218**.

[13] Li, S., Xu, J., Zhao, J. (2018). Research on dynamic characteristic of connecting rod with joint clearance. *6th International Conference on Mechanical Engineering, Materials Science and Civil Engineering*, **DOI:10.1088/1757-899X/542/1/012081**.

[14] Li, Y.B., Xu, T.T., Zheng, H., Wang Z.S. (2020). Dynamic characteristics of spatial parallel mechanism with spherical pair clearance. *Journal of Zhejiang University (Engineering Edition)*, vol. 54, no. 2, p. 348-356. (in Chinese)

[15] Erkaya, S. (2012). Investigation of joint clearance effects on welding robot manipulators. *Robotics and Computer-Integrated Manufacturing*, vol. 28, no. 4, p. 449-457, **DOI:10.1016/j.rcim.2012.02.001**.

[16] Erkaya, S. (2018). Effects of joint clearance on the motion accuracy of robotic manipulators. *Strojniški vestnik - Journal of Mechanical Engineering*, vol. 64, no. 2, p. 82-94, **DOI:10.5545/sv-jme.2017.4534**.

[17] Bai, Z.F., Jiang, X., Li, F., Zhao, J.J., Zhao, Y. (2018). Reducing undesirable vibrations of planar linkage mechanism with joint clearance. *Journal of Mechanical Science and Technology*, vol. 32, p. 559-565, **DOI:10.1007/s12206-018-0103-7**.

[18] Wang, X. P, Liu, G., Ma, S., Tong, R.T., Xue, Y.M. (2017). Effects of clearance joint on impact dynamic characteristics of planar mechanisms. *Journal of Vibration and Shock*, vol. 36, no. 17, p. 74-78, **DOI:10.13465/j.cnki.jvs.2017.17.012**. (in Chinese)

[19] Wang, X., Lin, W., Ji, X., Gaou, Z., Bai, X., Guo, Y. (2019). Dynamic analysis of a planar multibody system with multiple revolute clearance joints. *Proceedings of the Institution of Mechanical Engineers, Part C: Journal of Mechanical Engineering Science*, vol. 233, no. 10, p. 3429-3443, **DOI:10.1177/0954406218819022**.

[20] Matekar, S.B, Fulambarkar, A.M. (2020). Displacement analysis of slider in slider-crank mechanism with joint clearance. *Australian Journal of Mechanical Engineering*. **DOI:10.1080/14484846.2020.1763547**.

[21] Tajaril, M.J., Pedrammehr, S., Chalak Qazani, M.R., Nategh, M.J. (2017). The effects of joint clearance on the kinematic error of the hexapod tables. *5th RSI International Conference on Robotics and Mechatronics* p. 39-44, **DOI:10.1109/ICRoM.2017.8466132**.

[22] Xu, C., Dong, H., Xu, S., Wu, Y., Wang, C. (2017). Study and experiment on positioning error of SCARA robot caused by joint clearance. *10th International Conference on Intelligent Robotics and Applications*, vol. 10463, **DOI:10.1007/978-3-319-65292-4_14**.

[23] Gu, Y., Zhang, Y., Zhao, J., Yan, S.Z. (2019). Dynamic characteristics of free-floating space manipulator with joint clearance. *Journal of Mechanical Engineering*, vol. 55, no. 3, p. 99-108, **DOI:10.3901/JME.2019.03.099**.

[24] Huang, J.F., Cai, Y.L., Chen. J.Y. (2019). Kinematic accuracy analysis of 3-RRR mechanism considering clearance and member flexibility. *Machine Tool and Hydraulic*, vol. 47, no. 3, p. 3-8, **DOI:10.3969/j.issn.1001-3881.2019.03.002**. (in Chinese)

[25] Hou, Y.L., Zhao, L.J., Qi, X.F., Zeng, D.X. (2019). Dynamic simulation of a flexible parallel mechanism with clearance. *Journal of Yanshan University*, vol. 43, no. 6, p. 485-496, **DOI:10.3969/j.issn.1007-791X.2019.06.003**. (in Chinese)

[26] Zhang, X., Zhang. X. (2017). Minimizing the influence of revolute joint clearance using the planar redundantly actuated mechanism. *Robotics and Computer-Integrated Manufacturing*, vol. 46, p. 104-113, **DOI:10.1016/j.rcim.2017.01.006**.

[27] Erkaya, S. (2018). Clearance-induced vibration responses of mechanical systems: computational and experimental investigations. *Journal of the Brazilian Society of Mechanical Sciences and Engineering*, vol. 40, **DOI:10.1007/s40430-018-1015-x**.

[28] Erkaya, S. (2019). Determining power consumption using neural model in multibody systems with clearance and flexible joints. *Multibody System Dynamics*, vol. 47, p. 165-181, **DOI:10.1007/s11044-019-09682-4**.

[29] Chen, K., Zhang, G.J., Wu, R., Wang, L., Zheng, H.M., Chen, S.H. (2019). Dynamic analysis of a planar hydraulic rock-breaker mechanism with multiple clearance joints. *Shock and Vibration*, vol. 2019, art. ID 4718456, **DOI:10.1155/2019/4718456**.

[30] Tian, Q., Flores, P., Lankarani. H.M. (2018). A comprehensive survey of the analytical, numerical and experimental methodologies for dynamics of multibody mechanical systems with clearance or imperfect joints. *Mechanism and Machine Theory*, vol. 122, p. 1-57, **DOI:10.1016/j.mechmachtheory.2017.12.002**.

[31] Edler, J., Tic, V., Lovrec, D. (2019). 1-D simulation model of a progressive flow controller for hydrostatic bearings. *International Journal of Simulation Modelling*, vol. 18, no. 2, p. 267-278, **DOI:10.2507/IJSIMM18(2)472**.

[32] Erkaya, S., Uzmay, I. (2012). Effects of balancing and link flexibility on dynamics of a planar mechanism having joint clearance. *Scientia Iranica*, vol. 19, no. 3, p. 483-490, **DOI:10.1016/j.scient.2012.04.011**.

Strojniški vestnik - Journal of Mechanical Engineering 67(2021)1-2, 67-69
DOI:10.5545/sv-jme.2020.6950
Short Scientific Paper
Received for review: 2020-09-23
Received revised form: 2021-01-08
Accepted for publication: 2021-01-11

Demonstration of Interference Patterns by the Random Walk of Particles

Igor Grabec[1,*] – Nikolaj Sok[2]

[1] University of Ljubljana, Faculty of Mechanical Engeneering, Slovenia
[2] University of Ljubljana, Faculty of Computer and Information Science, Slovenia

Visualization of interference phenomena by Chladni patterns is treated. The formation of the pattern in the Young's double-slit experiment is described by a new model of driven random walk exhibited by particles bouncing on a vibrating surface. In the model the mean length of horizontal displacement is described deterministically by the wave amplitude. The presented example indicates that such formation of interference patterns can take place without any pilot-waves associated to particles. In spite od this, the pheomenon remeinds to formation of interference patterns observed at scattering of particles in quantum mechanics.

Keywords: random walk of particles, Chladni patterns, interference phenomena, Young's experiment

Highlights

- *Formation of Chladni patterns caused by interfering waves on a surface is considered. For this purpose a new model of pattern formation caused by jumping of particles on a vibrating surface is introduced.*
- *In the model the amplitude of vibrating surface is treated as a deterministic variable, while jumping of particles is described by the Gaussian random number genarator.*
- *Numerically simulated example of Chladni pattern formation in the Young's double-slit experiment shows that the distribution of particles reveales deterministic properties of interfering waves, athough the movement of individual patterns is random.*
- *This property reminds to the situation at the double slit experiment in quantum mechanics where the trajectories of individual particles indicate random character, while their distribution reveals deterministic properties of interference.*

0 INTRODUCTION

One of the great puzzles of nature is the wave-particle duality of quantum mechanics that was explained by De Broglie **[1]** and Böhm **[2]** by assigning to particles the so called pilot-waves. This duality had been considered an exclusive property of the microscopic world until the experiments with droplets bouncing on surfaces of vibrating liquids indicated that it might be characteristic of macroscopic particles too **[3]** and **[4]**. In these experiments droplets are accompanied by pilot-waves on the liquid surface where they can generate interference. In the quantum mechanical treatment the interference is governed by the Schrödinger equation **[2]**, while the interference of bouncing droplets is described by the classical wave mechanics **[3]** and **[4]**. Since the presence of pilot-waves is essential in both cases, it is rather surprising that properties of interference can be observed even when particles are not accompanied by them. This article points to the corresponding example by the numerical simulation of the Chladni pattern formation caused by interfering waves in the classical Young's double-slit experiment **[5]**.

1 MODEL AND SIMULATION

Chladni patterns are formed by the sand particles bouncing on vibrating surfaces and their application for the visualization of vibration modes has significantly contributed to the development of acoustics **[6]**. Although it is evident that during the formation of a pattern the particles move from regions of high vibration amplitude towards the calm regions at nodal lines, the analytical description of movement by bouncing remained incomplete due to its complexity **[7]** and **[8]**. To describe such movement quantitatively the trajectories of bouncing particles were statistically analyzed in recent experiments presented in the previous articles **[9]** to **[11]**. The analysis indicates that the bouncing of an individual particle corresponds to a random walk. The distribution of the horizontal displacement $\Delta\mathbf{R}(x,y)$ in this walk is Gaussian and direction independent. The standard deviation of the distribution is proportional to the amplitude of surface vibration $A(x,y)$ and characterizes the horizontal displacement length in a single bounce. This property enables a simple simulation of the pattern formation by the standard Gaussian random number generator G if the distribution of vibration amplitude $A(x,y)$ is given. Comparison of simulated and actually observed patterns reveals surprisingly good agreement of

*Corr. Author's Address: University of Ljubljana, Faculty of Mechanical Engeneering, Aškerčeva 6, 1000 Ljubljana, Slovenia, igor.grabec@fs.uni-lj.si

their properties [9] to [11]. Although the bouncing is random, the governing parameter of its distribution is determined by the vibration amplitude, and therefore, the Chladni pattern formed on a vibrating surface provides information about the characteristics of the corresponding standing wave. Since a standing wave is the result of the interference between waves moving in the opposite directions, we presume that such a pattern could be applied to characterize properties of interference also in other cases. To check this presumption we simulate a random walk of particles in the Young's experiment with interfering waves from two sources. For this purpose the model of vibration driven random walk developed in the previous article is utilized [9] to [11].

In the simulation a particular step of the random walk is generated by the modified Gaussian random number generator $(A-A_c)\times G$ with the standard deviation of the corresponding probability distribution proportional to the wave amplitude above the critical value A_c for bouncing. At the formation of Chladni patterns the critical value is usually much smaller than the wave amplitude $A_c << A$, and for the sake of simplicity, we discard it in the present modeling. The particle displacement in the x-direction during single bounce is then described by the expression: $\Delta x = A(x,y)\times G$, and similarly for the y-direction.

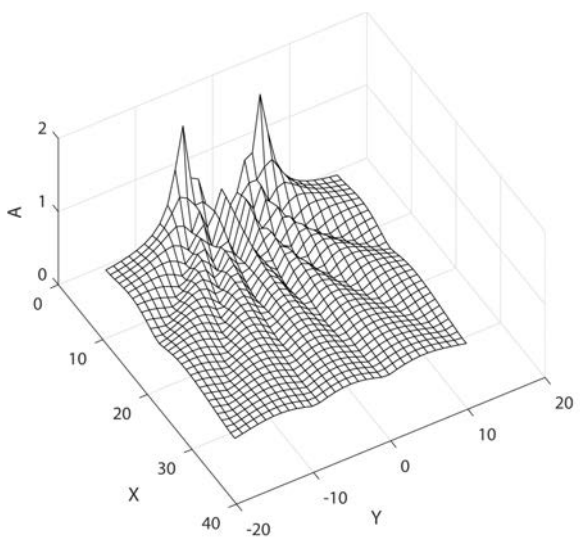

Fig. 1. *The distribution of the wave amplitude $A(x,y)$ in the simulated Young's experiment with interfering waves from two sources*

The distribution of the wave amplitude, that in our case equals the standard deviation of random number generator, is shown in Fig. 1, while the initial distribution of 5000 particles and the subsequent evolution of Chladni patterns in 100, 400, and 1600 bounces is displayed in Figs. 2 and 3. The changing of particle distribution is most expressive at the start of bouncing and declines with concentration of particles at low amplitude regions.

2 DISCUSION AND CONCLUSIONS

Figs. 2 and 3 reveal that particles move due to vibration driven random walk to the calm regions of the interference pattern. The corresponding Chladni pattern thus provides a proper basis for indicating and characterizing the interference phenomenon

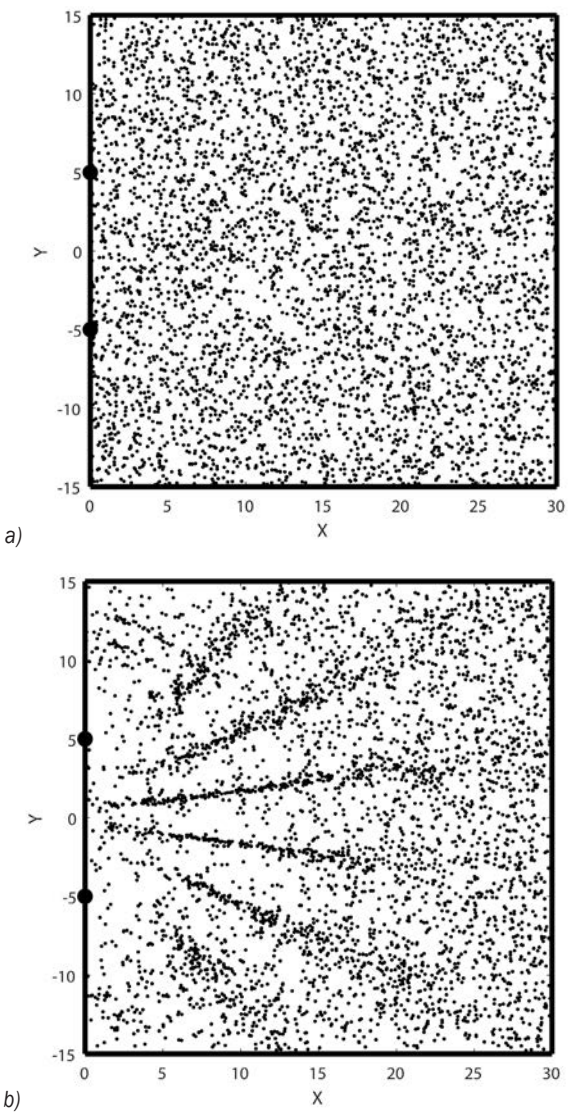

Fig. 2. *a) Initial distribution of 5000 particles, and b) Chladni pattern caused by 100 bounces*

although the particles bounce randomly during its formation. However, the interference character is in this case determined only by the properties of waves on the surface and not by any pilot-waves associated with particles. The influence of this character on a particular bounce remains unexplained, but it is simply described on average by the most simple relation between the wave amplitude and the standard deviation of the horizontal displacement.

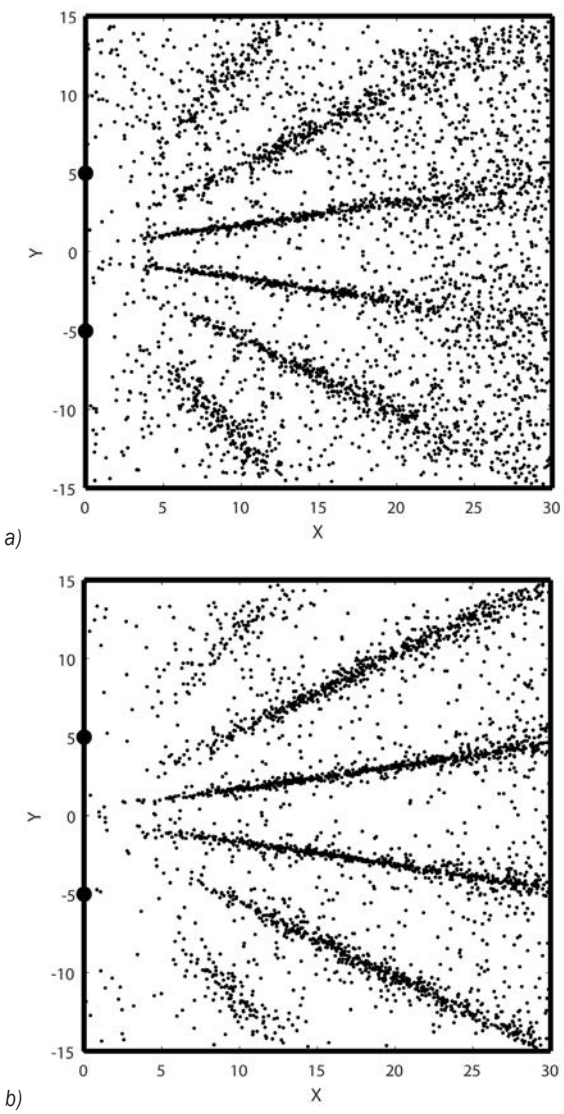

Fig. 3. *a) Chladni patterns caused by 400 bounces, and b) 1600 bounces*

In relation to the presented case the question arises whether it would be possible to find an example of interference phenomenon also in quantum mechanics that could be interpreted without wave-particle duality.

3 ACKNOWLEDGEMENTS

The authors would like to thank Prof. Tomaž Klinc for his comments and acknowledge the cooperation with the Laboratory of Synergetics at the Faculty of Mechanical Engineering, University of Ljubljana, Slovenia supported by the Slovenian Research Agency through the research core funding No. P2-0241.

4 REFERENCES

[1] de Broglie, L. (1953). The Interpretation of Wave Mechanics with the Help of Waves with Singular Regions, *from: http://arxiv.org/abs/1005.4534v1*, accessed on 2010-05-25.

[2] Böhm, D. (1952). A suggested interpretation of the quantum theory in terms of "hidden" variables. *Physical Review*, vol. 85, no. 2, p. 166-179, **DOI:10.1103/physrev.85.166**.

[3] Couder, Y., Protière, S., Fort, E., Boudaoud, A. (2005). Walking and orbiting droplets. *Nature*, vol. 437, p. 208, **DOI:10.1038/437208a**.

[4] Couder, Y., Fort, E. (2012). Probabilities and trajectories in classical wave-particle duality. *Journal of Physics: Conference Series*, vol. 361, art. ID 012001, p. 1-9, **DOI:10.1088/1742-6596/361/1/012001**.

[5] Chladni, E.F.F. (1787). Entdeckungen über die Theorie des Klanges, Leipzig, **DOI:10.14711/spcol/b495277**. (in German)

[6] Smilansky, U., Stöckmann, H.-J. (2007). Nodal patterns in physics and mathematics – From Chladni's seminal work to modern applications – A historic-scientific perspective. *EU Physical Journal - Special Topics*, vol. 145, no. 1, p. V-VI.

[7] Lichtenberg, A.J., Lieberman, M.A. (1983). *Regular and Stochastic Motion*, Springer, New York.

[8] Halev, A., Harris, D. M. (2018). Bouncing ball on a vibrating periodic surface. *Chaos*, vol. 28, no. 9, art. ID 096103, **DOI:10.1063/1.5023397**.

[9] Grabec, I. (2017). Vibration driven random walk in a Chladni experiment. *Physics Letters A*, vol 381, no. 2, p. 59-64, **DOI:10.1016/j.physleta.2016.10.059**.

[10] Grabec, I., Sok, N. (2019). Formation of Chladni Patterns by Vibration Driven Random Walk of Particles. *Nonlinear Phenomena in Complex Systems*, vol. 22, no. 1, p. 75-83.

[11] Grabec, I., Sok, N. (2018). Statistical description of particle movement in a Chladni experiment. *International Conference on "Applied Statistics", Abstracts and Program*, Statistical Society of Slovenia, Ljubljana.

List of reviewers who reviewed manuscripts in 2020

Adam Tadeusz Adamkowski, Poland
Mônica Lopes Aguiar, Span
Mohamed M.z. Ahmed, Egypt
Alma Y. Alanis, Mexico
Irina Stefanova Aleksandrova, Bulgaria
Mohammad Yeakub Ali, Brunei
Ahmed R. J. Almusawi, Iraq
Muhannad Al-Waily, Iraq
Fred Lacerda Amorim, Brasil
Dario Anastasio, Italy
Maksim Antonov, Estonia
Ivan Anžel, Slovenia
Fatahul Arifin, Indonesia
Ciril Arkar, Slovenia
Muhammad Shahid Arshad, Slovenia
Kamil Arslan, Turkey
Mohammed Asmael, Turkey
Viktor P. Astakhov, USA
Maja Atanasijević-Kunc, Slovenia
Anas Atieh, Jordan
Alexandra Aulova, Slovenia
Gokhan Aydin, Turkey

Bernd Bachert, Germany
Dražen Bajić, Croatia
Dhinesh Balasubramanian, India
Mustapha Barakat, France
Paweł Baranowski, Poland
Jani Barle, Croatia
Michael Bartoň, Spain
Michał Batsch, Poland
Branko Bauer, Croatia
Evangelos Bellos, Greece
Juraj Beniak, Slovakia
Ali Cemal Benim, Germany
Anton Bergant, Slovenia
Deepak Bharadwaj, India
Mohit Bhola, India
Ignacijo Biluš, Slovenia
Cristina Maria Biris, Romania
Miha Bobic, Slovenia
Miha Boltežar, Slovenia
Éd Claudio Bordinassi, Brasil
Tomaž Brajlih, Slovenia
Stefano Bruni, Italy
Bruno Brunone, Italy
Juana Abenójar Buendía, Spain
Vincenc Butala, Slovenia

Michele Calí, Italy
Roberto Capata, Italy
Caterina Capponi, Italy
Kadir Cavdar, Turkey
Onur Çavuşoğlu, Turkey
Xuejun Chen, China
Peng Cheng, USA
Andrea Chiocca, Germany
Veturia Chiroiu, Romani
Filippo Cianetti, Italy
Franco Concli, Italy
Romina Conte, Italy

Gregor Čepon, Slovenia
Martin Česnik, Slovenia

Mohammed Danish, Malaysia
Jos Darling, UK
J. Paulo Davim, Portugal
Luis Norberto López De Lacalle Marcaide, Spain
Mariusz Deja, Poland
Ivan Demšar, Slovenia
Hamed Aghajani Derazkola, Iran
Edvard Detiček, Slovenia
Ayyannan Devaraju, India
Janez Diaci, Slovenia
Burak Dikici, Turkey
Anselmo Eduardo Diniz, Brazil
The Vinh Do, Viet Nam
Oana Dodun, Romania
Bojan Dolšak, Slovenia
Mateja Dovjak, Slovenia
Isabel Duarte, Portugal
Jožef Duhovnik, Slovenia

Andrea Ehrmann, Germany
Ahmed Elkaseer, Germany
Manar Abd Elhakim Eltantawie, Egypt
Selcuk Erkaya, Turkey

Yusuf Fedai, Turkey
Imre Felde, Hungary
Tomasz Figlus, Poland
Luigino Filice, Italy
Robert Frazer, UK
Alessandro Freddi, Itaky
Francesco Frendo, Italy
Leonardo Frizziero, Italy

Roman Gabl, UK
Lidia Galda, Poland
Umberto Galietti, Italy
Siavash Ghanbari, USA
Mehran Ghasempour-Mouziraji, Iran
Mostafa Ghoreyshi, Iran
Gilbert-Rainer Gillich, Romania
Przemysław Golewski, Poland
Guilherme Ferreira Gomes, Brasil
María Pilar Valles González, Spain
Darko Goričanec, Slovenia
Aleš Gosar, Slovenia
Karl Gotlih, Slovenia
Edvard Govekar, Slovenia
Deepam Goyal, India
Dmitry Vladimirovich Gradov, Finland
Leo Gusel, Slovenia
Shivakanth Gutta, US

Rogelio L. Hecker, Argentina
Christian J.l. Hermes, Brasil
Marko Hočevar, Slovenia
Imre Horvath, The Netherlands
Richárd Horváth, Hungary
Mohammed Ayub Hossain, Bangladesh
Patrick C. Howlett, Australia
Ales Hribernik, Slovenia

The Editorial would like to thank all the reviewers in participating in reviewing process.
We appreciate the time and effort and greatly value the assistance as a manuscript reviewer for
Strojniški vestnik – Journal of Mechanical Engineering.

Vsebina

Strojniški vestnik - Journal of Mechanical Engineering
letnik 67, (2021), številka 1-2
Ljubljana, januar-februar 2021
ISSN 0039-2480

Izhaja mesečno

Razširjeni povzetki (extended abstracts)

Strojniški vestnik - Journal of Mechanical Engineering 67(2021)1-2, SI 3

Prejeto v recenzijo: 2020-12-22
Prejeto popravljeno: 2021-02-14
Odobreno za objavo: 2021-02-16

Analiza pretoka enokanalne mešanice kapljevitega CO_2 in MQL pri trajnostnem odrezavanju

Damir Grguraš[1] – Luka Sterle[1] – Aleš Malneršič[1] – Luka Kastelic[1] – Cedric Courbon[2] – Franci Pušavec[1,*]

[1] Univerza v Ljubljani, Fakulteta za strojništvo, Slovenija
[2] Univerza v Lyonu, École nationale d'ingénieurs de Saint-Étienne (ÉNISE), Francija

Uporaba emulzije na bazi olja, kot hladilno-mazalnega sredstva (HMS), v kombinaciji z nizko rezalno hitrostjo, privede do nizke produktivnosti konvencionalnega odrezavanja. Inovativen način za dvig produktivnosti v luči trajnostnega razvoja je odrezavanje z asistenco kapljevitega ogljikovega dioksida – LCO_2 in oljne megle – MQL. Enokanalni dovod mešanica LCO_2 + MQL predstavlja stanje tehnike pri takšnem LCO_2 podprtem odrezavanju. Za popolno razumevanje in optimizacijo hlajenja in mazanja, ki ga zagotavlja mešanica LCO_2 + MQL, je bistvena analiza pretoka medija, ki pa še ni dovolj znanstveno raziskana. To raziskovalno vrzel izpolnjuje ta znanstveni prispevek.

Analiza pretoka enokanalne mešanice LCO_2 + MQL se je izvedla s pomočjo visoko-hitrostne kamere na treh različnih pozicijah: (i) pozicija A – za analizo pretoka v dovodni šobi, kjer je bila določena povprečna hitrost toka medija; (ii) pozicija B – za analizo pretoka ob izstopu iz dovodne šobe (neposredna bližina izstopne šobe), kjer sta bili določeni povprečna hitrost pretoka in povprečni premer oljnih kapljic; (iii) pozicija C – za analizo pretoka ob izstopu iz dovodne šobe (3 mm oddaljeno od izstopne šobe), kjer sta bili določeni povprečna hitrost toka in povprečni premer oljnih kapljic. Analiza pretoka je bila izvedena s pomočjo visoko-hitrostne kamere z naslednjimi nastavitvami: (i) ločljivost zajema 512 x 384 pik in (ii) hitrost zajema 67500 sličic na sekund. Nadzorovan dovod mešanice LCO_2 + MQL je bil zagotovljen z lastniškim enokanalnim sistemom ArcLub One. Na podlagi stanja tehnike se je pri tej študiji uporabilo naslednje pretoke: masni pretok LCO_2, $\dot{m}_{LCO2}$, je znašal 100 in 200 g/min, volumski pretok olja (MQL), $\dot{V}_{olje}$, je znašal 20 in 60 ml/h. V tej študiji se je uporabilo različni MQL olji: (i) polarno olje MQL (olje 1) in (ii) nepolarno olje MQL (olje 2).

Ugotovljeno je bilo, da je hitrost toka mešanice LCO_2 + MQL odvisna od masnega pretoka LCO_2. Tako povečanje masnega pretoka LCO_2 zviša hitrost toka, npr. hitrost toka se poveča s 44 m/s na 49 m/s, ko se pretok LCO_2 poveča s 100 na 200 g/min ob nespremenjenem pretoku MQL 60 ml/h. V večji meri pa na hitrost toka mešanice LCO_2 + MQL vpliva tlačni padec in ekspanzija LCO_2 ob izstopu iz šobe. Hitrost toka se v tem primeru znatno poveča od povprečne 40 m/s v dovodni šobi na hitrost več kot 90 m/s na izstopu iz šobe. Ekspanzija LCO_2 vpliva tudi na velikost oljnih kapljic, saj se velikost le-teh ob izstopu iz šobe poveča do kritične, nestabilne velikosti. Temu sledi razpad takšnih kapljic. Velikost oljnih kapljic v mešanici LCO_2 + MQL pa je najbolj odvisna od topnosti med oljem in LCO_2. Ugotovljeno je bilo, da je topnost nepolarnega olja (olje 2), v primerjavi s polarnim oljem (olje 1), večja in tako, mešanica LCO_2 in olja 2 zagotavlja oljne kapljice premera 2 µm. Nasprotno, mešanica LCO_2 in olja 1, kjer je olje 1 delno topno v LCO_2, zagotavlja oljne kapljice s premerom več kot 5 µm. Ostanki, ki niso del mešanice LCO_2 + MQL, se pa izkažejo kot prosto leteče oljne kapljice, ki ne penetrirajo v rezalno cono, kar negativno vpliva na mazalne sposobnosti med odrezavanjem.

Prispevek te študije se kaže v izboljšanem razumevanju vedenja LCO_2 in olja, kar pomaga pri praktični uporabi LCO_2 podprtega odrezavanja. Ugotovljeno je bilo, da za najdaljšo obstojnost orodja potrebujemo nepolarno olje (olje 2) v mešanici LCO_2 + MQL. Takrat znaša obstojnost orodja L_f = 36,6 m pri frezanju titanove zlitine Ti-6Al-4V z asistenco LCO_2 + MQL. Obstojnost orodja pa je krajša (L_f = 28,0 m) ob uporabi polarnega olja (olje 1) v mešanici LCO_2 + MQL. Za nadaljnje delo se predlagajo temeljne študije vpliva mešanice LCO_2 in nepolarnega olja (olje 2) na obstojnost orodja pri odrezavanju drugih težko-obdelovalnih materialov, kot je Inconel 718, nerjavno jeklo 316L itd. Predlaga se tudi analiza obdelane površine in rezalnih sil pri obdelavi teh materialov.
Ključne besede: analiza pretoka, hitrsot pretoka, velikost kapljic, enokanalni dovod, kapljeviti ogljikov dioksid – LCO_2 (ang. *Liquid Carbon Dioxide*), oljna megla – MQL (ang. *Minimum Quantity Lubrication*), LCO_2 podprto odrezavanje

*Naslov avtorja za dopisovanje: Univerza v Ljubljani, Fakulteta za strojništvo, Aškerčeva 6, 1000 Ljubljana, Slovenija, franci.pusavec@fs.uni-lj.si

Strojniški vestnik - Journal of Mechanical Engineering 67(2021)1-2, SI 4

Prejeto v recenzijo: 2020-09-23
Prejeto popravljeno: 2020-11-20
Odobreno za objavo: 2020-12-09

Povezava med lastnostmi stika pnevmatike z voziščem in hrupom zaradi vibracij

Haichao Zhou[1,*] – Huiyun Li[1] – Chen Liang[1] – Lingxin Zhang[2] – Guolin Wang[1]

[1] Univerza Jiangsu, Šola za avtomobilsko in prometno tehniko, Kitajska
[2] AEOLUS Tyre Co. Ltd, Kitajska

Avtomobili so v neposrednem stiku z voziščem samo s pnevmatikami, ki imajo zato ključno vlogo pri stabilnosti krmiljenja, varnosti in udobju pri vožnji. Vibracije in hrup, ki nastanejo zaradi interakcij z voziščem, vplivajo na lastnosti NVH (hrup, vibracije in grobo delovanje) in s tem tudi na udobje pri vožnji in na druge lastnosti avtomobila. Novi predpisi na področju avtomobilskega hrupa, ki jih je sprejela Evropska unija (EU), vključujejo metode za preskušanje hrupa in mejne vrednosti avtomobilskega hrupa, katerega glavni vir so interakcije pnevmatik z voziščem. EU je velik uvoznik in izvoznik pnevmatik, ki morajo za prodajo na trgu EU izpolnjevati predpise glede hrupa. Izboljševanje lastnosti na področju vibracij in hrupa je zato pomemben cilj domačih in tujih raziskovalcev in proizvajalcev pnevmatik. Zgradba karkase ima velik vpliv na vibracije in hrup ter na lastnosti stika pnevmatike z voziščem. Za vibracije in hrup pnevmatik je zaslužno predvsem vzbujalno delovanje vozišča, zato obstaja potreba po preučitvi značilnih parametrov kontaktne površine med pnevmatiko in voziščem, ki vplivajo na vibracije in hrup. Te raziskave imajo tudi pomembno teoretično in aplikativno vrednost pri snovanju in optimizaciji zgradbe za zmanjšanje hrupa in vibracij.

Za preučitev odvisnosti med stikom z voziščem ter hrupom in vibracijami je bila izbrana pnevmatika za tovornjake v dimenzijah 295/80R22,5, postavljen pa je bil tudi model po metodi končnih elementov. Model je bil verificiran na podlagi rezultatov preizkusa togosti pnevmatike, modalne analize in odziva površinske hitrosti. Za določitev vpliva vibracijskih lastnosti pnevmatike na emisijo hrupa sta bili izbrani spremenljivki oblika konture in zasnova pasov. Opravljeni sta bili modalna analiza ter numerična simulacija hrupa in vibracij za različne zgradbe pnevmatik. Odtis pnevmatike na vozišču je bil razdeljen na več delov. Določeni so bili parametri stika za vsako podobmočje in preučene so bile odvisnosti med geometrijskimi in mehanskimi parametri stika pnevmatike s podlago in hrupom zaradi vibracij. Nato je bil analiziran vpliv asimetričnosti in togosti deformiranega dezena ter spektralne gostote vzbujalne sile vozišča na hrup in vibracije.

Rezultati kažejo pozitivno korelacijo med hrupom zaradi vibracij in asimetričnostjo radialne deformacije dezena. Korelacija med radialno deformacijsko togostjo in hrupom zaradi vibracij je negativna. Vršne in absolutne vrednosti spektralne gostote sile vzbujanja pnevmatike pri konstrukciji z minimalnim hrupom so znatno manjše kot pri originalni pnevmatiki. Študija bo uporabna kot teoretično vodilo pri projektiranju zgradbe tihih pnevmatik. Možnosti učinkovitega izkoriščanja odvisnosti med vibracijami in hrupom ter asimetričnostjo oz. togostjo radialne deformacije dezena pri snovanju zgradbe tihih pnevmatik bo treba še dodatno raziskati in potrditi.

V prihodnjih raziskavah bo mogoče podrobneje določiti funkcijske odvisnosti med vzbujalno silo ter hrupom in vibracijami z vidika interakcij med pnevmatikami in površino vozišča. Vrednost pričujočega članka je v določitvi in potrditvi natančnosti modela kotaljenja pnevmatike po metodi končnih elementov in v uporabi laserskega Dopplerjevega vibrometra za preskušanje odziva modela z vibracijami bočne stene. Izmerjena hitrost vibracij vseh merilnih točk na bočni steni v časovni in frekvenčni domeni potrjuje model. Preučen je tudi vpliv parametrov stika pnevmatike z voziščem na vibracije in hrup in analiziran je vpliv geometrijske porazdelitve pritiska na podlago in mehanskih parametrov na vibracije in hrup. Opredeljen je vpliv parametrov stika z voziščem na vibracije in hrup, kot so asimetričnost in togost radialne deformacije dezena ter gostota močnostnega spektra vzbujalne sile.

Ključne besede: hrup pnevmatik, parametri stika s podlago, numerična simulacija, modalna analiza, togost dezena, gostota močnostnega spektra

*Naslov avtorja za dopisovanje: Univerza Jiangsu, Šola za avtomobilsko in prometno tehniko, Zhenjiang, Kitajska, hczhou@ujs.edu.cn

Strojniški vestnik - Journal of Mechanical Engineering 67(2021)1-2, SI 5

Prejeto v recenzijo: 2020-09-25
Prejeto popravljeno: 2020-12-10
Odobreno za objavo: 2021-01-27

Ocena mehanskih, mikrostrukturnih in obrabnih lastnosti aluminijeve zlitine za avtomobilske aplikacije, ojačene s praškom iz šoljčnih lupin

Idawu Yakubu Suleiman[1,*] – Auwal Kasim[2] – Abdullahi Tanko Mohammed[3] – Munir Zubairu Sirajo[4]

[1]Univerza v Nigeriji, Oddelek za metalurgijo in materiale, Nigerija
[2]Univerza Ahmadu Bello, Oddelek za metalurgijo in materiale, Nigerija
[3]Zvezna politehnika Waziri Umaru, Oddelek za strojništvo, Nigerija
[4]Razvojni sklad za naftno tehnologijo, Abuja, Nigerija

Namen predstavljenega dela je preiskava mehanskih, mikrostrukturnih in obrabnih lastnosti zlitine Al-Mg-Si, ojačane s 3 ut. % do 15 ut. % praška iz školjčnih lupin (MSP).

V državah v razvoju se kljub njihovi navidezni razširjenosti ne proizvajajo sintetični materiali za ojačitev, kot sta silicijev karbid (SiC) in aluminijev oksid (Al_2O_3). Zaradi zanašanja na uvoz iz čezmorskih držav in neugodnih deviznih tečajev je cena sintetičnih materialov za ojačitev na lokalnih trgih razmeroma visoka. Možna alternativa dragim sintetičnim materialom so praški, izdelani iz kmetijskih odpadkov, kot je prašek iz lupin gojenih školjk. Prašek je cenovno ugoden, dostopen in prijazen do okolja.

Izdelana je bila aluminijeva zlitina, ojačena s praškom iz školjčnih lupin v različnih deležih od 3 ut. % do 15 ut. % v korakih po 3 %. Mehanske lastnosti so bile ovrednotene na standarden način (natezni, udarni in upogibni preskus, preskus trdote). Obrabne lastnosti ter mikrostruktura zlitine in kompozita so bile preiskane in primerjane z vrstičnim elektronskim mikroskopom v kombinaciji z energijsko disperzijskim rentgenskim spektrometrom (SEM/EDS).

Rezultati rentgenske fluorescenčne analize MSP z delci velikosti 100 μm je pokazala, da je v prašku največ kalcijevega oksida (95,70 % CaO). Preskusi so pokazali povišanje trdote zlitine v prisotnosti praška. Ocenjeno je bilo 45-odstotno povišanje natezne trdnosti pri povečanju deleža MSP z 0 na 3 ut. % in 2,30-odstotno povišanje pri povečanju deleža s 3 na 15 ut. % MSP. Raztezek pri pretrgu se je povišal pri povečanju deleža praška z 0 na 3 ut. % in zmanjšal pri povečanju s 3 na 15 ut. %. Preskusi so pokazali povišanje žilavosti pri povečanju deleža z 0 na 3 ut. %, znižanje pri povečanju s 6 na 9 ut. % in spet povišanje žilavosti pri 15 ut. % MSP. V upogibnih preskusih je bilo ugotovljeno povišanje trdnosti pri povečanju deleža praška z 0 na 15 ut. %. Morfologija razkriva precej enakomerno porazdelitev praška v vseh pripravljenih kompozitih.

Ugotovljene mehanske in obrabne lastnosti nakazujejo, da bi bili pripravljeni kompoziti primerni za proizvodnjo zavornih ploščic in izolatorjev v avtomobilski industriji.

Prispevek članka je v možnem znižanju stroškov in v optimizaciji lastnosti, kar sta tudi cilja tehničnega razvoja. Školjčne lupine so odpadek, ki predstavlja grožnjo za okolje. Razvoj poceni kompozitov z aluminijasto osnovo in ojačitvijo iz okolju prijaznega materiala predstavlja inovacijo na področju proizvodnje materialov. Ti kompoziti so cenejši od kompozitov s sintetičnimi ojačitvenimi materiali, kot so SiC, Al2O3, TiC itd. Rezultati bodo lahko koristili proizvajalcem zavornih čeljusti in ploščic ter avtomobilski industriji na splošno, v kateri je pomembno razmerje med trdnostjo in težo izdelkov.

Ključne besede: aluminijeva zlitina, kompoziti, prašek iz školjčnih lupin, mehanske lastnosti, mikrostruktura, obrabne lastnosti

*Naslov avtorja za dopisovanje: Univerza v Nigeriji, Oddelek za metalurgijo in materiale, Nsukka, Enugu City, Nigerija, idawu.suleiman@unn.edu.ng

Strojniški vestnik - Journal of Mechanical Engineering 67(2021)1-2, SI 6,

Prejeto v recenzijo: 2020-09-18
Prejeto popravljeno: 2020-12-08
Odobreno za objavo: 2020-12-24

Model utrjevanja materiala s kombiniranim delovanjem kolapsa kavitacijskih mehurčkov in delcev Al_2O_3 ter njegova eksperimentalna potrditev

Lei Liu* – Huafeng Guo – Ping Yu
Tehniška univerza Xuzhou, Fakulteta za strojništvo in elektrotehniko, Kitajska

Namen raziskave je razvoj nove metode utrjevanja zlitin s kombinacijo dinamike fluidov in hladnega površinskega kovanja.

Preizkušanci so bili utrjeni s kombinacijo hladnega površinskega kovanja z nanodelci Al_2O_3 in delovanja energije, ki nastane ob kolapsu kavitacijskih mehurčkov. Izbrani so bili naslednji testni parametri: moč ultrazvoka 500 W, frekvenca ultrazvoka 20 kHz, transformator za merjenje amplitude premera 15 mm na oddaljenosti 1 mm od površine vzorca in temperatura 20 °C. Z ultrazvokom so bili ustvarjeni kavitacijski mehurčki premera 2 mm do 5 mm, prožilna frekvenca pa je bila približno 60 Hz. Preizkušanci dimenzij 20 mm × 20 mm × 0,5 mm so bili izdelani iz magnezijeve zlitine AZ31. Premer delcev Al_2O_3 je bil manjši od 500 nm. Preizkušanci so bili pred preizkusi spolirani z brusnim papirjem (granulacija 8000), po preizkusu pa so bili očiščeni, posušeni s hladnim zrakom in shranjeni v zatesnjenih posodah.

Članek obravnava teorijo dinamike fluidov, dovajanje energije s kolapsom kavitacijskih mehurčkov ter izboljšanje prijemanja nanodelcev na substrat.

Po 5 minutah kombiniranega delovanja se pod vrstičnim elektronskim mikroskopom pokažejo nanodelci na površini preizkušanca. S preiskavami XRD in XPS je bilo ugotovljeno povečanje vsebnosti Al_2O_3, kar pomeni, da so delci Al_2O_3 zasidrani v površini preizkušancev. Mikrotrdota preizkušancev se je izboljšala za 36 %, vsebnost Al_2O_3 pa se je povečala za 1 %. Mehanizem utrjevanja s kombiniranim delovanjem je mogoče pojasniti s prenosom energije, ki nastane ob kolapsu kavitacijskih mehurčkov, na delce Al_2O_3, ti pa nato udarijo ob površino preizkušanca. Udarno delovanje na preizkušanec je tako bolj nežno, prehodno območje z jamicami na površini preizkušanca pa je precej bolj gladko in zvezno. Površina preizkušanca se še dodatno utrdi zaradi zasidranja nanodelcev Al_2O_3 v površino. Ti nanodelci imajo visoko trdnost in mikrotrdoto. S podaljševanjem časa utrjevanja se na površini postopoma oblikujejo nezaželene morfološke strukture. Ob podaljšanju časa kombiniranega delovanja na 10 minut so bile ugotovljene poškodbe na večjem delu površine. Rezultati preiskav XRD in XPS so pokazali, da delci Al_2O_3 vplivajo na adhezijo površinskih slojev, ki zato postopoma odpadejo od preizkušanca. Predolga obdelava zato škoduje lastnostim preizkušancev.

Podaljšanje časa utrjevanja vodi v poškodbe in zato mora biti ta čas strogo nadzorovan. Seveda je odvisen tudi od mnogih drugih lastnosti, kot je debelina preizkušanca, ki jih bo treba podrobneje preučiti.

Praktični, teoretični in znanstveni prispevki raziskave so:

- Magnezijeva zlitina je bila izpostavljena utrjevanju s kombinacijo kavitacijskih mehurčkov in nanodelcev Al_2O_3.
- Ko pride do kolapsa kavitacijskega mehurčka v bližini stene preizkušanca, delci Al_2O_3 udarijo ob površino magnezijeve zlitine in se zasidrajo v njej. Magnezijeva zlitina se tako utrjuje pod vplivom udarnih valov, ki jih oblikujejo mikrocurki.
- Zasidranje delcev Al_2O_3 v površini preizkušanca je glavni dejavnik, ki vpliva na model kombiniranega utrjevanja in prispeva k izboljšanju lastnosti preizkušancev.
- Delci Al_2O_3 se po daljši obdelavi iztrgajo iz površine preizkušanca, kar privede do degradacije mehanskih lastnosti zlitine.

Ključne besede: kolaps kavitacijskega mehurčka, nanodelci, sklopitev, model utrjevanja, mikrotrdota, morfologija, preostale napetosti

*Naslov avtorja za dopisovanje: Tehniška univerza Xuzhou, Fakulteta za strojništvo in elektrotehniko, Xuzhou, Kitajska, leiliu86@sina.cn

Strojniški vestnik - Journal of Mechanical Engineering 67(2021)1-2, SI 7,

Received for review: 2020-08-27
Received revised form: 2020-12-16
Accepted for publication: 2021-01-14

Preiskava vpliva parametrov laserskega varjenja na trdnost jekel TRIP

Khot Rahul S[1] – T. Venkateshwara Rao[2] – H. N. Girish[3] – Tadashi Ishigaki[4] – Puttaswamy Madhusudan[5,6,*]

[1]Univerza K L, Oddelek za strojništvo, Indija
[2]Inštitut za tehnologijo DBS, Oddelek za strojništvo, Kavali, Indija
[3]Univerza Mysore, Oddelek za geologijo, Indija
[4]Univerza Tottori, Fakulteta za strojništvo, Japonska
[5]Ton Duc Thang University, Raziskovalna skupina za okoljski inženiring in management, Vietnam
[6]Univerza Ton Duc Thang, Fakulteta za okoljske študije in varstvo pri delu, Vietnam

Pričujoči članek raziskuje uporabo laserja Nd:YAG za utrjevanje jekla s plastičnostjo, inducirano z deformacijo (TRIP), med procesom varjenja za aplikacije v avtomobilski industriji. Po karakterizaciji materiala je bil preučen vpliv različnih pogojev pri varjenju na trdnost spoja, vključno z vpadnim kotom laserskega žarka, hitrostjo varjenja in močjo laserja. Preučene so bile tudi mikrostruktura, natezna trdnost in mikrotrdota lasersko varjene pločevine TRIP ter njihov vpliv na toplotno vplivani pas (HAZ) in na talilno cono (FZ).

Jekla TRIP v obliki hladno vlečene pločevine z debelino 2 mm je dobavilo podjetje Nextgen Steels and Alloys. Zvar je bil narejen v prečni smeri po dolžini preizkušancev, pripravljenih po standardu ASTM E8/E8M. Preiskana je bila mikrostruktura po prečnem prerezu v talilni coni, toplotno vplivani coni in osnovni kovini. Preizkušanci so bili spolirani na stroju za lepanje s praškom iz aluminijevega oksida in vodo. Po poliranju so bili potopljeni v 5 % raztopino nitala in 95 % raztopino metanola za nadaljnjo karakterizacijo. Deformacija in porušitvena natezna trdnost sta bili izmerjeni na univerzalnem preskuševalnem stroju SAR Testing Systems STS 248 z natančnostjo ±1 % pri delovni hitrosti 5 mm/min. Termografski posnetki so bili izdelani s termovizijsko kamero Testo 875i.

Eksperimentalno določena porušitvena trdnost 487,65 MPa se dobro ujema s porušitveno trdnostjo 485,18 MPa, določeno s programsko opremo za simulacije. Rezultati eksperimentov so pokazali, da ima vpadni kot laserskega žarka pomembno vlogo pri izboljšanju trdnosti jekla. Največja porušitvena trdnost v višini 549 MPa je bila ugotovljena pri vpadnem kotu 80°, hitrosti 30 mm/s in moči 2200 W. S povečanjem moči in hitrosti sta se povečali tudi deformacija in trdnost jekla. Preiskava mikrostrukture je pokazala, da se je mikrotrdota v talilni coni s povečanjem moči in ohranitvijo nizkih vrednosti ostalih parametrov povečala na 185 HV1.0/10. S spreminjanjem vpadnega kota laserskega žarka je bilo doseženo 9,62-odstotno izboljšanje natezne trdnosti in 67-odstotno izboljšanje deformacije.

To delo je omejeno le na izbrane parametre, v prihodnje raziskave pa bo mogoče vključiti tudi ostale parametre, kot so smer potovanja, goriščna dolžina, goriščna razdalja, vrsta laserja, premer laserja, vrste materialov itd. Možno bo tudi kombiniranje laserskega varjenja z obločnim ali ultrazvočnim varjenjem.

Ključne besede: jeklo TRIP, lasersko varjenje, laser Nd:YAG, mehanska trdnost, mikrotrdota, termovizijska kamera

*Naslov avtorja za dopisovanje: Univerza Ton Duc Thang, Fakulteta za okoljske študije in varstvo pri delu, Ho Chi Minh, Vietnam, puttaswamy.madhusudan@tdtu.edu.vn

Strojniški vestnik - Journal of Mechanical Engineering 67(2021)1-2, SI 8,

Received for review: 2020-10-19
Received revised form: 2020-12-18
Accepted for publication: 2021-01-13

Dinamična analiza hidravličnega podporja z enkratno zračnostjo

Qingliang Zeng [1,2] – Yangyang Li, – Yang Yang[1,*]

[1] Znanstveno-tehniška univerza v Shandongu, Kolidž za strojništvo in elektroniko, Kitajska
[2] Univerza v Shandongu, Kitajska

Hidravlična podporja imajo pomembno vlogo v premogovništvu. Za njihovo delovanje brez prisotnosti ljudi bo treba izboljšati natančnost premikov in optimizirati napetostna stanja v podporju. Zračnost je pomembna lastnost mehanizmov, ki ima velik vpliv na gibanja hidravličnega podporja in na sile v njem.

Hidravlično podporje je kompleksen paralelni mehanizem s sferično, translatorno in rotacijsko kinematično vezjo. Vpliv posamezne zračnosti bi bilo težko natančno opisati, če bi želeli zajeti vse zračnosti hkrati. Za pričujočo študijo je bila zato izbrana zračnost med zadnjo ročico in osnovo, s čimer je bil odpravljen vpliv zračnosti v ostalih kinematičnih parih. Ta zračnost je pomembna za delovanje hidravličnega podporja, izbrana kinematična vez pa je najprimernejša za preučevanje vpliva enkratnih zračnosti na dinamiko podporja. Za določitev vpliva zračnosti na gibanja podporja in na napetosti v njem je bila opravljena dinamična analiza podporja z zračnostjo med zadnjo ročico in osnovo ter podporja brez take zračnosti. Narejena je bila primerjava gibanj zadnje ročice in kontaktnih sil v kinematični vezi z zračnostjo. Velikosti zračnosti v različnih kinematičnih vezeh se razlikujejo, prav tako pa se razlikuje njihov vpliv na gibanje mehanizmov in na napetosti v njih. Za preučitev vpliva velikosti zračnosti na dinamične lastnosti hidravličnega podporja je bila opravljena dinamična analiza podporja z različnimi vrednostmi zračnosti. S primerjavo gibanj in napetosti v podporju pri različnih zračnostih je bil določen vpliv velikosti zračnosti na podporje. Zadnja ročica kot del štirizgibnega mehanizma pomembno vpliva na držo podporja. Za preučitev vpliva zračnosti na držo podporja sta bila določena gibanje vrha zgornjega nosilca ter sprememba kota sprednjih in zadnjih stojk med procesom dviganja podporja pri različnih vrednostih zračnosti. Na zračnost med drugim najbolj vplivajo sunki. Različni načini dovoda olja pri iztegovanju stojk podporja imajo različen vpliv na podporje, prisotnost zračnosti pa ta vpliv le poveča. Za določitev vpliva zračnosti na podporje pri različnih načinih dovoda olja sta bila analizirana dva načina iztegovanja sprednjih in zadnjih stojk: z nezveznim in zveznim dovodom olja. Analizirana so bila gibanja in sile v podporju.

Za simulacijo napetosti v hidravličnem podporju z enkratno zračnostjo je bila uporabljena os ustrezno drugačnih dimenzij na zadnji ročici in na osnovi, dodan pa je bil tudi model kontaktne sile med zadnjo ročico, osnovo in osjo. Pri simulaciji zračnosti med zadnjo ročico in osnovo sta bila uporabljena model kontaktne sile L-N in izboljšani model Coulombovega trenja za popis normalne in tangencialne sile na kontaktu z zračnostjo. Proces dviganja podporja je bil simuliran s koračno funkcijo.

Prisotnost zračnosti v primerjavi s podporjem brez zračnosti povzroči variiranje gibanj in napetosti v podporju, s tem pa se zmanjša stabilnost njegovega delovanja. Velikost zračnosti vpliva na variiranje gibanj in sil v podporju. Pri različnih načinih iztegovanja so bili ugotovljeni različni odgovori podporja z zračnostjo. Način dovoda olja z zveznim prehodom lahko zmanjša variacije zaradi zračnosti, ki sicer vplivajo na stabilnost delovanja podporja.

V pričujoči študiji je bila upoštevana samo zračnost med zadnjo ročico in osnovo hidravličnega podporja. Raziskave vplivov zračnosti v hidravličnem podporju bo zato treba postopoma razširiti tako, da bodo zajele več zračnosti.

S preučevanjem zračnosti je mogoče podrobneje analizirati gibanja hidravličnega podporja za realizacijo natančnega upravljanja, s končnim ciljem izkopa premoga brez prisotnosti ljudi.

Ključne besede: pametno rudarjenje, dinamična analiza, zračnost kinematičnega para, velikost zračnosti, drža hidravličnega podporja, način dovoda olja pri iztegovanju

*Naslov avtorja za dopisovanje: Znanstveno-tehniška univerza v Shandongu, Kolidž za strojništvo in elektroniko, Kitajska, yang.yang@sdust.edu.cn

Strojniški vestnik - Journal of Mechanical Engineering 67(2021)1-2, SI 9

Prejeto v recenzijo: 2020-09-23
Prejeto popravljeno: 2021-01-08
Odobreno za objavo: 2021-01-11

Prikaz interferenčnih vzorcev z naključnim gibanjem delcev

Igor Grabec[1,*] – Nikolaj Sok[2]

[1] Univerza v Ljubljani, Fakulteta za strojništvo, Slovenija
[2] Univerza v Ljubljani, Fakulteta za računalništvo in informatiko, Slovenija

Valovni značaj delcev v kvantni mehaniki predstavlja presenetljivo lastnost, ki sta jo De Broglie in Böhm poskusila razložiti tako, da sta delcem pripisala pilotni val. Ta dvoličnost je bila obravnavana kakor lastnost mikro-sveta do nedavnega, ko so poskusi s kapljicami na površini vibrirajoče kapljevine pokazali, da je lahko značilna tudi za makroskopske delce. V teh poskusih spremljajo kapljice pilotni valovi na kapljevini, kar lahko vodi do interferenčnih pojavov, podobno kakor pri delcih v mikro-svetu. Glavni namen članka je pokazati, da lahko opazimo interferenčne pojave pri gibanju delcev na vibrijočih površinah celo tedaj, ko ni prisoten pilotni val. V ta namen je numerično prikazano nastajanje Chladnijevega vzorca, ki ga povzroči interferenca valov v Youngovem poskusu.

Chladnijev vzorec oblikujejo trdni delci, ki poskakujejo na vibrirajoči površini. Uporaba teh vzorcev za analizo nihanja teles je precej pripomogla pri razvoju akustike. Čeprav je očitno, da se pri oblikovanju takšnega vzorca gibljejo delci iz področja z visoko amplitudo vibriranja v področje z nizko amplitudo, pa analitičen opis tega gibanja dolgo ni bil izpeljan zaradi kompleksnosti celotnega pojava. V ta namen so bile šele nedavno analizirane trajektorije poskakujočih delcev na vibrirajočih površinah. Analiza je pokazala, da je poskakovanje posameznega delca naključno. Porazdelitev horizontalnega premika $\Delta\mathbf{R}(x,y)$ je Gaussova in neodvisna od smeri. Standardna deviacija porazdelitve je sorazmerna amplitudi vibracije $A(x,y)$ in karakterizira dolžino premika v enem skoku. Ta lastnost omogoča preprosto simulacijo oblikovanja Chladnijevega vzorca z generatorjem naključnih števil G na osnovi podane porazdelitve amplitude vibracij $A(x,y)$. Primerjava simuliranih in opaženih vzorcev pokaže presenetljivo dobro ujemanje njihovih lastnosti. Čeprav je poskakovanje delcev naključno, je osnovni parameter porazdelitve določen z amplitudo vibracije, in zato Chladnijev vzorec, ki nastane na vibrirajoči površini, nudi informacijo o karakteristikah ustreznega stojnega vala na površini. Ker je stojni val posledica interference valov gibajočih se v nasprotnih smereh, lahko predpostavimo, da je Chladnijev vzorec uporaben za karakteriziranje lastnosti interference tudi v drugih primerih. Za potrditev te predpostavke simuliramo gibanje delcev v Youngovem poskusu, ki vključuje interferenco valov iz dveh izvorov. V ta namen uporabimo model vsiljenega naključnega premikanja iz predhodnega članka.

V simulaciji je posamezni premik opredeljen z Gaussovim generatorjem naključnih števil: $(A(x,y)-A_c)\times G$, ki ima standardno deviacijo porazdelitve verjetnosti sorazmerno amplitudi vibracije nad kritično vrednostjo A_c za poskakovanje. Premik delca v x-smeri pri skoku je opisan z enačbo: $\Delta x=(A(x,y)-A_c)\times G$, in podobno v y-smeri. Porazdelitev amplitude vala je prikazana na Sliki 1, medtem ko je porazdelitev 5000 delcev v Chladnijevem vzorcu na začetku, in po 100, 400, ter 1600 skokih, prikazana na Slikah 2 in 3. Spreminjanje porazdelitve delcev je najbolj izrazito na začetku poskakovanja in pojenjuje s premikanjem delcev v področja z majhno amplitudo.

Sliki 2 in 3 kažeta, da se delci gibljejo zaradi poskakovanja v mirna področja. Nastali Chladnijev vzorec zato nudi osnovo za prikazovanje in karakteriziranje interferenčnega pojava, četudi pri njegovem nastajanju poskakujejo delci naključno. Seveda so lastnosti interferenčnega pojava v tem primeru opredeljene samo z lastnostmi valov na površini in ne s pilotnimi valovi delcev. V zvezi s prikazanim primerom se pojavi vprašanje, ali bi bilo mogoče tudi v kvantni mehaniki najti primer intereferenčnega pojava, ki bi ga lahko interpretirali brez valovne dvoličnosti delcev iz mikro-sveta.

Ključne besede: naključno gibanje delcev, Chladnijevi vzorci, interferenčni pojav, Youngov poskus

*Naslov avtorja za dopisovanje: Univerza v Ljubljani, Fakulteta za strojništvo, Aškerčeva 6, 1000 Ljubljana, Slovenija, igor.grabec@fs.uni-lj.si

Guide for Authors

All manuscripts must be in English. Pages should be numbered sequentially. The manuscript should be composed in accordance with the Article Template given above. The maximum length of contributions is 12 pages (approx. 5000 words). Longer contributions will only be accepted if authors provide justification in a cover letter. For full instructions see the Information for Authors section on the journal's website: http://en.sv-jme.eu .

SUBMISSION:

Submission to SV-JME is made with the implicit understanding that neither the manuscript nor the essence of its content has been published previously either in whole or in part and that it is not being considered for publication elsewhere. All the listed authors should have agreed on the content and the corresponding (submitting) author is responsible for having ensured that this agreement has been reached. The acceptance of an article is based entirely on its scientific merit, as judged by peer review. Scientific articles comprising simulations only will not be accepted for publication; simulations must be accompanied by experimental results carried out to confirm or deny the accuracy of the simulation. Every manuscript submitted to the SV-JME undergoes a peer-review process.

The authors are kindly invited to submit the paper through our web site: http://ojs.sv-jme.eu. The Author is able to track the submission through the editorial process - as well as participate in the copyediting and proofreading of submissions accepted for publication - by logging in, and using the username and password provided.

SUBMISSION CONTENT:

The typical submission material consists of:

- A **manuscript** (A PDF file, with title, all authors with affiliations, abstract, keywords, highlights, inserted figures and tables and references),
- Supplementary files:
  - a **manuscript** in a WORD file format
  - a **cover letter** (please see instructions for composing the cover letter)
  - a ZIP file containing **figures** in high resolution in one of the graphical formats (please see instructions for preparing the figure files)
  - possible **appendicies** (optional), cover materials, video materials, etc.

Incomplete or improperly prepared submissions will be rejected with explanatory comments provided. In this case we will kindly ask the authors to carefully read the Information for Authors and to resubmit their manuscripts taking into consideration our comments.

COVER LETTER INSTRUCTIONS:

Please add a **cover letter** stating the following information about the submitted paper:

1. Paper **title**, list of **authors** and their **affiliations**. **One** corresponding author should be provided.
2. **Type of paper**: original scientific paper (1.01), review scientific paper (1.02) or short scientific paper (1.03).
3. A **declaration** that neither the manuscript nor the essence of its content has been published in whole or in part previously and that it is not being considered for publication elsewhere.
4. State the **value of the paper** or its practical, theoretical and scientific implications. What is new in the paper with respect to the state-of-the-art in the published papers? Do not repeat the content of your abstract for this purpose.
5. We kindly ask you to suggest at least two **reviewers** for your paper and give us their names, their full affiliation and contact information, and their scientific research interest. The suggested reviewers should have at least two relevant references (with an impact factor) to the scientific field concerned; they should not be from the same country as the authors and should have no close connection with the authors.

FORMAT OF THE MANUSCRIPT:

The manuscript should be composed in accordance with the Article Template. The manuscript should be written in the following format:

- A **Title** that adequately describes the content of the manuscript.
- A list of **Authors** and their **affiliations**.
- An **Abstract** that should not exceed 250 words. The Abstract should state the principal objectives and the scope of the investigation, as well as the methodology employed. It should summarize the results and state the principal conclusions.
- 4 to 6 significant **key words** should follow the abstract to aid indexing.
- 4 to 6 **highlights;** a short collection of bullet points that convey the core findings and provide readers with a quick textual overview of the article. These four to six bullet points should describe the essence of the research (e.g. results or conclusions) and highlight what is distinctive about it.
- An **Introduction** that should provide a review of recent literature and sufficient background information to allow the results of the article to be understood and evaluated.
- A **Methods** section detailing the theoretical or experimental methods used.
- An **Experimental section** that should provide details of the experimental set-up and the methods used to obtain the results.
- A **Results** section that should clearly and concisely present the data, using figures and tables where appropriate.
- A **Discussion** section that should describe the relationships and generalizations shown by the results and discuss the significance of the results, making comparisons with previously published work. (It may be appropriate to combine the Results and Discussion sections into a single section to improve clarity.)
- A **Conclusions** section that should present one or more conclusions drawn from the results and subsequent discussion and should not duplicate the Abstract.
- **Acknowledgement** (optional) of collaboration or preparation assistance may be included. Please note the source of funding for the research.
- **Nomenclature** (optional). Papers with many symbols should have a nomenclature that defines all symbols with units, inserted above the references. If one is used, it must contain all the symbols used in the manuscript and the definitions should not be repeated in the text. In all cases, identify the symbols used if they are not widely recognized in the profession. Define acronyms in the text, not in the nomenclature.
- **References** must be cited consecutively in the text using square brackets [1] and collected together in a reference list at the end of the manuscript.
- **Appendix(-icies)** if any.

SPECIAL NOTES

Units: The SI system of units for nomenclature, symbols and abbreviations should be followed closely. Symbols for physical quantities in the text should be written in italics (e.g. *v*, *T*, *n*, etc.). Symbols for units that consist of letters should be in plain text (e.g. ms^{-1}, K, min, mm, etc.). Please also see: http://physics.nist.gov/cuu/pdf/sp811.pdf .

Abbreviations should be spelt out in full on first appearance followed by the abbreviation in parentheses, e.g. variable time geometry (VTG). The meaning of symbols and units belonging to symbols should be explained in each case or cited in a **nomenclature** section at the end of the manuscript before the References.

Figures (figures, graphs, illustrations digital images, photographs) must be cited in consecutive numerical order in the text and referred to in both the text and the captions as Fig. 1, Fig. 2, etc. Figures should be prepared without borders and on white grounding and should be sent separately in their original formats. If a figure is composed of several parts, please mark each part with a), b), c), etc. and provide an explanation for each part in Figure caption. The caption should be self-explanatory. Letters and numbers should be readable (Arial or Times New Roman, min 6 pt with equal sizes and fonts in all figures). Graphics (submitted as supplementary files) may be exported in resolution good enough for printing (min. 300 dpi) in any common format, e.g. TIFF, BMP or JPG, PDF and should be named Fig1.jpg, Fig2.tif, etc. However, graphs and line drawings should be prepared as vector images, e.g. CDR, AI. Multi-curve graphs should have individual curves marked with a symbol or otherwise provide distinguishing differences using, for example, different thicknesses or dashing.

Tables should carry separate titles and must be numbered in consecutive numerical order in the text and referred to in both the text and the captions as Table 1, Table 2, etc. In addition to the physical quantities, such as *t* (in italics), the units [s] (normal text) should be added in square brackets. Tables should not duplicate data found elsewhere in the manuscript. Tables should be prepared using a table editor and not inserted as a graphic.

REFERENCES:

A reference list must be included using the following information as a guide. Only cited text references are to be included. Each reference is to be referred to in the text by a number enclosed in a square bracket (i.e. [3] or [2] to [4] for more references; do not combine more than 3 references, explain each). No reference to the author is necessary.

References must be numbered and ordered according to where they are first mentioned in the paper, not alphabetically. All references must be complete and accurate. Please add DOI code when available. Examples follow.

Journal Papers:

Surname 1, Initials, Surname 2, Initials (year). Title. Journal, volume, number, pages, DOI code.

[1] Hackenschmidt, R., Alber-Laukant, B., Rieg, F. (2010). Simulating nonlinear materials under centrifugal forces by using intelligent cross-linked simulations. *Strojniški vestnik - Journal of Mechanical Engineering,* vol. 57, no. 7-8, p. 531-538, DOI:10.5545/sv-jme.2011.013.

Journal titles should not be abbreviated. Note that journal title is set in italics.

Books:

Surname 1, Initials, Surname 2, Initials (year). Title. Publisher, place of publication.

[2] Groover, M.P. (2007). *Fundamentals of Modern Manufacturing*. John Wiley & Sons, Hoboken.

Note that the title of the book is italicized.

Chapters in Books:

Surname 1, Initials, Surname 2, Initials (year). Chapter title. Editor(s) of book, book title. Publisher, place of publication, pages.

[3] Carbone, G., Ceccarelli, M. (2005). Legged robotic systems. Kordić, V., Lazinica, A., Merdan, M. (Eds.), Cutting Edge Robotics. Pro literatur Verlag, Mammendorf, p. 553-576.

Proceedings Papers:

Surname 1, Initials, Surname 2, Initials (year). Paper title. Proceedings title, pages.

[4] Štefanić, N., Martinčević-Mikić, S., Tošanović, N. (2009). Applied lean system in process industry. *MOTSP Conference Proceedings*, p. 422-427.

Standards:

Standard-Code (year). Title. Organisation. Place.

[5] ISO/DIS 16000-6.2:2002. *Indoor Air – Part 6: Determination of Volatile Organic Compounds in Indoor and Chamber Air by Active Sampling on TENAX TA Sorbent, Thermal Desorption and Gas Chromatography using MSD/FID.* International Organization for Standardization. Geneva.

WWW pages:

Surname, Initials or Company name. Title, from http://address, date of access.

[6] Rockwell Automation. Arena, from *http://www.arenasimulation.com,* accessed on 2009-09-07.

EXTENDED ABSTRACT:

When the paper is accepted for publishing, the authors will be requested to send an **extended abstract** (approx. one A4 page or 3500 to 4000 characters or approx. 600 words). The instruction for composing the extended abstract are published on-line: http://www.sv-jme.eu/information-for-authors/ .

COPYRIGHT:

Authors submitting a manuscript do so on the understanding that the work has not been published before, is not being considered for publication elsewhere and has been read and approved by all authors. The submission of the manuscript by the authors means that the authors automatically agree to transfer copyright to SV-JME when the manuscript is accepted for publication. All accepted manuscripts must be accompanied by a Copyright Transfer Agreement, which should be sent to the editor. The work should be original work by the authors and not be published elsewhere in any language without the written consent of the publisher. The proof will be sent to the author showing the final layout of the article. Proof correction must be minimal and executed quickly. Thus it is essential that manuscripts are accurate when submitted. Authors can track the status of their accepted articles on http://en.sv-jme.eu/.

PUBLICATION FEE:

Authors will be asked to pay a publication fee for each article prior to the article appearing in the journal. However, this fee only needs to be paid after the article has been accepted for publishing. The fee is 380 EUR (for articles with maximum of 6 pages), 470 EUR (for articles with maximum of 10 pages), plus 50 EUR for each additional page. The additional cost for a color page is 90.00 EUR (only for a journal hard copy; optional upon author's request). These fees do not include tax.

Strojniški vestnik -Journal of Mechanical Engineering
Aškerčeva 6, 1000 Ljubljana, Slovenia, e-mail: info@sv-jme.eu

9 770039 248001
ISSN 0039-2480

http://www.sv-jme.eu

Contents

Papers